The application of broadband ultrafast spectroscopy to reveal structural, magnetic and electronic dynamics in quantum materials

by

David Moreno Mencía

Thesis supervisor:
Prof. Dr. Simon Wall

A thesis submitted in fulfilment of the requirements
for the degree of Doctor of Philosophy
in

Ultrafast Dynamics of Quantum Solids

ICFO – Institut de Ciències Fotòniques
UPC – Universitat Politècnica de Catalunya

Barcelona, October 2021

Thesis committee:

Prof. Dr. Michael Gensch (Technische Universität Berlin, Germany)
Prof. Dr. Paul van Loosdrecht (Universität zu Köln, Germany)
Prof. Dr. Dmitri K. Efetov (ICFO - Institut de Ciències Fotòniques, Spain)

Abstract

In the last decades, quantum materials have received much attention in the field of condensed matter physics due, in part, to their exotic properties. These are difficult to understand as they result from multiple physical interactions with similar strength, such as charge, spin, orbitals and phonon degrees of freedom.

To study and control these interactions, the use of light has emerged as a powerful tool. For example, thanks to recent advantages on X-ray sources it has been possible to improve our understanding of how the atomic structure of quantum materials changes upon photo-excitation. However, these experiments are difficult and there are only a few facilities in the world to perform them. In contrast to X-ray sources, table-top ultrafast laser systems allow us to measure in a systematic manner by performing optical pump-probe spectroscopy. The versatility of this approach enables the simultaneous monitoring of the different degrees of freedom that dictate the properties of quantum materials. In this thesis, we use pump-probe broadband spectroscopy in the visible region to study the structural, electronic and magnetic dynamics with unprecedented detail in two key quantum materials such as $Sr_3Ir_2O_7$ and V_2O_3.

In $Sr_3Ir_2O_7$, a compound that undergoes a magnetic phase transition, firstly we study how photo-excitation affects to the reflectivity at a wide range of energies. This provides us information about the electronic and structural properties of this compound. Secondly, we show how to control magnetic order by photo-excitation and demonstrate that light can non-thermally suppress the magnetic long-range order in this material.

In V_2O_3 we characterize its insulator to metal and structural phase transitions. In the metallic state, we show that a key phonon mode is very sensitive to sample inhomogeneity. When taking this into account, we find no evidence for non-thermal lattice dynamics in contrast to existing literature. Furthermore, we show that the light induced transition from the insulator to metallic phase proceeds along a highly damped and incoherent pathway, where vibrational coherence is not observed.

Resumen

En las últimas décadas, los materiales cuánticos han generado un gran interés en el campo de la materia condensada debido, en parte, a sus exóticas propiedades. Éstas son difíciles de comprender ya que surgen de una compleja interacción física entre los distintos grados de libertad como la carga, el espín, el momento orbital y fonones.

El uso de la luz surge como una herramienta poderosa para estudiar y controlar estas interacciones. Por ejemplo, gracias a los avances en los sistemas de rayos X se ha mejorado nuestra comprensión de cómo la estructura atómica de los materiales cuánticos cambia bajo la fotoexcitación. Sin embargo, estos experimentos son difíciles y, además, hay escasas instalaciones alrededor del mundo para poder realizarlos. A diferencia de los sistemas de rayos X, los sistemas láseres ultrarrápidos nos permiten medir de una manera sistemática mediante la espectroscopía de bomba-sonda. La versatilidad de esta técnica permite monitorizar de manera simultánea los diferentes grados de libertad que determinan las propiedades de los materiales cuánticos. En esta tesis, utilizamos espectroscopía de bomba-sonda de banda ancha en la región visible para estudiar las dinámicas estructurales, electrónicas y magnéticas con detalles sin precedentes en dos materiales cuánticos clave como $Sr_3Ir_2O_7$ y V_2O_3.

En $Sr_3Ir_2O_7$, compuesto que experimenta una transición de fase magnética, estudiamos en primer lugar cómo la fotoexcitación afecta a la reflectividad en un amplio rango de energías. Esto nos proporciona información sobre las propiedades estructurales y electrónicas de dicho compuesto. En segundo lugar, mostramos cómo se puede controlar el orden magnético mediante la fotoexcitación, demostrando que la luz puede suprimir el orden magnético de largo alcance de manera no térmica en este material.

En V_2O_3 caracterizamos las transiciones metal-aislante y estructurales del material. En el estado metálico mostramos que un modo de los fonones clave es muy sensible a la falta de homogeneidad de la muestra. Al tener esto en cuenta, no encontramos pruebas de cambios estructurales no-termodinámicos, en contraste con la literatura existente. Además, mostramos que la transición

de fase metal-aislante inducida por la luz se realiza de una manera altamente amortiguada e incoherente, donde no se observa la frecuencia vibratoria.

Contents

List of Tables

List of Figures

Chapter 1

Introduction

1.1 Electronic band structure of solids

Condensed matter physics explains the properties of materials in which the hierarchy of the basic physical interactions is consolidated, such as free-electron metals, ionic insulators or covalent semiconductors. Usually, the properties of materials can be successfully predicted by band structure theory. Bands, formed from a linear combination of the atomic orbitals, within the symmetry of the lattice, are constructed by assuming that the effects of the interactions between electrons can be ignored, allowing each electron to be treated independently. Each band can support a finite number of electrons and the bands are separated by an energy gap. The probability that an electron can occupy a state with E energy is given by the Fermi-Dirac distribution

$$\mathrm{f(E)} = \frac{1}{\mathrm{e}^{(\mathrm{E}-\mathrm{E_F})/\mathrm{k_B T}} + 1} \tag{1.1}$$

where $\mathrm{k_B}$ is the Boltzmann's constant, T is the absolute temperature and $\mathrm{E_F}$ is the Fermi level, which is a hypothetical energy level of an electron, such that at thermodynamic equilibrium this energy level would have a 50% probability of being occupied at any given time. The location of $\mathrm{E_F}$ in a material's band structure determines the electrical behaviour of the material:

- A material is an insulator if $\mathrm{E_F}$ is located within a large band gap. Then, the material cannot respond to direct current and low frequency electric fields because the band is full and a finite amount of energy is required to excite the charge.

- A material is a semiconductor if $\mathrm{E_F}$ is surrounded by a bandgap but the electrons can easily move into some unoccupied band states, allowing the material to respond to direct current and low frequency electric fields.

- A material is a metal or semimetal if the $\mathrm{E_F}$ is inside of one or more allowed bands. In a semimetal, the conduction and valance band are overlapped.

A diagram of the band structure is shown in Figure 1.1. If we analyse, for example, the case of Gold (Au), with atomic number Z=79, and an electron configuration of [Xe]$4\mathrm{f}^{14}5\mathrm{d}^{10}6\mathrm{s}^{1}$, it can be defined as a metal because the 6s band is half filled and electrons can move freely through it. On the other hand, in the case of Silicon (Si), with Z=14 and an electron configuration of [Ne]$3s^2 3p^2$, one would expect a metallic character since there are only two electrons in the p orbital, however the *s* and *p* atomic orbitals combine to form sp^3 molecular orbital, i.e. the energy level splits into 4 bonding sp^3 orbitals, which are fully occupied and 4 antibonding orbitals which are unoccupied, thus Si is defined as a semiconductor. A similar case to Si is found in Magnesium (Mg) with electron configuration [Ne]$3s^2$ that would make it an insulator, but as the *s* and *p* orbitals overlap, the system is a semi-metal.

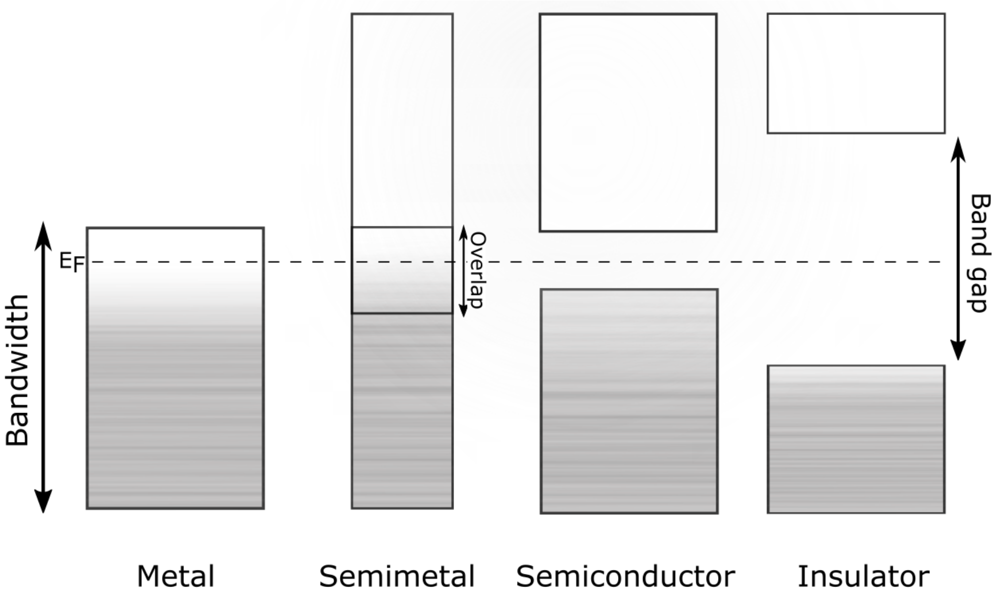

Figure 1.1: **Band structure diagrams for metals, semimetals, semiconductors, and insulators.** The dashed line indicates the Fermi level (E_F).

Therefore, to determine if an element is an insulator or metal with band theory, it is important to know how the energy levels are hybridized in a solid. This requires understanding how the energy levels of the free ions. This is often successful achieved with density functional theory (DFT), which is able to accurate predict the properties of many materials. However, there are many materials in which the application of DFT spectacularly fails to reproduce the real properties. These materials are often called correlated materials.

1.2 Correlated materials

Correlated materials are a broad class of compounds whose properties are the result of multiple physical competitions between the charge, lattice, spin, and orbital degrees of freedom [1, 2, 3, 4]. The correlation of electrons in these solids produces a rich variety of states, typically through the interplay between magnetism and electrical interactions. Over the years, large research efforts has been devoted to understand correlated materials. Most of them have been encouraged by the technological opportunities that these materials offer. For example, this includes the phenomenons such as high-temperature superconductivity discovered by Bednorz and Müller in 1986 [5, 6], the control of the insulator to metal (IMT) phases on demand for switching applications, among others, and even the control of colossal magnetoresistance which allows for a large changes in resistance upon the application of the magnetic field [7, 8, 9], and which can have impact on data storage technologies.

Most correlated materials are transition metal oxides (TMO). These compounds present some of the most interesting phenomena observed in condensed matter, which arise from the complex interplay of electronic, magnetic and lattice degrees of freedom [10, 11]. For example, Figure 1.2 shows a phase diagram of a typical transition metal oxide, where different phases such as metal, insulator or high-temperature superconductivity can be reached by varying the temperature or changing the doping level of the material. The sensitivity of these materials to external stimuli is closely related to the electronic structure [3, 12] which, as a first approximation, the electronic structure can be understood by the crystal field theory.

Crystal field theory considers the way in which the repulsions that the anions exert on the electrons of the cation can depend on the orbital in which they are found. Let us consider a V^{3+} ion in a spherical potential. Due to the high symmetry, the 3d levels retain the fivefold degeneracy of the isolated ion (Figure 1.3a). However, these transition metal ions are usually surrounded by six oxygen ions (O^{2-}) making octahedron, which give rise to a crystal-field potential (the total Coulomb potential of electrons from each la ttice site) that reduces the symmetry and the 3d orbitals are split in energy into threefold-degenerate t_{2g} states, built from the d_{xy}, d_{yz}, and d_{zx}, and twofold-degenerate e_g states, comprising the $d_{x^2-y^2}$ and $d_{3z^2-r^2}$ (Figure 1.3b). Due to the Jahn-Teller effect, a local deformation of the octahedron, elongates the crystal in the xy plane and compresses it along the z-axis, the degeneracy is decreased, so the

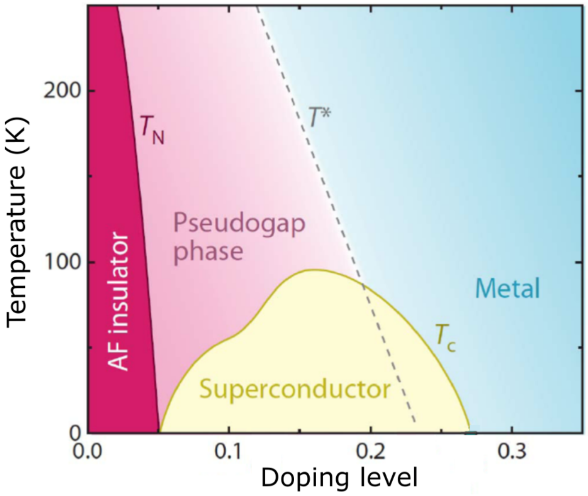

Figure 1.2: **Phase diagram of a typical transition metal oxide.** The ground state of many TMOs are antiferromagnetic insulators below the Néel temperature, T_N. This order can vanish with a change on the doping level or changing the temperature below the critical temperature, T_c, leading to new phases such as superconductivity or metallic. Reproduced from [13].

energy of the system decreases (Figure 1.3c) [1, 14, 15].

However, although this theory works, it has a limitation to explain why some correlated materials are expected to be metals but are actually insulators. One effort to solve this problem can be found in the Mott-Hubbard model and Peierls distortion models which show capture the basic concepts of the relative contributions of electron-electron and electron-phonon interactions.

Mott-Hubbard model

Mott proposed to include the electron hopping between neighbouring sites and the Coulomb repulsion of electrons at the same site. The Coulomb repulsion accounts for the usually neglected (or underestimated) electron correlation. Electron correlation means that electrons do not move independently of each other but feel their pairwise repulsion [16]. The Hubbard Hamiltonian is given by the expression [17]

$$\mathrm{H} = \sum_{\mathrm{ijk}} \mathrm{t_{ij} c^{\dagger}_{i\sigma} c_{j\sigma}} + \mathrm{U} \sum_{\mathrm{i}} \mathrm{n_{i\uparrow} n_{i\downarrow}}$$

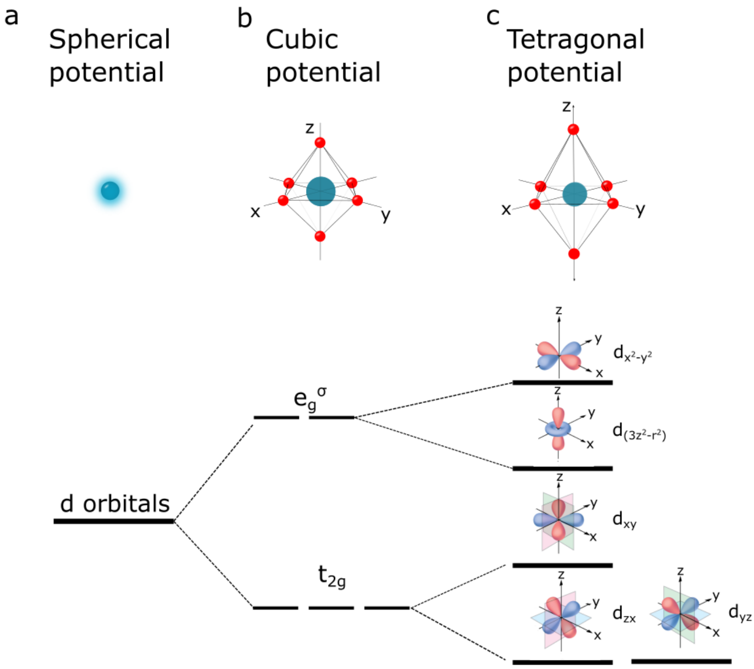

Figure 1.3: **Schematic energy levels of the d-orbitals in a transition-metal ion.** a) The 3d states are five-fold degenerate in a spherical potential. b) When the ion is located within a cubic potential, the d-orbitals are split into twofold-degenerate e_g orbitals and threefold-degenerate t_{2g} orbitals. c) A distortion of the cubic potential along the z-axis, makes the potential change into a tetragonal potential. The orbitals $d_{x^2-y^2}$, $d_{3z^2-r^2}$, d_{xy}, d_{zx}, and d_{yz} are represented over its corresponding states.

where U is the potential energy emerging from the charges on the electrons, t_{ij} is the hopping energy, $c^\dagger_{i\sigma}$ and $c_{j\sigma}$ are the fermion creation and annihilation operators for an electron with spin σ on site i, and $n_{i\sigma} = c^\dagger_{i\sigma}c_{j\sigma}$ is the related ladder operator counting the occupation on site i. In the case U=0, this model reduces to the tight binding model and states that the system is metallic if there is one electron per lattice site. However, if $U > t$, the electronic repulsion can localize the charges and open a gap in the electronic density of states at the Fermi level producing an insulator. These materials are known as Mott insulators.

Peierls distortion

An alternative explanation was provided by Peierls where the crystallographic distortion and electron-phonon interactions are responsible for determining the specific behaviour of the materials. Peierls showed that a half-filled 1D metal is unstable against a structural distortion transforming the metal into an insulator [18]. The electronic dispersion relation for a half-filled band is shown in Figure 1.4. The independent electrons occupy half of the available states up to the Fermi-surface and the material is conducting.

Nevertheless, if the material distorts, forming dimerized pairs as shown in Figure 1.4, the period of the lattice will double to contain two of the previous lattice points. The doubling of the lattice period corresponds to a halving of the Brillouin zone. This opens a gap at the Fermi-surface causing the material to become an insulator. Peierls showed that, for a one-dimensional material, the reduction in energy for the electrons at the Fermi-surface would be larger than the increase in elastic energy required to cause the distortion.

Therefore, there is a significant debate in concluding what is the role of the different degrees of freedom and which of them are the dominant one in the transition phase. For example, many different phases can be achieved by changing the relative strengths of the couplings. In this way, for instance, electron-phonon coupling or a reduction of the electron bandwidth, can modify the Coulomb repulsion to generate an attractive interaction between electrons. This is the force behind the formation of Cooper pairs and is responsible for conventional superconductivity. Understanding the coupling between electrons, lattice, spin and orbital degrees of freedom is vital for determining the properties. Practical control of these properties is a precondition for exploiting quantum advantages in new photonic, electronic and energy technologies.

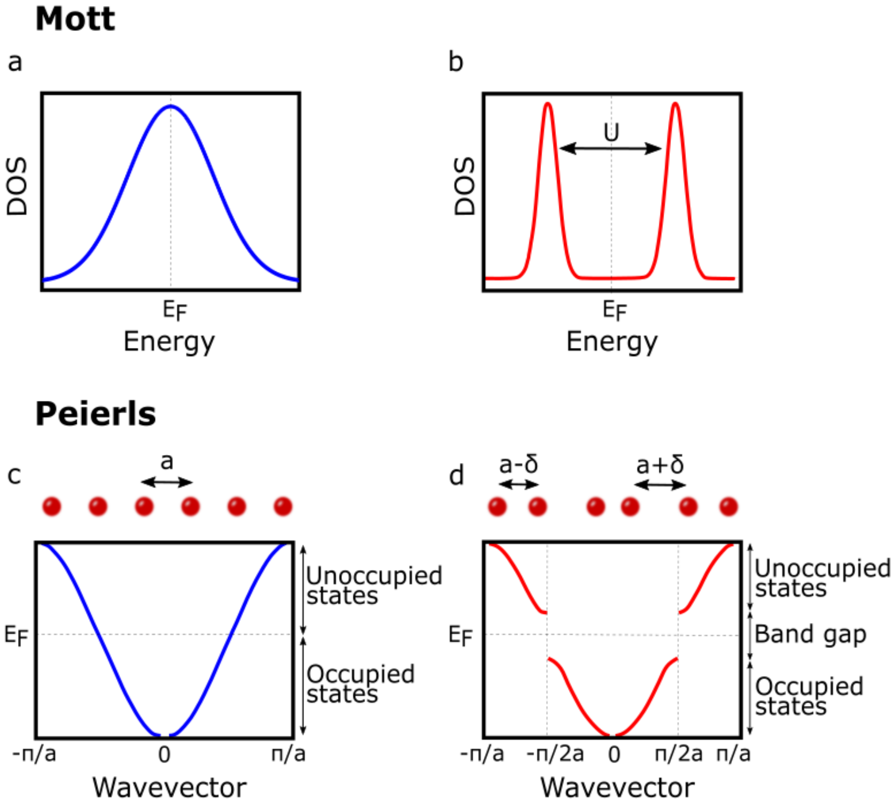

Figure 1.4: **Mott vs Peierls competition**. a) In the metallic phase, large screening leads to delocalized bands with large bandwidths. b) Screening reduction gives rise to Coulomb interactions, which localizes charges open a gap in the electronic density of state at the Fermi level leading to the insulating phases. c) In the metallic sate, the band is half-full in a periodic lattice, with lattice constant a. d) If the lattice distorts, doubling the unit cell, the Brillouin zone halves. The Fermi level is now located in a gap, leading the material to the insulating phase. Adapted from [19].

1.3 How to control correlated materials

The number of valence electrons available is important to define and control the properties of the correlated materials, as it has been discussed in the previous section. Thus, the properties of correlated materials can be modified by chemical doping. In this way, by introducing ions with a higher or lower valency new phases can be stabilised, leading to new material properties [20]. What is most interesting is that the different phases of matter are usually separated by relatively small energy difference. As a consequence, phase transitions into states with completely different properties can be induced with small external perturbation [21, 22, 23].

1.3.1 Photo-excitation: a route to fine control

While chemical doping offers a way to stabilised different phases in equilibrium, photo-excitation provides an alternative way to control the properties of correlated materials out of equilibrium. Exciting the materials with light can have different effects on them, ranging from merely exciting carriers across a band gap to inducing structural phase transitions. These effects can be studied in absorbing materials, where photons from a short and intense laser pulse couple to valence electrons. Photo-excitation changes the charge distribution leading to changes in the dielectric function which, subsequently, will affect to the reflectivity of the material. Moreover, the electronic redistribution within the solid generates a force into the lattice. The restoring forces experienced by the ions upon their perturbation are dictated by the superposition of the phonon modes of the lattice potential. When the force is generated by an impulse-like excitation, with a duration shorter than the period of the phonons, coherent motions of the lattice are induced. Given that phonons modulate the dielectric function of the material, these vibrations can be measured in the time domain through the transient reflection or transmission of the solid. When the symmetry of the system changes, as it happens upon a structural transition, the number and frequencies of the modes also typically change. This way, phonon modes can be employed as a signature of the current phase of the system.

By the early 1980s, Shank *et. al* [24] were among the first to investigate the early timescale dynamics of photo-induced optical absorption in a highly excited semiconductor using femtosecond laser pulses. This measurement was followed by the time-resolved study of the energy transfer to the crystal lattice and the dynamics of the phase transition to the melted state induced by a femtosecond-pulse in silicon [25].

Years later, at the beginning of the 90's, Yu *et al.* [26] were one of the firsts to coin the term "photodoping" since they observed that the properties of correlated materials could be changed by photo-excitation in a similar way to those induced by chemical doping. This comparison was first made in a single crystal of $YBa_2Cu_3O_{7-\delta}$.

In the 2000s, and almost 20 years after the first ultrafast melting experiment, Cavalleri *et al.* reported using ultrafast X-ray probes in VO_2 [27] the first direct measurement of a femtosecond solid-solid phase transition and the combined measurement of electronic and structure dynamics in a correlated solid. Nowadays, probing correlated materials by X-ray free electron pulses is one of the most used approaches due to recent development of extremely bright and coherent-ultrafast X-ray pulses which is enabling more insights into the roles of coherence and disorder in the lattice after photo-excitation [28, 29, 30, 31].

Thanks to X-ray it has been possible to improve our knowledge of the exotic physics of technologically relevant materials. However, despite the advantages of X-rays, there are only a few facilities in the world and, as a result, the number of experiments that can be performed are limited. In contrast, one powerful technique available to us to perform measurements in a systematic manner is optical pump-probe spectroscopy. Since early work, this methodology has reach unprecedented reproducibility and reliability due to the advances on the development of pulse chirp amplification and the availability of commercial lasers. The technique relies on the measurement of changes in reflectivity and transmittance as a function of a delay between two, generally, optical pulses. As of today, it is possible to measure with attoseconds time-resolution allowing us to capture processes on their fundamental timescales. Moreover, a wide range of energies, from ultraviolet to terahertz, are accessible, providing detailed information about how the dielectric constant can change as a function of the energy scale. This versatility allows us to obtain information that complements and can serve as a guide for experiments like those performed at XFEL. However, such versatility also brings with it significant experimental challenges, such as identifying a reliable 'marker' for a specific degree of freedom or a photo-excitation process. This is particularly important to understand the physics behind correlated materials in which the photo-excitation event can launch multiple and competing phenomena, all of which can change the optical constants in a similar way. Often, in the literature, characterization of light driven changes in phase-changed materials is performed using a single probe wavelength approach and in a limited range of experimental conditions. In particular, most experiments are performed at 800 nm probe wavelengths, corresponding to the output of Ti:Sapphire lasers, ignoring other energy scales. Consequently, these experiments provide only a limited view of how the dielectric constant changes and thus hinder a full mapping of the photo-induced process. In this thesis, we directly address this problem by recording the transient optical response using a broadband spectroscopy at multiple experimental conditions such as temperature, fluence and time delays in order to identify reliable fingerprints for phase transitions and elucidate the interplay between different degrees of freedom.

1.4 Thesis structure

In this thesis, we measure the transient optical response on two prototypical Mott insulator compounds ($Sr_3Ir_2O_7$ and V_2O_3) which present electronic, structural and magnetic phase transitions. The thesis is structured as follows:

- **Chapter 2** describes in detail the experimental setup and discusses the procedures to collect reproducible and high quality pump-probe data.

Chapters 3, 4 and 5 focus on the study of the prototypical spin-orbit Mott insulator $Sr_3Ir_2O_7$:

- **Chapter 3** provides an introduction on $Sr_3Ir_2O_7$, discussing the current state of the research.

- **Chapter 4** studies the electronic and structural properties of $Sr_3Ir_2O_7$ by studying how photo-excitation alters the reflectivity at a wide range of energies. In addition, it is shown the evolution of the phonon modes with fluence and wavelength.

- **Chapter 5** shows how photo-excitation of $Sr_3Ir_2O_7$ can non-thermally suppress the magnetic long-range order. We can distinguish between different regimes, where the system can recover within a picosecond and, another regime in which the magnetic order is completely suppressed for long times while the lattice temperature remains below the transition temperature. We suggest how this crossover emanates from the generation of photo-induced spin defects that enable a pathway for spin disordering and long-lived breaking of magnetic order.

Chapters 6 and 7 are centred on the research performed in the transition metal oxide V_2O_3:

- **Chapter 6** gives an introduction on the physics of V_2O_3, presenting its electronic and crystal structure and a brief description of its phase diagram. This chapter continues with the comparison of the A_{1g} phonon mode of the metallic V_2O_3 measured by two different techniques, Raman spectroscopy and time-resolved reflectivity. The good agreement on the frequency of this mode by these two different measurements allows us to conclude that there is no light-induced hardening of the A_{1g} phonon mode as previously claimed in the literature.

- **Chapter 7** tracks of the ultrafast phase transition in V_2O_3. This chapter also shows the difficulties found to measure on a V_2O_3 single crystal and how this problems are solved by using thin films. Our results suggest that damping and dephasing rates are a dominant factor when looking at the dynamics of the coherent phonons in the phase transition.

- Finally, **chapter 8** summarizes the main achievements of the thesis.

Chapter 2

Experimental methods for ultrafast broadband spectroscopy

This chapter presents the experimental techniques and experimental setup we have used throughout this thesis. Section 2.1 explains the pump-probe spectroscopy technique. Section 2.2 describes our experimental setup and laser light system which acts as the pump and probe beams. Section 2.3 explains the physics of Raman spectroscopy, as well as the description of the Raman microscope that we have used.

2.1 Pump-probe spectroscopy

One of the most common experimental techniques to study ultrafast dynamics is the pump-probe spectroscopy. In this method, a stronger beam (the pump) excites the sample, initiating some dynamics. After some time Δt, a weaker beam (the probe) monitors the changes induced by the pump. The probe beam can either be X-ray radiation, electrons (for electron diffraction or photoemission) or radiation in the ultraviolet-visible (UV-VIS), visible, infrared (IR), and terahertz (THz) region, depending on the type of information of interest. This method is a stroboscopic technique where each pulse captures the properties of a material in an instant. In order to measure the temporal evolution, the material must respond in a repeatable way. If this is the case, the delay between pump and probe pulses can be varied, and the experiment can be repeated with different delays to map out the temporal response of the system.

To control the arrival time of the pump and probe, the path length of one of the two beams is varied. For optical pump-probe experiments, this can be done with a retro-reflective mirror system on a motorized translation stage. This way, if the mirrors are translated by a distance x, the additional length travelled by the laser beam is $2x$ which induces a delay $\Delta \mathrm{t} = 2\mathrm{x}/\mathrm{c}$, where c is the speed of light. Hence, in order to achieve a time delay of 1 ps between both beams, the additional distance that one of the beam has to travel is 150 µm. In the ideal case, the time resolution would be established by a delta function, however, it is given by the pulse width obtained directly from the laser, which usually has a value around 30-50 fs.

Depending on the experimental geometry, we can measure the reflectivity or transmission of the sample in the pump-probe experiment. For highly absorbing samples, the direct data from the transmission is easier to interpret since it is related to the absorption of the sample, while the reflectivity has a more complex dependence on the fundamental properties of the material. However, transmission experiments can only be performed on thin transmissive materials. Thick, large and high absorbing samples limit the amount of light that reaches the detector, complicating data collection. As a consequence, reflectivity is often the geometry of choice, especially for the study of single crystals.

The signal to noise ratio in pump-probe experiments is determined by the amount of photons that arrive to the detector. To improve the signal to noise ratio we need to accumulate multiple laser shots per each delay. In addition, the use of a chopper will also improve the signal to noise ratio since it allows us to remove many of the fluctuations, i.e., if the system has noise at 1 Hz, and we chop at 1 kHz, we get 1000 samples of on and off within that fluctuation in the probe power, so that drift cancels out.

2.2 Experimental setup

2.2.1 The laser system

In this thesis the Ti:Sapphire Legend Elite Duo laser supplied by *Coherent* is used. The central wavelength of the laser is 800 nm, with 40 nm bandwidth and a pulse duration of close to 35 fs with an energy of 1 mJ and 5 kHz repetition rate. A fraction of the laser output is reduced in size by a factor of 3 using a telescope and directly sent into the pump-probe measurement setup (Figure 2.1). This laser light will be used as the pump as well as to generate a broadband visible supercontinuum (probe).

2.2.2 Pumping

All the experiments performed in this thesis using broadband spectroscopy are done in the same pump-probe experimental setup (Figure 2.1). The pump comes from the transmitted light of the beam splitter at the entrance of the setup. Its pulse energy is controlled by a half wave plate (λ/2) which is mounted on a motorized rotation stage that rotates the polarization of the 800 nm beam relative to a Brewster polarizer. After this, the beam goes through a chopper

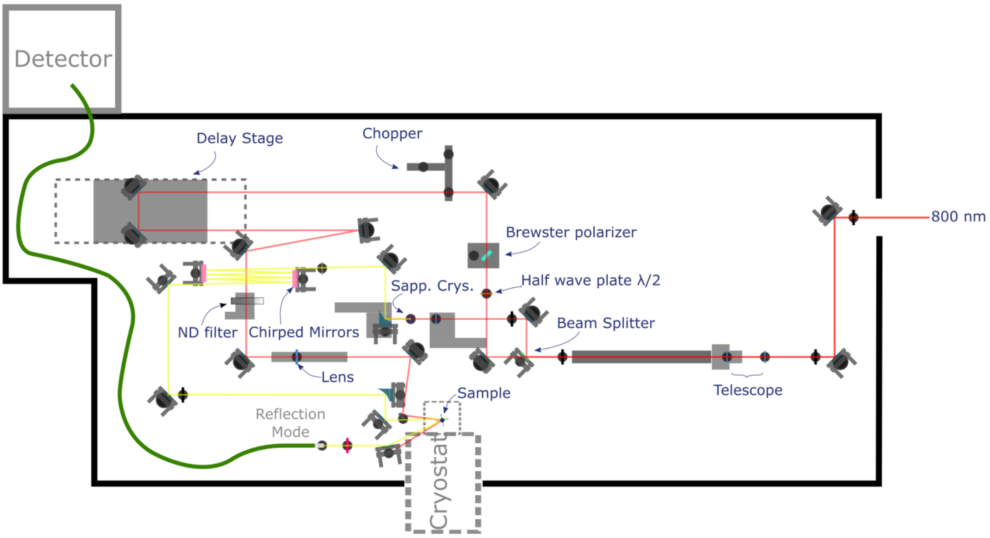

Figure 2.1: **Schematic pump-probe experiment setup.**

and to a delay stage which is used to control the arrival time difference between the pump and probe beam to the sample. In order to ensure a pump spot larger than the probe spot, a lens is adjusted so that the focus is behind the sample. That pump spot size is measured by a CMOS camera that records an image of the beam. The beam profile is fitted by a Gaussian shape (left side Figure 2.2) in order to obtain the full width at half maximum (FWHM). This value is used to calculate the beam area as $A = \pi r^2$. In all the experiments reported in this thesis the probe size is made 10 times smaller than the pump size in order to ensure probing of a homogeneously pumped region.

The fluence (energy per unit of area) is calculated as

$$F = \frac{P_{laser} \cdot \cos(\vartheta_i)}{f_{laser} \cdot \text{beamsize}}$$

where P_{laser} is the power of the laser on the sample site at each half wave plate angle in the setup; ϑ_i is the incident pump angle on the sample; f_{laser} is the laser repetition rate. Figure 2.2 shows a typical simulation of fluence vs. the half wave plate angle.

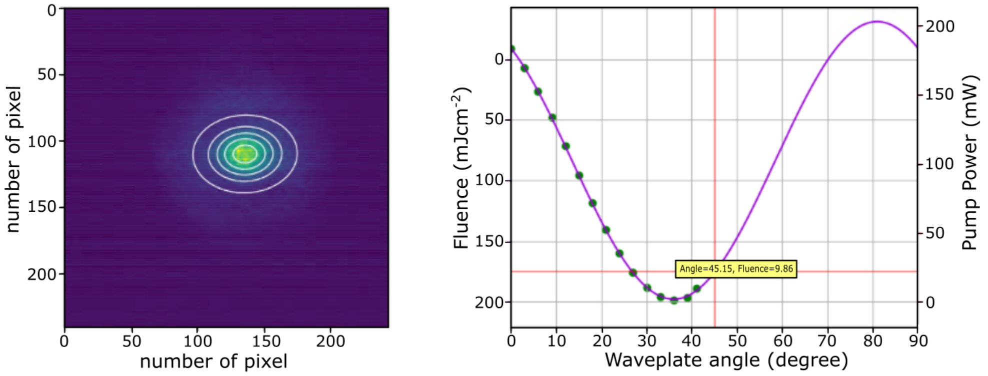

Figure 2.2: **Spot size and fluence calculation of the 800 nm beam.** Left: Spot size calculation. The image of a beam is fitted by a Gaussian shape. Right: Fluence value vs waveplate angle. The green dots are real fluence values while the purple line is a simulation.

2.2.3 Probing

In this thesis, broadband visible light is used as the probe. This light is generated by focusing the 800 nm beam into a sapphire crystal. A supercontinuum of frequencies is generated in the crystal by a complex nonlinear process relying on the optical Kerr effect and self phase modulation. The optical Kerr effect in the sapphire crystal results in an intensity-dependent refractive index of the third order susceptibility, which, for ultrashort pulses, means that the refractive index varies in time, adding an instantaneous phase to the pulse. This phase $\varphi(t)$ shifts the frequency of the field $\omega = d\varphi(t)/dt$: the early part of the pulse is red shifted, while the trailing edge is blue shifted, as a consequence the spectrum is broadened.

After generation, the white light goes to an off-axis parabolic mirror placed on a linear translation stage. To ensure the beam is collinear, it can be sent over a long distance to check the alignment as shown in Figure 2.1.

In order to correct the broadening of the pulse produced at the crystal and at other optical components, the collimated beam is sent into a pair of chirped mirrors. These mirrors are made of dielectric dispersive materials with a series of layered coatings through which some colours penetrate deeper than others. This changes the distance travelled by each colour and reduces the positive dispersion. The chirped mirrors located in the pump-probe setup have a wavelength range of 450-950 nm and a reflectivity greater than the 99.2%. The group delay dispersion (GDD), i.e. the frequency dependence of the group delay, is -55 fs^2 at 700 nm. For experiments in which the sample was under laboratory conditions (i.e., held only by a holder without any other glass) 3 bounces were required to correct the chirp. In contrast, for experiments using a cryostat, 4 bounces were required to compensate for the extra fused silica windows. Figure 2.3 shows a comparison on the relative reflective signal before and after adding the chirped mirrors as measured in the pump-probe setup.

After the chirped mirrors, the white light beam is focused onto the sample using an off-axis parabolic mirror. In some experiments in this thesis, the sample is placed inside a liquid Nitrogen (LN_2) cryostat which allows to control the temperature between 77 K and 500 K, the pressure is kept in the order of 10^{-6} mbar. The cryostat cavity is made of four windows, three thick ($\approx$ 2mm) and one thin ($\approx$ 500μm). The thick windows are placed on the back and the sides, while the thin window is usually placed at the front. The rear window is used for transmission measurements while the sides windows are used for

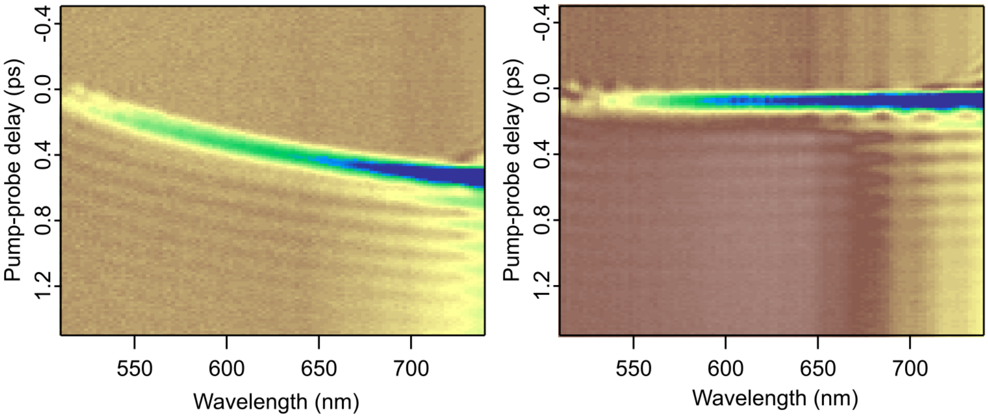

Figure 2.3: **Chirped correction of a broadband visible beam.** The images show a comparison on the relative reflective signal before and after adding the chirped mirrors.

reflective measurements where the pump incident angle is 45°.

The reflection of the probe beam from the sample is focused with an achromatic lens into a glass fiber located on a linear manual translation stage to facilitate an efficient coupling. The glass fiber drives the light into a spectrometer with a Czerny-Turner design which separates the wavelengths of the white light. The intensity of the light is measured by each pixel of a sCMOS camera. To control the amount of light coming into the camera and avoid the saturations of the pixels, a slider slit is used.

For optimal acquisition, the light has to be centered into the camera and be distributed as much as possible at every wavelength, as shown in Figure 2.4a. This is required to avoid any possible artefact in the R_{on}/R_{off} spectrum. Experimentally, higher signal stability and reproducibility was obtained when the intensity on the camera increased smoothly from lower to higher wavelengths without any abrupt change as shown in Figure 2.4b. In most cases, it was found that poor spectra quality could be fixed by adjusting the compression of the 800 nm laser pulse. Changing the polarization of the beam by rotating the angle of the sapphire crystal was also found to significantly impact the signal stability.

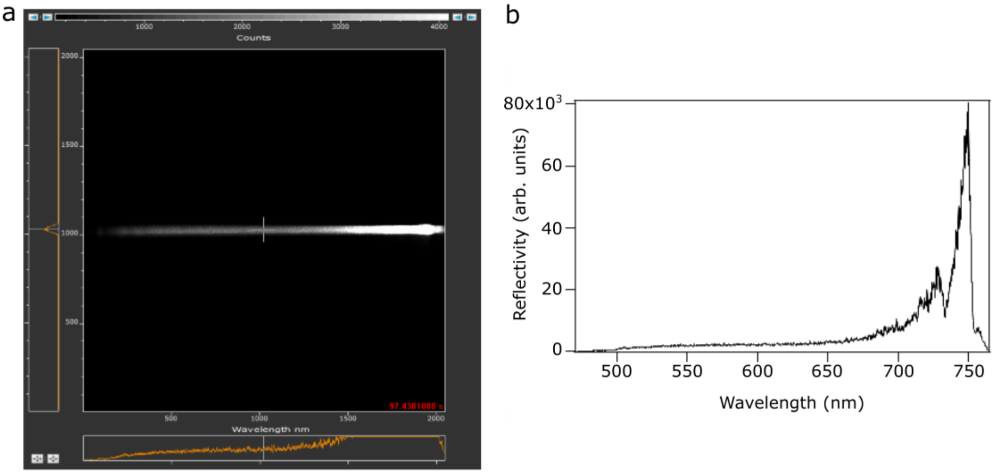

Figure 2.4: **Characterization of the white light.** a) Light distribution on the Andor camera. b)broadband spectrum. To have most light on the system as possible below the saturation level, at least an average count number of 2500 at the same time delay point is used, thus will improve the signal to noise ratio of the data.

2.2.4 Detection

Due to the synchronization between the detector and the laser was non-trivial, we have used two different detection schemes throughout this thesis.

Detection scheme 1:

On the first detection scheme, it is compound by a *iXon* Andor camera that reads at 500 Hz. However, the laser fires 5000 pulses per second, thus is not possible to read every laser pulse. To ensure synchronization, the camera was configured to read in groups of 10 pulses. To achieve this, first the *laser* trigger is connected to a *frequency divider*, which divides the frequency by a factor of 20 (5000/20=250 Hz). The signal that the frequency divider generates is connected to the trigger of the *chopper*. In this way the chopper cuts half the laser pulses (producing pump on and pump off). Subsequently, the signal generated by the chopper is connected to a *delayer* that has 2 channels, *A* and *B*, which multiplex the signal. Signal A activates when the chopper is not blocking the laser (pump on). Signal B activates 2 ms later (i.e. the time every ten pulses thus corresponding to pump off). The signal between every bunch of 10 pulses are used to trigger the camera as shown in Figure 2.5a. This configuration ensures that the first 10 pulses always correspond to the sample excited (pump on) and the next 10 pulses correspond to the sample without excitation (pump off). Allowing us to reliably collect R_{on}/R_{off} signals.

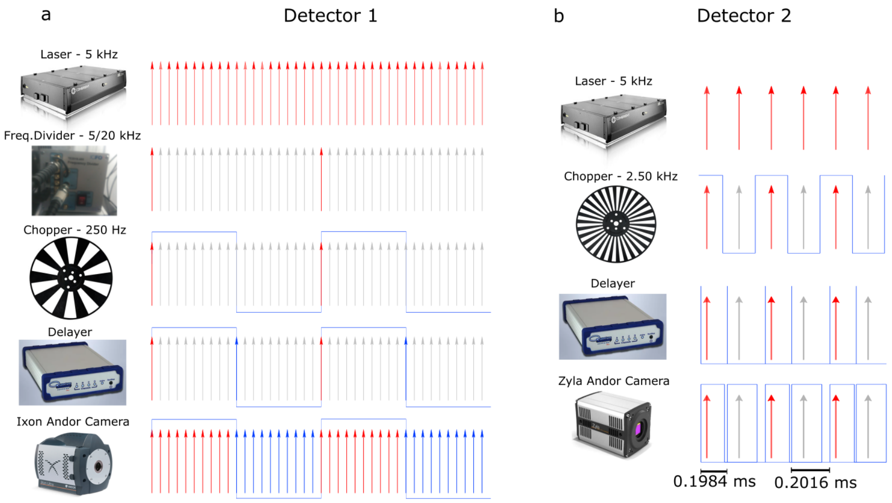

Figure 2.5: **Diagram of the laser-camera synchronization.** The red arrows indicate pump on, and the blue ones are the pump off. The solid blue line are the exposure time.**a** Detector 1 schematic synchronization.**b** Detector 2 schematic synchronization.

One limitation of this data collection configuration is the accumulation of ten consecutive pump on pulses on the sample. If the sample does not fully recover between pulses, heat will start to accumulate. This means that each pump pulse will pump a slightly different state of the system, while each probe pulse will probe a different state as indicated in Figure 2.6. This different sates will then be averaged together.

Detection scheme 2:

To avoid this problem, during the course of this thesis a *Zyla* Andor camera was acquired. This camera reads at 5 kHz, and thus collects one pulse *on* and one pulse *off* (Figure 2.6b). With this new configuration, the trigger laser is connected directly to the chopper and the camera (Figure 2.5b): The laser trigger is connected to a faster chopper that runs at 2.5 kHz. In this case, as the blades of the chopper are closer, two cylindrical lenses focus the beam through the chopper to avoid any beam clipping. The full time delay between two consecutive on pulses (or off pulses) is 0.4 ms. Then, for every signal from the chopper, the delayer generates two new signals: Signal 1 at the frequency of the chopper and signal 2 at $\Delta = 0.2016$ ms, which leaves one pair spaced by 0.2016 ms and another by 0.4 ms – 0.216 ms = 0.1984 ms. The camera records the time between the signals from the delayer, so if the time is short, i.e. it measures 0.1984 between pulses, it knows that the first pulse was the laser off pulse and the second was the laser on, in this way, the delayer is always on.

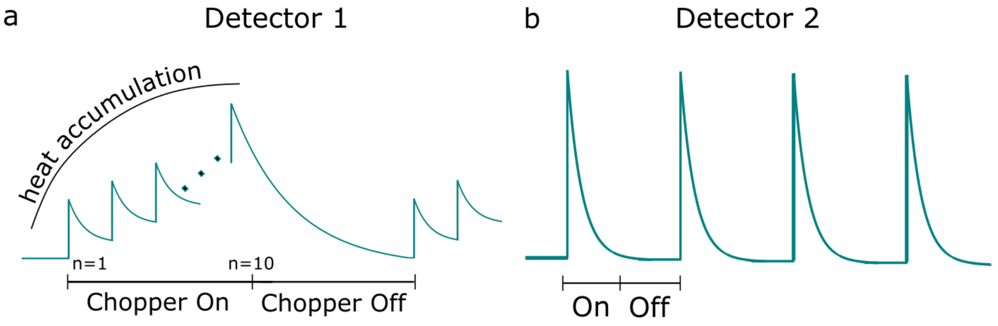

Figure 2.6: **Diagram of the heat accumulation on the sample.** a) Shows the heat accumulation of ten consecutive pump *on* pulses on the sample through the configuration of detector 1. b) Using the configuration of detector 2, the system will develop a new equilibrium in which each pump pulse will pump the system in the same state.

2.3 Raman spectroscopy

Raman spectroscopy is a straightforward and non-destructive useful technique to identify a wide range of materials. This technique involves illuminating a sample with monochromatic light and using a spectrometer to examine light scattered by the sample. In this thesis, we rely on Raman spectroscopy to do a first characterization of the single crystal. This technique is used to determine the low-frequency modes such as the vibrational or rotational modes of systems.

At the molecular level, photons can interact with matter by absorption or scattering processes. Scattering may occur either elastically or inelastically. The elastically process is termed Rayleigh scattering, whilst the inelastic process is termed Raman scattering. The electric field component of the scattering photon perturbs the electron cloud of the molecule and may be regarded as exciting the system to a virtual level. Raman scattering occurs when the system exchanges energy with the photon (Figure 2.7), and the system subsequently will emit or absorb a phonon with energy $h\nu_p$. The frequency shift corresponding to the energy difference between the incident and scattered photon is termed the Raman shift. Depending on whether the system has lost or gained energy, the Raman shift occurs either as an up-or down-shift of the scattered photon

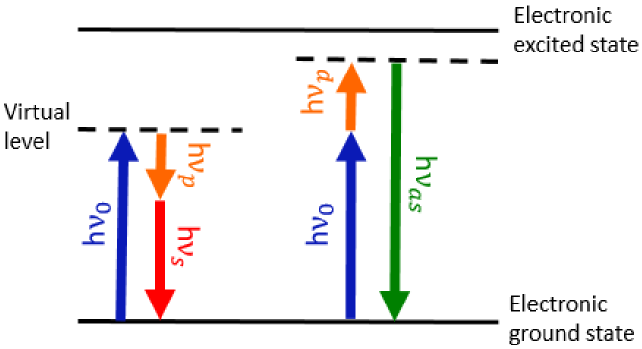

Figure 2.7: **Raman scattering by of light by phonons.** Light can be inelastically scattered by the creation of phonon and the emission of a lower energy, stokes photon, or by the absorption of a phonon and the emission of a higher frequency anti-stokes phonon. Non-resonant Raman scattering occurs when transitions are to virtual levels.

frequency relative to that of the incident photon. The lower energy photon scattered an energy of $h\nu_s = h\nu_i - h\nu_p$ is called the stokes photon, while the higher energy photon with an energy $h\nu_{as} = h\nu_i + h\nu_p$ is the anti-stokes photon. A plot of detected number of photons versus Raman shift from the incident laser energy gives a Raman spectrum. Different materials have different vibrational modes, and therefore characteristic Raman spectra.

In Raman spectrometers, lasers are used as a photon source due to their highly monochromatic nature and high beam fluxes. The Raman spectroscopy results presented on this thesis were performed using a Renishaw inVia™inSpect confocal Raman microscope provided by ICFO (Figure 2.8). The setup consists of two possible laser sources, one at 532 nm of central wavelength at 100 mW of power and, another source at 785 nm of central wavelength at 300 mW. The beam is guided through a series of mirror that focuses the light into the microscope that shine the light on the sample and collect the scattered light. Then, as the Raman effect is much weaker than the Rayleigh scattered component, the beam goes into Rayleigh rejection filters that are used to be able to detect the Raman effect. After this, the Raman scattered light is focused through a

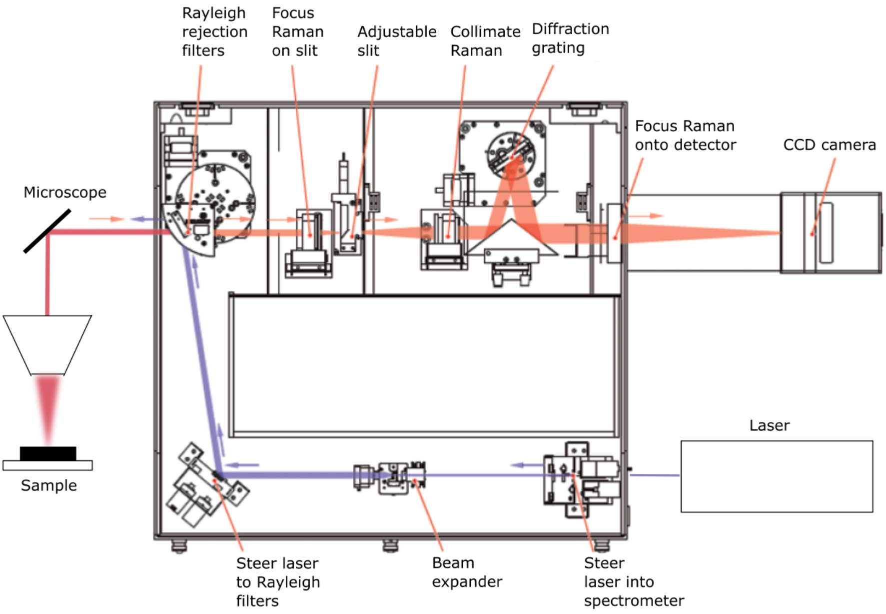

Figure 2.8: **Schematic Raman spectroscopy setup.** Adapted from [32].

slit (100 µm width) and is dispersed by a diffraction grating. Finally, a CCD camera detects the inelastic scattered light.

Chapter 3

Electronic and magnetic properties of Iridium-based oxides

This chapter presents the physical properties of Sr_2IrO_4 *and* $Sr_3Ir_2O_7$*, from which the control of the magnetic order can be studied. Section 3.1 explains the importance of 5d TMOs in a short introduction. The crystal and electronic structure of two of the most studied 5d TMOs compounds,* Sr_2IrO_4 *and* $Sr_3Ir_2O_7$*, are discussed in Section 3.2 and Section 3.3, respectively. The study of the static and dynamic magnetic properties through innovative techniques using X-rays are discussed in Section 3.4. In addition, this section shows relevant studies on the changes of the phonons with temperature.*

3.1 Introduction

The breakdown of antiferromagnetism in Mott insulating transition-metal oxides (TMOs) through doping gives rise to a broad range of novel and complex properties. Among them we can highlight high temperature superconductivity in cuprates or the colossal magnetoresistance in manganites [5, 8]. In these materials, electrons, spins, and phonons strongly interact to dictate the material properties. Most initial work focused on *3d* electron systems, however recently *4d* and *5d* TMOs have emerged where strong spin orbit coupling also competes with the other degrees of freedom to enable even more complex phases. Among these oxides, iridium-based *5d* TMOs has attracted considerable attention. The research has been driven by the similarities of this materials with superconducting cuprates [34]. The main difference between these two kind of compounds emanates from the fact that while the orbitals in iridates are *5d*, the cuprates are *3d*. This open the exotic opportunity of control the magnetic order due to its strong spin-orbit coupling that may have a strong influence on the coupling to phonons.

In this chapter, I provide an introduction to the crystal and electronic structure, and a first overview of the magnetic properties of two of the most studied iridates samples, $\mathrm{Sr_2IrO_4}$ and $\mathrm{Sr_3Ir_2O_7}$. These undoped compounds exhibit a phase transition from paramagnetic to antiferromagnetic at $\mathrm{T_N} \approx 240$ K for the former compound, and $\mathrm{T_N} \approx 280$ K for the latter. The low-energy properties of these materials have been well-studied experimentally thanks to the rapidly developing resonant X-ray magnetic scattering technique as well as some experiments based on the characterization of the phonon modes. The understanding of demagnetization process in these different systems is particularly important because antiferromagnetic order breaks down, through chemical doping, into technologically-relevant phases. Our ability to manipulate antiferromagnetic order with light is key to stabilise those phases on demand.

3.2 Structure: Ruddlesden-Popper series

The iridates belong to the Ruddlesden-Popper phases that are a series of compounds whose chemical form is generally given by $\mathrm{A_{n+1}B_nX_{3n+1}}$, where A and B are cations and X is an anion [35, 36]. The subscript n represents the number of layers in the system from which one Ruddlesden-Popper member will be distinguished from another of the series. Therefore, numerous crystal lattices with the stacks containing octahedra show some perovskite features as it is shown in Figure 3.1[37]. For iridates, Sr occupies the A site, Ir takes the B place and O is site in X.

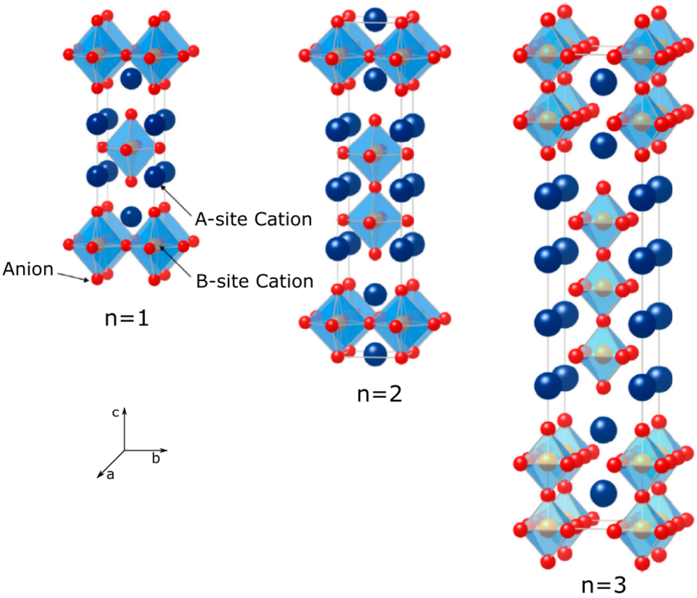

Figure 3.1: **Ruddlesden-Popper phases.** For iridates $\mathrm{Sr_{n+1}Ir_nO_{3n+1}}$, the A-site Sr atoms are shown in dark blue, B-site Ir atoms are in orange in the centre of the octahedra which are surrounded by the Oxygen atoms in red. Taken from [37].

This structure can be manipulated in two ways that have a strong impact on the key material properties:

Dimensional control:

There is a change as a function of dimensionality for a fixed anion and cations types, this is, just changing the number of layers n, one can drive the material property such as the Morin transition observed when the iridates evolve from insulators (n = 0) to metal (n = ∞) associated with a change on the electronic structure as well [38, 39, 40]. In particular, two materials have received more attention, the monolayer Sr_2IrO_4 and the bilayer $Sr_3Ir_2O_7$.

Doping control:

The A site can be alloyed to drive a phase transition as it is the case for the bilayer iridate $Sr_3Ir_2O_7$, where substituting Sr for a fraction of La can suppress antiferromagnetism and force the insulating gap to close [41].

Thus, given the different variety of physics manifest in these compounds, it shows the Ruddlesden-Popper family of compounds represent an ideal platform for investigating new frontiers of condensed matter physics.

Crystal structure of iridates

The iridates consist of layers of corner-sharing oxygen octahedra with one Ir ion at the centre and which are separated by Sr atoms. The octahedra are slightly elongated along the crystal c-axis (Figure 3.1). The corresponding lattice parameters of each compound are summarized in Table 3.1. These values were obtained from Neutron powder diffraction technique on Sr_2IrO_4 [42], and from X-ray diffraction experiments on the $Sr_3Ir_2O_7$ compound [43, 44, 45].

Compound	Space group	a=b (Å)	c (Å)
Sr_2IrO_4	$I4_1/acd$	≈ 5.499	≈ 25.781
$Sr_3Ir_2O_7$	$I4/mmm$	≈ 3.896	≈ 20.879

Table 3.1: Lattice parameters of Sr_2IrO_4 and $Sr_3Ir_2O_7$ [43, 44, 45].

3.3 Electronic structure: the role of the spin-orbit coupling

The crystal field splitting of the energy bands and the strong spin-orbit coupling play an important role for the electronic properties of the iridates. According to the free electron model, one could predict that the iridates are metallic. Considering the electronic structure of these compounds, the formal valance charge of Sr atom is +2, while the oxygen ion has a closed shell with a $2p^6$ configuration, and thus is -2; this leaves the Ir ion with a valance of +4 with an electronic configuration of $[Xe]4f^{14}5d^5$, leaving the system with the odd number of electrons per unit cell resulting in a half-filled valence band. However, experimentally both Sr_2IrO_4 and $Sr_3Ir_2O_7$ are insulators [38, 46]. Such contradiction has been understood by taking into account the different energy scales at play. Firstly, the crystal field splits the 5d orbitals ($d_{xy}, d_{xz}, d_{yz}, d_{x^2-y^2}$ and $d_{3z^2-r^2}$) into $t_{2g}(d_{xy}, d_{xz}, d_{yz})$ and $e_g(d_{x^2-y^2}, d_{3z^2-r^2})$ orbitals. Secondly, in the spin-orbit coupling limit, the t_{2g} band splits into effective total angular momentum $J_{eff} = 1/2$ doublet and $J_{eff} = 3/2$ quartet bands. The t_{2g} states will correspond to the orbital angular momentum L=1 states with $\Psi_{m_l=\pm1} = \mp(|zx\rangle \pm i|yz\rangle)/\sqrt{2}$ and $\Psi_{m_l=0} = |xy\rangle$ (Schematic figure of the orbitals on its corresponding energy states is depicted in Figure 1.3 from Chapter 1). In addition, the $J_{eff} = 1/2$ band is sufficiently narrowed, as a result of spin-orbit effects, that even quite modest U is enough to form an upper and lower Hubbard band. With the lower Hubbard band completely filled, and the upper Hubbard band empty, an insulating state is finally attained. For the monolayer compound has been measured a bandgap of 400 meV [47, 48, 49] while for the bilayer compound the bandgap is 130 meV [45, 50].

This extended splitting was first observed experimentally by Kim *et al.* using ARPES technique in Sr_2IrO_4 [47] and it has been subsequently confirmed by RXS experiments [51]. As it is shown in the comparative Table 3.2, the optical transition from $J_{eff} = 1/2$ LHB to the $J_{eff} = 1/2$ UHB has an energy value in Sr_2IrO_4 ($Sr_3Ir_2O_7$) of ~ 0.5 eV (~ 0.35 eV) and from $J_{eff} = 3/2$ to $J_{eff} = 1/2$ UHB, ~ 1 eV (~ 0.8 eV) [45, 52]. The fact that the $SrIrO_3$ compound is a metal is because the bandwidth increases when the number of layers n rises since it is proportional to the number of the neighbouring Ir ions. Thus, the bilayer compound has a small but finite bandgap but when $n = \infty$ like in $SrIrO_3$, all bands are overlapped, causing a correlated metal [39].

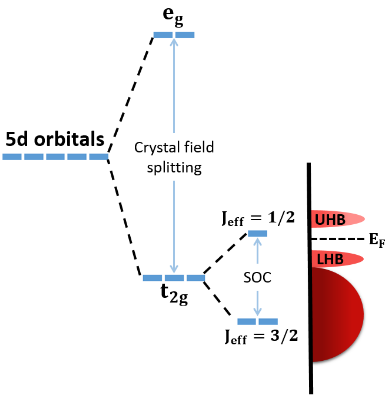

Figure 3.2: **Schematic energy level and band diagram of the** Ir^{4+} **ions.** The d orbitals are split into t_{2g} and e_g orbitals. The Coulomb interactions established a filled $J_{eff} = 3/2$ and half-filled $J_{eff} = 1/2$ Mott state, which is sufficiently narrowed that even a modes U is enough to form a lower Hubbard band (LHB) and an upper Hubbard band (UHB).

	Bandgap	LHB → UHB	$J_{eff} = 3/2 \rightarrow J_{eff} = 1/2$
Sr_2IrO_4	400 meV	0.5 eV	1 eV
$Sr_3Ir_2O_7$	130 meV	0.35 eV	0.8 eV

Table 3.2: Transition energy values of Sr_2IrO_4 and $Sr_3Ir_2O_7$ [45, 47, 48, 50, 52].

3.4 Magnetic properties

The $J_{\text{eff}} = 1/2$ state can also contributes to unusual magnetic behaviours whose emergent physical properties can be drastically different from those of the conventional Mott insulators. A prime example is when $J_{\text{eff}} = 1/2$ is realized in a honeycomb lattice structure where electrons hopping between $J_{\text{eff}} = 1/2$ states acquire complex phase, it generates a Berry phase leading to the recent prediction of quantum spin-Hall effect at room temperature [53], and it also leads to the low-energy Hamiltonian of Kitaev model which is relevant, for example, for quantum computing [54]. Experimental establishment of the $J_{\text{eff}} = 1/2$ state is thus an important step toward these physics [47]. However, it is usually difficult to get the phase information experimentally, because it is always the intensity, the square modulus of the wave function, that is measured; and thus a reference, with which the sate under measurement can interfere, is required. The resonant X-ray scattering (RXS) technique uses resonance effects at an X-ray absorption edge to selectively enhance the signal of interest, and has become a powerful tool for investigating ordering phenomena. The RXS signal contains important information about the phase of the wave function for valence electrons, because RXS results from quantum interference between different scattering paths via intermediate states of a single site. Given this, recent advances on this technique we can distinguish between resonant elastic or inelastic X-ray scattering in the static- or time-resolved domain, equally.

3.4.1 Static magnetic properties

The resonant elastic X-ray scattering (REXS) technique provides a sensitive probe for spatial modulations of spins, charges, and orbitals. This unique sensitivity is achieved by merging diffraction and X-ray absorption spectroscopy (XAS) into a single experiment, where the scattering provides information about spatial modulation and the XAS provides sensitivity to the electronic structure. More precisely, resonant X-ray scattering close to an absorption edge involves virtual transitions from core levels into unoccupied states close to the Fermi level and these virtual transitions depend strongly on the spin, charge and orbital configuration of the resonant scattering centres. Furthermore, the resonance process strongly enhances the scattering cross-section and allows the opportunity to study selected atomic species in a crystal [55]. Kim *et al.* [51]

used REXS to probe the relative phases of constituent atomic orbitals in an electronic wave function, which uncovered the Mott insulating state induced by relativistic spin-orbit coupling in Sr_2IrO_4. The X-ray diffraction intensity is presented in Figure 3.3a as a function of the X-ray energy. It is shown that the intensity is remarkably enhanced around the $L_3(2p_{3/2})$ and $L_2(2p_{1/2})$ edges of around 11.22 and 12.83 keV. The temperature dependences of the REXS intensity at the orbital order reflection are shown in Figure 3.3b. With decreasing temperature, the REXS intensity rapidly increases at about 240 K which corresponds to the magnetic transition. This experiment demonstrates that X-rays can be extended to a new level to probe even finer details of magnetic structure finding important applications in systems such as iridates, where complex phases give rise to novel physics.

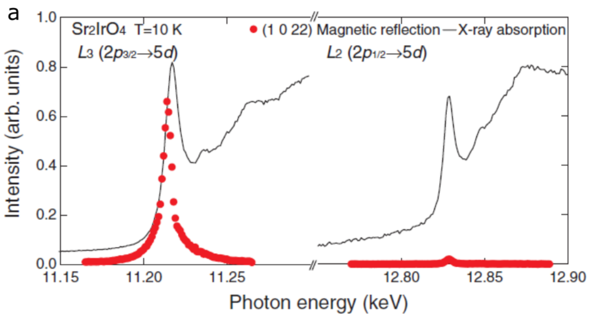

Figure 3.3: **Resonant enhancement of the magnetic reflection (1 0 22) at the L edge of Sr_2IrO_4** a) Solid lines are X-ray absorption spectra indicating the presence of Ir $L_3(2p_{3/2})$ and $L_2(2p_{1/2})$ edges around 11.22 and 12.83 keV. The dotted red lines represent the intensity of the magnetic (1 0 22) peak. b)Temperature-dependent magnetization in the in-plane field of 0.5 T is shown by the solid line. Taken from [51].

A similar technique is the resonant inelastic X-ray scattering (RIXS), which scatters X-ray photons inelastically off matter. The changes in energy, momentum and polarization of the scattered photon are transferred to intrinsic excitations of the material under study, being able to probe many elementary excitations such as crystal-field and orbital excitations, magnons, and phonons among other particles. Besides, the resonance in RIXS greatly enhances the cross-section and adds selectivity to atomic species. In this aspect, RIXS offers a wide landscape in the study of strongly correlated electron system [56]. One of the first experiment using RIXS on Sr_2IrO_4 was done by J. Kim *et al.* in 2012 to map the dispersion of magnons as well characterizing in further detail the so-called spin-orbit exciton attributed to the excitation of a hole across the $J_{eff} = 1/2$ level to one of $J_{eff} = 3/2$ quartet levels. Magnetic excitations in this system are quite well described by a pure Heisenberg model with J=60 meV, J'=-20 meV, and J"=15 meV, which correspond to the first, second, and third nearest *Ir* neighbours respectively [33]. A similar measurement was done later on the bilayer compound $Sr_3Ir_2O_7$ [57] that shows a notable deviation from the Heisenberg model with a large magnon gap of ≈ 92 meV exceeds the total magnon bandwidth of ≈ 70 meV. In addition, they show that 5d oxide with strong spin-orbit coupling and a small charge gap can arise a novel type of magnet different from the usual 3d oxides with small spin-orbit coupling which can be described by isotropic Heisenberg interaction with small anisotropic corrections. In this way, it is revealed the unconventional nature of the magnetism in iridates using RXS technique in the static domain.

The influence of antiferromagnetic order on the lattice

Zone-centre optical phonons in iridates can be studied in a regular laboratory via Raman or pump-probe spectroscopy techniques. Through these methods it is possible to study how magnetism affects the phonon modes once the temperature is below T_N.

The use of Raman scattering as a probe of spin-orbit-lattice interaction in the iridates is very efficient since both magnons and phonons are detected with high resolution and signal intensity. The Raman-active phonons line shapes in $Sr_3Ir_2O_7$ and Sr_2IrO_4 are coupling indicators of spin and charge excitations. A set of lower-energy A_{1g} modes are seen at 5.3 THz in Sr_2IrO_4 and two peaks at 4.2 and 5.1 THz in the bilayer compound. H.Gretarson *et al.* performed a temperature dependence of the A_{1g} Raman mode intensity, finding that both modes exhibited an anomalous temperature dependence in $Sr_3Ir_2O_7$ for $T \leq 200K$ while in Sr_2IrO_4 showed soften anomalies below T_N. These magnetic-order-induced phonon frequency anomalies of similar magnitudes have been usually attributed to the dependence of the superexchange interaction on the atomic coordinates, which are dynamically modulated in a lattice vibration. In addition, Fano asymmetries for the A_{1g} mode in both compounds were found. These asymmetries can indicate a strong coupling to a continuum of excitations.

Since the magnetic-order-induced A_{1g} phonon line shape renormalization is of similar magnitude in both compounds (Figure 3.4), charge excitations can be ruled out as the origin of these anomalies. These considerations indicates that the spin-orbit coupling is not sufficiently strong to quench the orbital fluctuations in the paramagnetic state of Sr_2IrO_4 and $Sr_3Ir_2O_7$ [46].

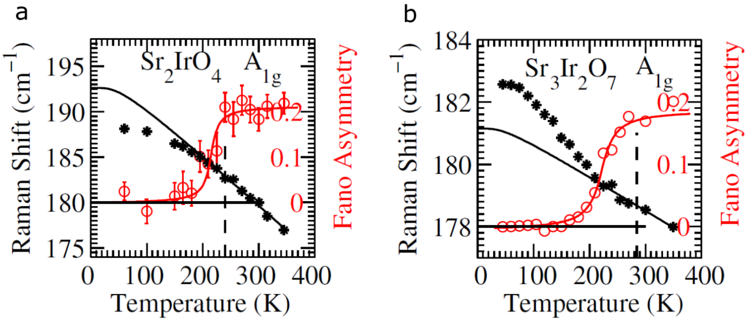

Figure 3.4: **Temperature evolution of the A_{1g} phonon mode using Raman scattering** of a) Sr_2IrO_4 and b) $Sr_3Ir_2O_7$. Both compounds show a frequency shift with temperature. The right axis indicates the Fano asymmetry parameter of the A_{1g} mode. Taken from [46].

L.L.Hu *et al.* obtained similar results using pump-probe technique in $Sr_3Ir_2O_7$. Two A_{1g} modes were observed, one phonon at a frequency of 4.42 THz and a discernable peak at 5.5 THz. Investigating the temperature dependence of these modes, it was found that the phonon amplitude exhibited an anomaly below T_N, where the amplitude at $T > T_N$ is constant and, from T_N to 180 K the amplitude suddenly sharply increases (Figure 3.5a). The phonon frequency also exhibits an anomaly below T_N with a similar temperature dependence to that observed on the phonon amplitude (Figure 3.5b). A comparable table of the transition temperature and phonon frequencies of both components is shown in Table 3.3.

	T_N	A_{1g} modes	B_{2g} mode
Sr_2IrO_4	240 K	$\sim$ 5.3 THz	11.4 THz
$Sr_3Ir_2O_7$	280 K	$\sim$ 4.2 and $\sim$ 5.1 THz	11.4 THz

Table 3.3: T_N and phonon frequency values of Sr_2IrO_4 and $Sr_3Ir_2O_7$.

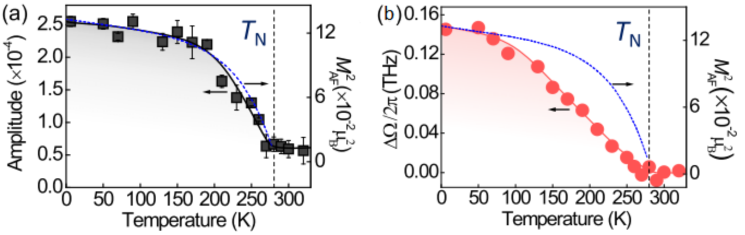

Figure 3.5: **Temperature dependence of the coherent A_{1g}phonon by pump-probe spectroscopy technique.** a) Amplitude. Blue dashed curve: M^2_{AF} adapted from [58] b) frequency deviation $\Delta\nu$ (red dots) assuming conventional anharmonic phonon decay. M^2_{AF} adapted from [58].The dashed vertical lines mark T_N. Taken from [45].

3.4.2 Dynamic magnetic properties

Although ultrafast manipulation of magnetism holds great promise for progress in the understanding of new quantum states and technical applications, the knowledge of how the magnetic correlations evolve on ultrafast timescales is limited for antiferromagnetic materials. The iridates have become the first materials to break this impasse. Recently, the first ever time-resolved RIXS (tr-RIXS) experiments have been performed first on Sr_2IrO_4 and on $Sr_3Ir_2O_7$, enabling the study of magnetic correlations on short lengthscales for the first time [59, 60].

In Sr_2IrO_4, the long range magnetic order shows that, in the non-equilibrium state, is strongly suppressed after 2 ps of the excitation, but hosts photocarriers that induced strong, non-thermal magnetic correlations. Figure 3.6b shows the 3D long-range magnetic order in Sr_2IrO_4 (blue trace) is suppressed very fast but restores on a fluence-dependent timescale of a $\tau_{mag} \approx 100$ ps. Looking at the RIXS difference spectra, Dean *et al.* saw that the magnon at $(\pi, 0)$ was identical before and after the pump, whereas the (π, π) showed appreciable changes. This indicates that the high-energy correlations at $(\pi, 0)$ are more robust than the lower-energy spin wave at (π, π) that arises from a smaller disturbance of the Néel order (Figure 3.6c). This could imply that the higher-energy magnons recover to their equilibrium configuration in much less than 2ps, which could be owing to the fact that a higher-energy excitation can decay into lower-energy multi-particle excitations in a greater number of different ways that can the lower-energy magnons.

In contrast, the 3D long-range magnetic order in $Sr_3Ir_2O_7$ (grey trace in Figure 3.6b) shows that immediately after the optical pump (t=0) magnetism is reduced by 50-75%. This occur faster than 0.15 ps. A significant fraction of the magnetic signal is recovered within the first picoseconds, but a slower process is superimposed preventing the full restoration of the original magnetic state. As a result, the reduced magnetic peak intensity stays roughly constant in the range between 5 and 500 ps without noticeable recovery. The different behaviour between both materials are likely to arise from their distinct magnetic interactions and resulting magnon dispersions. To confirm this statement, Mazzone *et al.* [60] studied the tr-RIXS energy-loss spectra of $Sr_3Ir_2O_7$ measured at (π, π) and (π,0), corresponding to the minimum and maximum of the gapped spin-wave dispersions. They found that at both reciprocal lattice positions, significant changes at $t > 0$ were recorded up to 5 ps, evidencing that the magnon and orbital excitations are altered upon photo-doping at both, (π, π) and (π, 0). Moreover, the similarity in the time evolution at the minimum and maximum of the dispersion relation (Figure 3.6d) shows the transient magnons in $Sr_3Ir_2O_7$ are trapped over an extended area in reciprocal space (Figure 3.6e), demonstrating an incoherent response of transient magnetism.

Even though these techniques show that direct measurements of the 2D magnetic correlations and are consequently crucial for an understanding of magnetic dynamics in strongly correlated materials, the response of other degrees of freedom on these experiments remains elusive. For example, it is still unknown if the optical quenching of the spin order requires a concomitant heating of the lattice, i.e. if the suppression of spin order is due to rapid, but trivial, heating, or if in contrast, the suppression is non-thermal, potentially enabling access to new transient states unreachable in thermodynamic equilibrium. Whether the process occurs thermally or non-thermally is critical as it dictates what mechanism stabilizes the photo-excited state, and ultimately determines our ability to control it. In the next chapters, we will study first, the electronic and structural properties of $Sr_3Ir_2O_7$ upon photo-excitation and, second, we will demonstrate that light can non-thermally melt long-range spin order in $Sr_3Ir_2O_7$, where at low fluences magnetic order recovers within 1 ps but at high fluences the system remains demagnetized where the generation of photo-induced spin defects enables a mechanism that could help expose new transient phases.

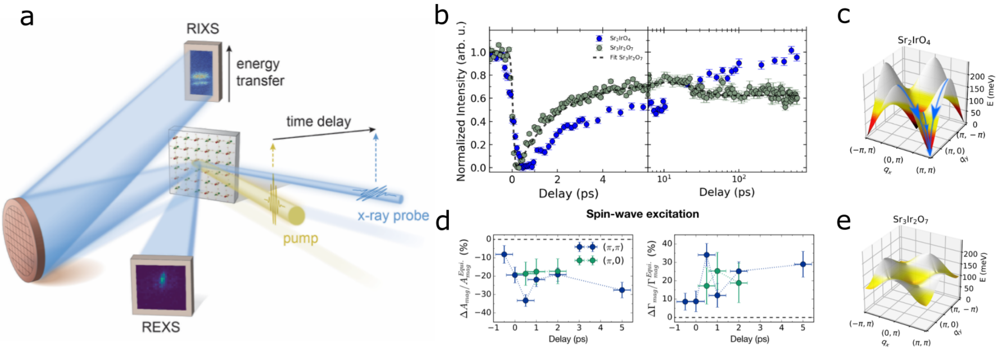

Figure 3.6: **tr-RIXS and tr-REXS measurements on iridates.** a) Scattering set-up, where the yellow is the optical laser pump (2 µm) and the blue pulses are the ultrashort X-ray pulses. Magnetic long-range order was measured via tr-REXS. After the sample position tr-RIXS was measured. b) Relative magnetic Bragg peak intensity as a function of time delay of $Sr_3Ir_2O_7$ (grey) and Sr_2IrO_4 (blue). Black dashed line is a fit of a model of the time evolution of the transient magnetic long-range order shown in [60]. c) Equilibrium state magnetic dispersions of Sr_2IrO_4. d) Time dependence of the relative magnon amplitude and full-width at half-maximum, respectively. e) Equilibrium state magnetic dispersions of $Sr_3Ir_2O_7$. Taken from [60].

Chapter 4

Ultrafast broadband detection of photo-induced electronic and structural changes in $Sr_3Ir_2O_7$

This chapter studies the electronic and structural properties of the bilayer iridate compound, $Sr_3Ir_2O_7$. *Section 4.1 shows how photo-excitation changes the reflectivity at a wide range of energies and shows how to characterize the optical parameters by starting from a published optical conductivity spectra at different temperature. Section 4.2 shows the experimental changes in the reflectivity upon photo-excitation at different temperatures and time delays and shows the difficulties to define a model that captures the electronic dynamics. Section 4.3 introduces the structural properties by looking at the coherent phonon spectra at different excitation fluences at 77 K. Section 4.4 summarizes the main conclusions of this chapter.*

4.1 Introduction

In the previous chapter we discussed how the magnetic state of $Sr_3Ir_2O_7$ has been tracked with X-ray techniques. However, the response of the other degrees of freedom has yet to be fully explored in detail. In this chapter we look at how both the photo-excited electrons and coherent phonons modify the electronic properties of a semiconducting iridium-based oxide and how to track those changes using ultrafast broadband spectroscopy. Before discussing our results, we first consider what happens when we photo-excite conventional semiconductors and how to measure these changes. The effect of an intense pulse of light on the reflectivity of the materials is non-trivial, as the pulse can trigger many different processes that result in a prompt change in the reflectivity of the material.

In a direct band gap semiconductor, the absorption can take place only at frequencies for which the photon energy $h\nu > E_g$, where E_g is the energy gap. This adds to the concentration of mobile charge carriers and increases the conductivity of the material. Following photo-generation, these charges might recombine. However, the radiative electron-hole recombination is unlikely in an indirect-gap semiconductor. This is because transitions from near the bottom of the conduction band to near the top of the valence band require an exchange of momentum that cannot be accommodated by the emitted photon. However, momentum may be conserved by the participation of phonons. Although photon absorption also requires energy and momentum conservation in an indirect-gap semiconductor, this is readily achieved by means of a two-step process. The electron is first excited to a high energy level within the conduction band by a vertical transition. Subsequently, it quickly relaxes to the bottom of the conduction band by thermalization in which its momentum is transferred to phonons.

In this picture the band structure remains fixed and the dynamics are dictated by the change in the charge distribution. In correlated materials the effects can be more complex as the distribution of charges can also prompt changes in the electronic structure or drive phase transitions. Furthermore, it can also generate coherent phonons, which in turn modulates the band structure. Experimentally, these changes in the properties of the materials can be measured by tracking the reflectivity of the sample at the relevant energies.

The reflectivity can be related to the electronic structure through the dielectric function as:

$$R = \left| \frac{\sqrt{\hat{\varepsilon}(\omega)} - 1}{\sqrt{\hat{\varepsilon}(\omega)} + 1} \right|^2 \tag{4.1}$$

The dielectric function $\hat{\varepsilon}$ is a complex function that depends on the frequency ω of the driving electric field and measures the electric polarizability of an insulator or dielectric material. The real (ε_1) part captures the low frequency response of the free electrons, while the imaginary (ε_2) part of the dielectric function models the optical transitions between different bands. Often, these transitions are approximated as 'Lorentzian'. The dielectric function is defined as

$$\hat{\varepsilon} = \varepsilon_1 + i\varepsilon_2 = \frac{A^2(\omega_0^2 - \omega^2)}{(\omega_0^2 - \omega^2)^2 + \omega^2\gamma^2} + i\frac{A^2\omega\gamma}{(\omega_0^2 - \omega^2)^2 + \omega^2\gamma^2} \tag{4.2}$$

From ε_2 we can obtain the optical conductivity that quantifies how well a material conducts electricity at different frequencies and allows us to model the optical resonances and therefore infer information about the transitions that can be (photo-) induced in our materials. Normally, the full dielectric function is given as a linear summation of multiple Lorentzians to account for the fact that materials have more than one resonance.

$$\sigma(\omega) = \varepsilon_2(\omega)\omega = \sum_i \frac{A^2\gamma}{(\omega_{0i}^2 - \omega^2)^2 + \omega^2\gamma^2}\omega^2 \tag{4.3}$$

Therefore, studying the changes in the dielectric constant through changes in the reflectivity of the sample provides an experimental way to understand how photo-excitation modifies the properties and ultimately the function of correlated materials. Next, we evaluate the optical parameters (A, ω_0 and γ) in the prototypical Mott insulator $Sr_3Ir_2O_7$.

4.1.1 Optical parameters of $Sr_3Ir_2O_7$ in the visible regime

In order to understand what reflectivity dynamics mean, it is important to understand what the visible region of the reflectivity spectra actually measures. For this, we use the optical conductivity spectra of $Sr_3Ir_2O_7$ published by Park *et al.* at 400 K [61], shown in Figure 4.1 for a broad range of energies from 0 to 5 eV. The changes of the optical conductivity with energy are highly structured, in particular we can identify 9 different shoulders indicated with arrows in the figure. To model them, we use equation 4.3. The results of the fit are shown as a solid blue line in the figure. The same fit was performed at 200 K and 10 K. From this model, we can extract the different values of the central frequency ω_0, amplitude A and damping term γ parameters, which are shown in Table 4.1. The contribution of each feature is shown in Figures 4.2a and b for the two extreme temperatures, 400 and 10 K, respectively. We observe that the spectrum is dominated primarily by five components: two are centred at values lower than 1 eV, specifically at 0.25 and 0.86 eV. These are consistent with the α and β direct transition between energy bands shown in Section 3.3 from the previous chapter. The other three main features are centred at 2.4, 3.3 and 5 eV and are related to charge transfer excitations between the Oxygen and Iridium ions [34]. A zoom of the visible region is shown in Figures 4.2c and d which is dominated by the resonances at 0.86, 2.4 and 3.3 eV. Interestingly, we observe that the central frequencies do not significantly change with temperature, instead the main differences between the three temperatures analysed are associated to the amplitude and damping terms.

400 K			200 K			10 K		
ω_0	A	γ	ω_0	A	γ	ω_0	A	γ
0.25	15.5	0.48	0.35	13	0.35	0.38	12.7	0.3
0.86	21.3	1	0.86	20	0.85	0.86	22.7	0.8
1.3	5	0.8	1.3	8	0.7	1.3	10	0.7
1.75	24.8	4.6	1.6	30	5	1.75	20	14.5
2.4	14.5	0.8	2.4	13	0.5	2.4	16	0.7
2.8	8	1	2.8	14	0.8	2.8	13	1.25
3.3	49.5	2.16	3.3	45.5	1.8	3.3	51	1.97
4.13	8	1.1	4.13	14.5	1.15	4.13	12	1.1
5	53.5	2.1	5.1	49	1.8	5.15	52	1.75

Table 4.1: Central frequency (ω_0), amplitude (A) and damping term (γ) coefficients of $Sr_3Ir_2O_7$ at 400 K, 200 K, and 10 K.

Having identified all the main features, we next reconstruct the real (ε_1) and imaginary (ε_2) parts of the dielectric function as well as the reflectivity by using the equations 4.2 and 4.1, respectively. Figure 4.3a shows that ε_1 and ε_2 have a similar magnitude, which has important consequences for the modelling of

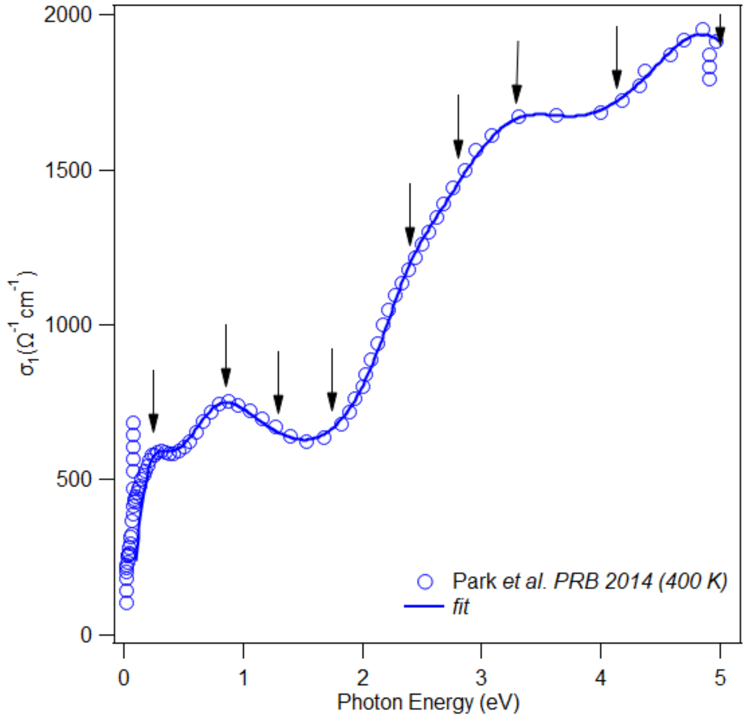

Figure 4.1: **Optical conductivity of $Sr_3Ir_2O_7$ at 400 K.** The circle data is taken from [61] and the solid line is the fit using the parameters from Table 4.1. The arrows represent the different oscillators in the spectrum.

transient conductivity changes as discussed below. Focusing on the reflectivity at different temperature, we observe that the reflectivity decreases until ~1.8 eV and it is relatively flat at higher energies.

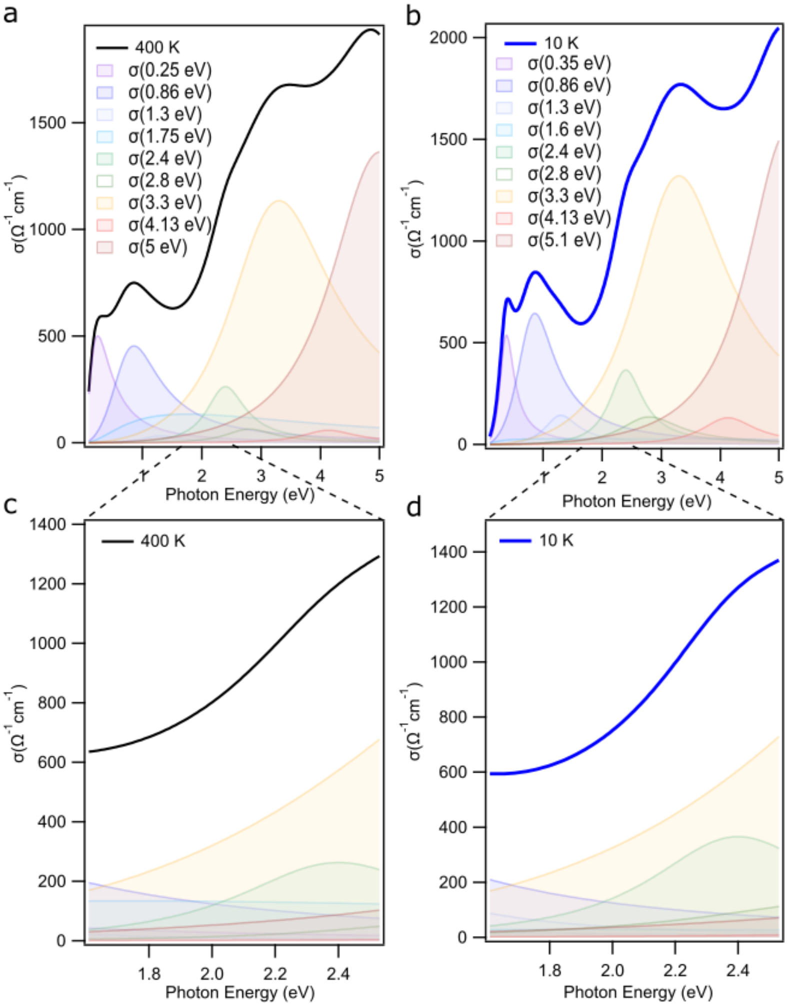

Figure 4.2: **Optical contribution of each Drude-Lorentz term from 0 to 5 eV** at a) 400 K and b) 10 K. The main contributions at both temperatures are given by the oscillators at 0.25, 0.86, 2.4, 3.3 and 5 eV. c, d) Zoom of the optical conductivity in the visible range at 400 K and 10 K, respectively. The main contributions in this range are at 0.86, 2.4 and 3.3 eV.

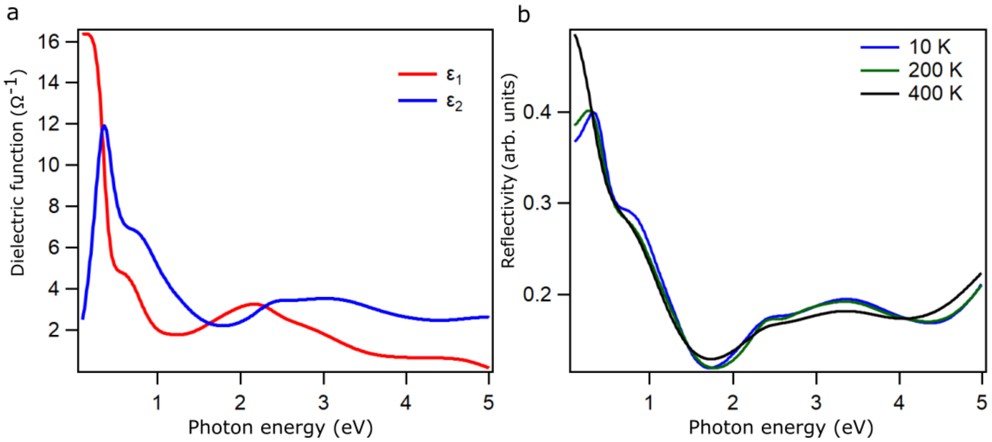

Figure 4.3: **Dielectric function and Reflectivity of $Sr_3Ir_2O_7$ at 10, 200 and 400 K.**

4.1.2 Differential reflectivity as a function of temperature

Next we evaluate in more detail how the reflectivity changes as a function of temperature. In particular, we assess the difference between above and below the transition temperature, $T_N \sim 280$ K. To evaluate these differences, we represent the data as normalized changes in reflectivity as

$$\frac{\Delta R}{R_{off}} = \frac{R_{highT} - R_{lowT}}{R_{lowT}} = \frac{\Delta R_{highT-lowT}}{R_{lowT}}$$

Such representation allows us to compare the data more directly to the experimental change in the reflectivity measured in our laboratory. Figure 4.4a shows the change in reflectivity at 400, 200 and 10 K. We focus in the visible region shown in Figure 4.4b. $\Delta R_{400-10}/R_{10}$ and $\Delta R_{400-200}/R_{200}$ show the same behaviour albeit a small red shift with increasing temperature. Both signals are characterized by a positive change at low energies and a negative change above to ~ 2.1 eV and ~ 2.3 eV, respectively. In contrast, $\Delta R_{200-10}/R_{200}$ has a different behaviour, primarily exhibiting a negative change throughout the analysed visible region. Such difference could result from the fact that ΔR_{200-10} corresponds to the reflectivity change between the same magnetic state of the sample. In contrast, $\Delta R_{400-10}/R_{10}$ and $\Delta R_{400-200}/R_{200}$ represents the change between two different magnetic states (i.e., above and below T_N). In the next section, we compare these data with the transient experimental results obtained after photo-excitation of $Sr_3Ir_2O_7$.

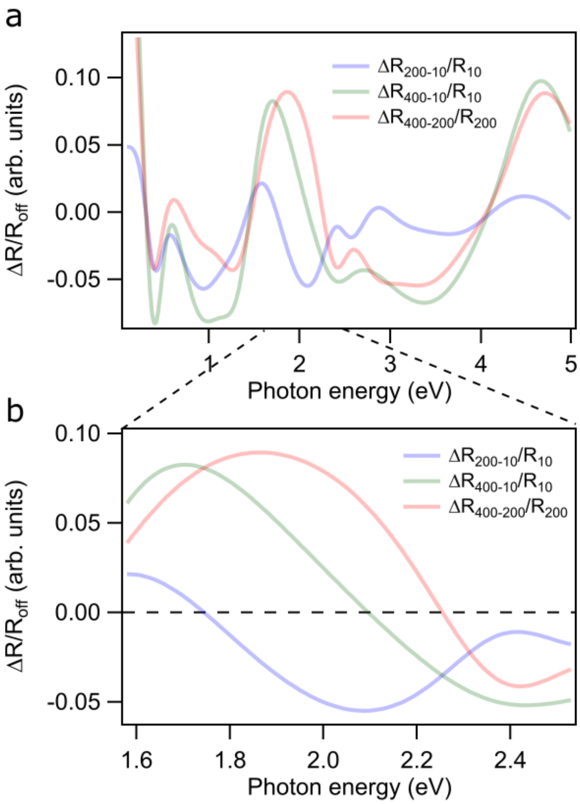

Figure 4.4: **Change of the reflectivity of $Sr_3Ir_2O_7$ as a function of temperature** a) from 0 to 5 eV. b) Zoom of the change of the reflectivity in the visible range. The dashed line represents the 0 level that indicates a change in the sign of the signal.

4.2 Experimental photo-induced reflectivity changes in $Sr_3Ir_2O_7$

Broadband pump-probe measurements of $Sr_3Ir_2O_7$ has been performed in our laboratory at different temperatures and fluence. The experimental changes on the reflectivity have been modelled based on the optical parameters studied above.

4.2.1 Ultrafast transient reflectivity setup

The transient reflectivity measurements presented herein are performed using the laser system described in Section 2.2. The pump is at 800 nm (described in Section 2.2.2) with an energy of 1 mJ at 5 kHz repetition rate. The broadband visible probe light (further description in Section 2.2.3) was generated by focusing a small fraction of the 800 nm beam onto a sapphire crystal. The pump energy was adjusted using a half wave plate on a motorized stage capable of rotating the polarization of the beam relative to a Brewster polarizer. Both beams were focused on the sample and to ensure probing of a homogeneously pumped region, the probe size ($\sim 4 \cdot 10^{-5}$ cm^2) was made smaller than the pump size ($\sim 2 \cdot 10^{-4}$ cm^2). The sample is a $Sr_3Ir_2O_7$ single crystal synthesized using the self-flux method as described in Ref. [62] and references therein. It is a cleaved sample to obtain a clean surface for all measurements. The changes in the reflectivity of this sample were detected using the *Detector 1* (Section 2.2.4), which is the commercial *Andor iXon sCMOS* camera. The cryogenic measurements were performed using liquid nitrogen cryostat (*Oxford Instrument, Optistat DN-V*) capable of maintaining a pressure of 10^{-6} mbar. The measurement has been taken at 77 K and 295 K at different fluences up to 8 mJcm^{-2} and at different time delays ranging from -0.5 to 5.5 ps with steps of 0.015 ps. Such fine scans are required to identify and analysed any coherent phenomena in our data.

4.2.2 Ultrafast transient reflectivity spectra

Figure 4.5 shows a typical broadband transient reflectivity spectra taken at 77 K and 295 K following photo-excitation with 800 nm (1.5 eV) laser light at fluence values of F=1.5, 3, 5 and 8 mJcm^{-2}. The spectral changes are qualitatively similar in all cases. For a given fluence, both temperatures show a suppressed reflectivity at short wavelengths and a signal enhancement above ~600 nm (see lineouts in top Figure 4.5) consistent with a shift in the O2p-Ir5d charge transfer resonance [34]. Moreover they both exhibit fast dynamics within the first picosecond, followed by a much slower plateau. The signal is also modulated by an oscillating component due to coherent phonons as discussed further below.

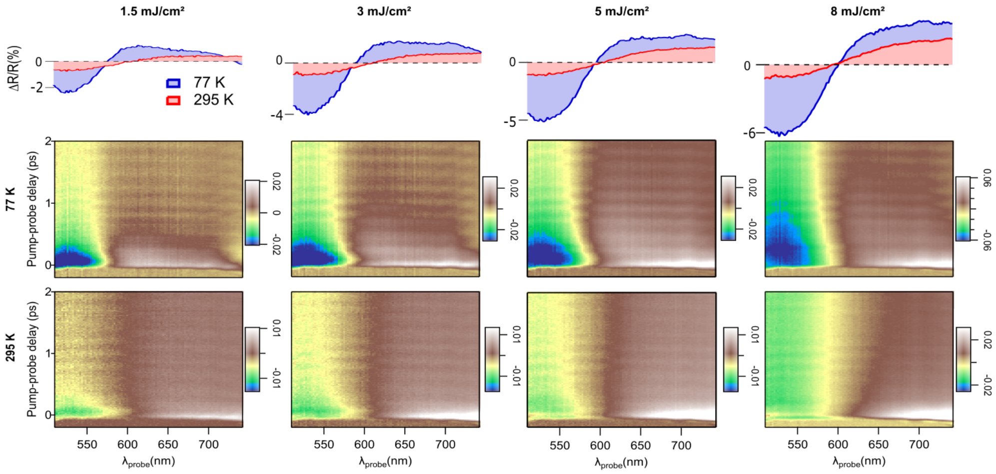

Figure 4.5: **Transient reflectivity change in $Sr_3Ir_2O_7$ upon 800 nm excitation at 77 K and 295 K.** Measurements at F= 1.5mJcm^{-2}, 3 mJcm^{-2}, 5 mJcm^{-2} and 8 mJcm^{-2}.

To facilitate comparison of the datasets, Figure 4.6 shows the lineouts at the two temperatures and at different fluences measured at 5 ps. Notably, this data is qualitatively the same as shown in Figure 4.4 for $\Delta R_{400-10}/R_{10}$ and $\Delta R_{400-200}/R_{200}$. We find that the amplitude of the negative signal increases as the temperature decreases, especially at high fluence values, while the changes of the positive signal are less abrupt. In addition, we observed that the crossing point (energy) between the positive and negative signal red shifts with increasing fluence when the sample is in the antiferromagnetic state at 77 K. In contrast, this crossing point keeps constant in the paramagnetic state at 295 K.

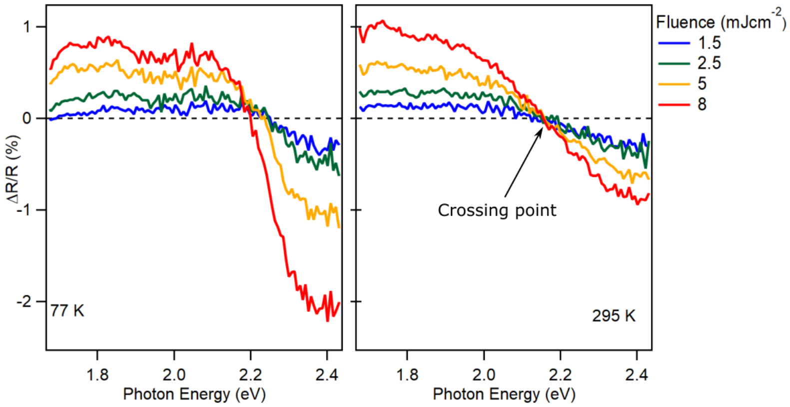

Figure 4.6: **Experimental reflectivity change of $Sr_3Ir_2O_7$ at 77 and 295 K at 5 ps.**

To understand the meaning of the spectra, we model them using the equations presented in previous sections. For small changes, we can express changes in reflectivity as a Taylor expansion. For changes in the resonant frequency, the reflectivity can be expressed as

$$\frac{\Delta R}{R} = \frac{1}{R}\left(\frac{\partial R}{\partial \varepsilon_1}\frac{\partial \varepsilon_1}{\partial \omega_0} + \frac{\partial R}{\partial \varepsilon_2}\frac{\partial \varepsilon_2}{\partial \omega_0}\right) d\omega_0$$

$$= \frac{1}{R}\left(\frac{\partial R}{\partial \varepsilon_1}\left(\frac{4A\gamma^2\omega_0\omega^2}{\left(\left(\omega_0^2-\omega^2\right)^2+\gamma^2\omega^2\right)^2} - \frac{2A\omega_0}{\left(\omega_0^2-\omega^2\right)^2+\gamma^2\omega^2}\right)\right.$$

$$\left. + \frac{\partial R}{\partial \varepsilon_2}\left(\frac{4A\gamma\omega\omega_0\left(\omega_0^2-\omega^2\right)}{\left(\left(\omega_0^2-\omega^2\right)^2+\gamma^2\omega^2\right)^2}\right)\right) d\omega_0$$

$$= \frac{1}{R}\left(\frac{\partial R}{\partial \varepsilon_1}\left(\frac{2A\omega_0\left(\gamma^2\omega^2-\left(\omega_0^2-\omega^2\right)^2\right)}{\left(\left(\omega_0^2-\omega^2\right)^2+\gamma^2\omega^2\right)^2}\right) + \frac{\partial R}{\partial \varepsilon_2}\left(\frac{4A\gamma\omega\omega_0\left(\omega_0^2-\omega^2\right)}{\left(\left(\omega_0^2-\omega^2\right)^2+\gamma^2\omega^2\right)^2}\right)\right) d\omega_0$$

$$= \left(\left(\frac{\left(\gamma^2\omega^2-\left(\omega_0^2-\omega^2\right)^2\right)}{\left(\left(\omega_0^2-\omega^2\right)^2+\gamma^2\omega^2\right)^2}\right) + \left(\frac{b\omega\left(\omega_0^2-\omega^2\right)}{\left(\left(\omega_0^2-\omega^2\right)^2+\gamma^2\omega^2\right)^2}\right)\right)\Delta\omega_0$$

Where $\Delta\omega_0 = \frac{1}{R}\frac{\partial R}{\partial \varepsilon_1}2A\omega_0 d\omega_0$; $b\Delta\omega_0 = \frac{1}{R}\frac{\partial R}{\partial \varepsilon_2}4A\gamma\omega_0 d\omega_0$ with *b* being a constant factor that connects the amplitudes from the real and imaginary terms.

A change in reflectivity for a change in the amplitude is expressed as

$$\frac{\Delta R}{R} = \left(\left(\frac{(\omega_0^2 - \omega^2)}{(\omega_0^2 - \omega^2)^2 + \gamma^2\omega^2}\right) + \left(\frac{b\gamma^2\omega^2}{(\omega_0^2 - \omega^2)^2 + \gamma^2\omega^2}\right)\right)\Delta A$$

Where $\Delta A = \frac{1}{R}\frac{\partial R}{\partial \varepsilon_1}AdA$; $b\Delta A = \frac{1}{R}\frac{\partial R}{\partial \varepsilon_2}AdA$

A change in reflectivity for a change in the damping term is expressed as

$$\frac{\Delta R}{R} = \left(\left(\frac{2\gamma\left(\omega_0^2 - \omega^2\right)}{\left(\left(\omega_0^2 - \omega^2\right) + \gamma^2\omega^2\right)^2 + 4\gamma\omega^2\left(\omega_0^2 - \omega^2\right)^2}\right)\right.$$
$$\left. + \left(\frac{b\left(\left(\omega_0^2 - \omega^2\right)^2 + \gamma^2\omega^2\right)}{\left(\left(\omega_0^2 - \omega^2\right) + \gamma^2\omega^2\right)^2 + 4\gamma\omega^2\left(\omega_0^2 - \omega^2\right)^2}\right)\right)\Delta\gamma$$

Where $\Delta\gamma = \frac{1}{R}\frac{\partial R}{\partial \varepsilon_1}A\omega^2 d\gamma$; $b\Delta\gamma = \frac{1}{R}\frac{\partial R}{\partial \varepsilon_2}A\omega^2 d\gamma$

In principle, all three components should be fitted to the data. However, as shown in Figure 4.7 the similarity between these shapes, makes fitting them difficult. Therefore, in the following, we assume that all changes are due to changes in ω_0 because this term has the biggest effect on the signal, and parameter has been shown to be important for similar transitions in the cuprates [34].

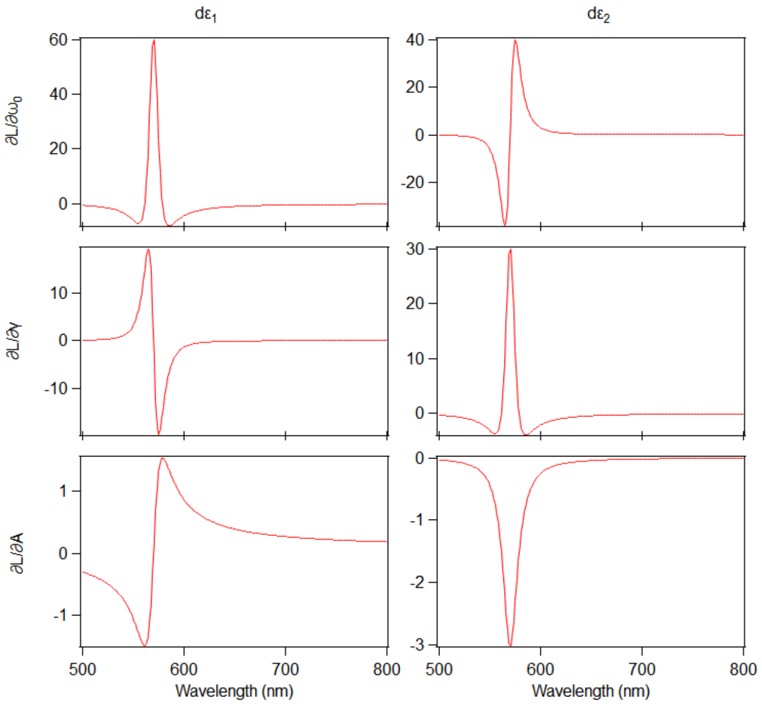

Figure 4.7: **Change of the Lorentzian term as a function of the parameters.** The parameter values to calculate these simulations have been A=1, ω_0=2.18 (λ_0 = 570 nm) and, γ = 0.1.

We proceed to study the changes on the reflectivity by fitting our experimental data with the $\delta R = \frac{\partial R}{\partial \varepsilon}\frac{\partial \varepsilon}{\partial \omega_0}d\omega_0$ term at different fluence, time delays and temperatures. First, the fitting functions were calculated at one temperature and time by using the equation 4.2.2 where no restrictions were imposed to calculate the parameters for each fluence. Subsequently, we calculated the mean value of the obtained b, ω_0 and γ terms, as we do not expect them to change with fluence. Then, a new fitting procedure was done by fixing these parameters to the calculated mean value and only allowing the amplitude A to change. Figure 4.8a shows the curve fitting at 77 K at 5 ps. The fitting matches the data very well but at high excitation fluence they start to deviate, where the raw data is red shifted relative to the model. Figure 4.8b shows the data immediately after photo-excitation at 0.5 ps. In this case, despite the fit matching well the data, both at high and low fluence show some differences at $\Delta R/R=0$. In addition, a second resonance at $\approx$ 1.7 eV (Table 4.1) start to become more important. Figures 4.8c and d show the fit on the reflectivity data at 295 K at 5 and 0.5 ps, respectively. At both times the fit works properly since there is no red shifts with fluence and only the resonance at around 2.4 eV is dominant. Figure 4.9 shows the comparison of this resonance with temperature between the experimental frequency obtained through the fitting curves and the ones obtained by evaluating the optical conductivity measured by Park *et al.* [61] and shown in Table 4.1. Both data show a similar frequency at $\approx$ 2.3-2.4 eV at different temperatures, showing the reliability on both methods.

In summary, we find that optical excitation induces changes in reflectivity that are consistent with a change in the Oxygen-Iridium charge transfer resonance. Such changes are very similar to the cuprates, where photo-excitation was also shown to shift the Cupper-Oxygen charge transfer resonance [34]. Our model works well for all times and fluences at high temperature, but there are significant deviations as a function of fluence or time at 77 K. We speculate that such deviations could originate from changes in the magnetic state of the sample as we discuss in detail in Chapter 5. Next, we further characterize how the coherent phonons in the signal modulate the charge transfer resonance.

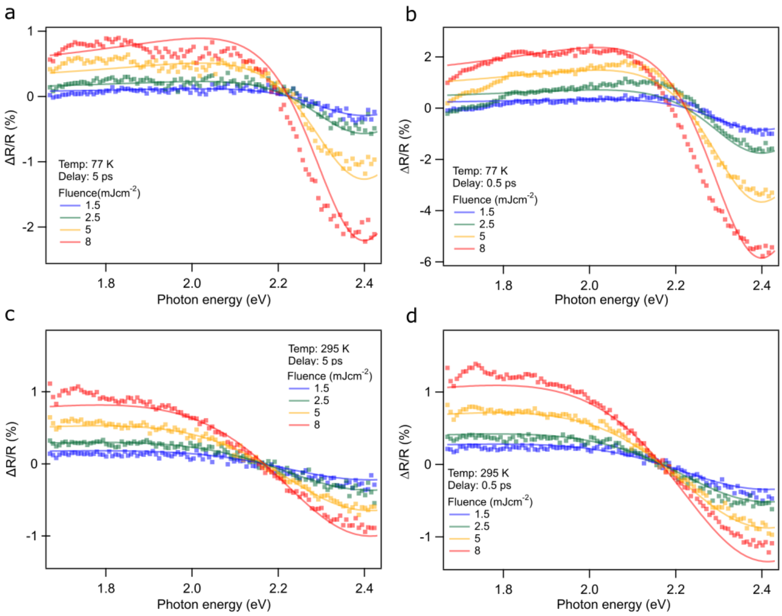

Figure 4.8: **Lorentzian fit to the experimental reflectivity change at 77 K and 295 K.**

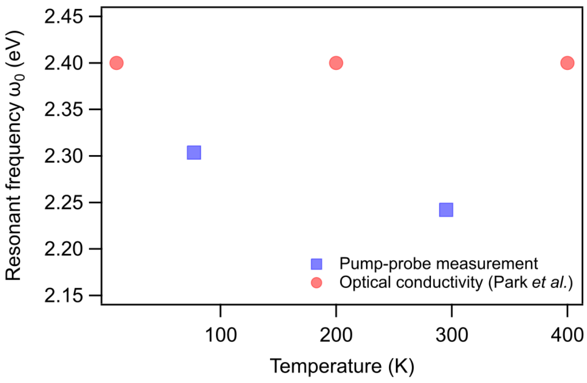

Figure 4.9: **Comparison between the experimental and theoretical frequency with temperature.**

4.3 Coherent phonon spectra

Having discussed the different spectral shape under several conditions, next we look to the time evolution of the transient reflectivity. As observed in Figure 4.5, the signal is modulated by coherent phonon oscillations. To isolate these oscillations, first we differentiate the signal in order to remove the incoherent exponential decay component (Figure 4.10a). Subsequently, a fast Four Transform (FFT) of the resulting differential map yielded a 2D plot of frequency vs probe wavelength. To avoid any coherent artefact at t ~ 0 ps, the dataset was analysed only between 0.3 - 5.5 ps. Inspection of Figure 4.10b reveals two clear features at around 4.42 and 5.46 THz that correspond to the low and high energy A_{1g} modes, respectively. Interestingly, the maximum intensity of each mode is strongly wavelength dependent, while the 4.42 THz mode has a maximum in the region of 650-750 nm (1.65-1.9 eV), the 5.46 THz mode has a maximum at ~550 nm (2.25 eV).

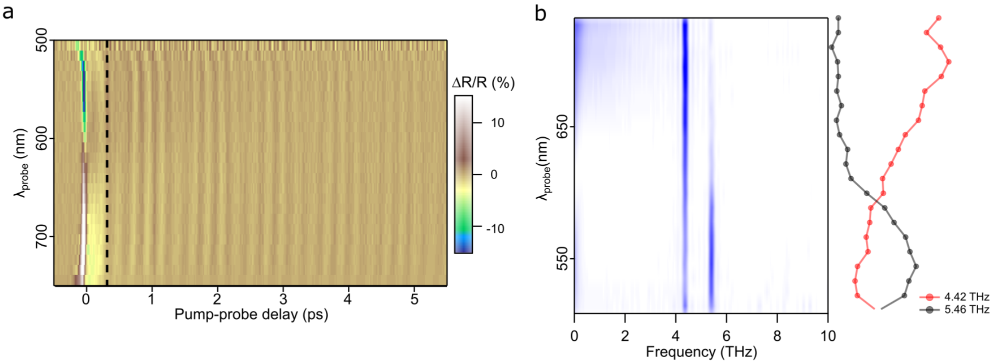

Figure 4.10: **Differentiated transient reflectivity change and Fourier Transform of $Sr_3Ir_2O_7$ at 77 K.** a) Differentiated transient reflectivity change to remove the incoherent exponential decay component. The dashed line indicates the starter time at which the FFT is calculated to avoid any coherent artefact at t ~ 0 ps. b) Fourier transform of the oscillations form the transient reflectivity data. The lineout show the FFT visible spectra of the 4.42 and 5.46 THz phonon modes.

We next perform the same analysis at 77 K and 295 K as a function of excitation fluence. Figure 4.11a shows the intensity of the 5.46 THz as a function of wavelength at 77 K. The spectrum at each fluence has a Gaussian shape centred at ∼ 550 nm and the intensity of the mode increases linearly with fluence. Figure 4.11b presents the same mode at 295 K; the spectra still remains a Gaussian shape centred ∼550 nm for all fluences, however the amplitude is significantly smaller compared to the 77 K data. Looking at the 4.42 THz phonon mode, we observe that at 77 K the spectrum has a broader Gaussian shape and that the central frequency red shifts with increasing fluence (Figure 4.11c). In contrast, the same mode at 295 K shows no significant spectral structure nor a dependence on the excitation fluence (Figure 4.11d).

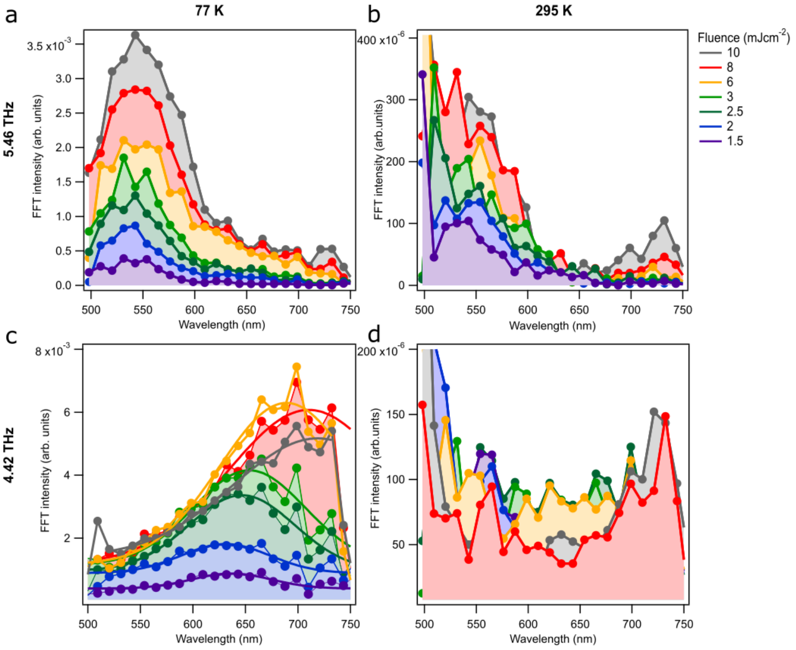

Figure 4.11: **Phonon spectra at 77 K and 295 K at different fluence values.** Intensity of the 5.46 THz mode as a function of wavelength at a) 77 K and b) 295 K. c) Intensity of the 4.42 THz mode as a function of wavelength at 77 K and d) 295 K. Solid lines indicate the Gaussian function fit to the spectra at different fluence values.

To further characterize the behaviour of the two different modes as a function of fluence and temperature in a broadband range of wavelengths we fit the spectrum with a Gaussian function and obtained detailed values for the amplitude, width and central wavelength to which the modes couple. Figure 4.12a shows how the amplitude of the 4.42 THz mode increases rapidly with fluence until it saturates at ∼5 mJ/cm^2. In contrast, the amplitude of the 5.46 THz mode increases more linearly with fluence. Figure 4.12b presents the change of the width as a function fluence. In the low energy mode, the width increases linearly with fluence, whereas in the high energy mode, the width keeps mainly constant with only a small increased at higher fluences. Most remarkably, this analysis shows that the central wavelength to which the 4.42 THz couples more strongly, shifts by ∼ 100 nm within 1 to 10 mJ/cm^2 while the central wavelength of the 5.46 THz mode shows no significant change in the same fluence region (Figure 4.12c). Another way to visualize the results is by representing the area of the Gaussian (*Amplitude x width*). This is shown in Figure 4.12d where we can see that the area for the high energy mode saturates at high fluence while the 5.46 THz mode area increases linearly with fluence. Overall, these results show the phonon modes exhibit a strong fluence dependence with the 4.5 THz mode at 77 K being the most fluence sensitive.

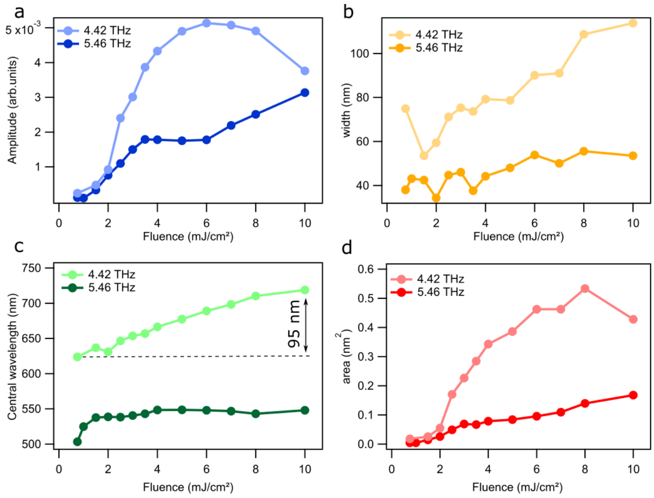

Figure 4.12: **Gaussian coefficients from the phonon spectra fit as a function of fluence at 77 K.** a) Amplitude, b) width, c) central wavelength and d) area coefficients of both 4.42 and 5.46 THz phonon modes.

An alternative way to verify such strong fluence dependence on the 4.42 THz mode at 77 K is by directly fitting the differentiated transient data (Figure 4.10b) at different fluence focusing on the 650-700 nm region where this mode shows its maximum intensity and the 5.46 THz mode contribute less (Figure 4.11). The differentiated transient data was fit with the equation:

$$f(t) = A_1 \cos\left(\frac{2\pi f_1}{T_1} + \varphi_1\right) e^{-t/\tau_1} + A_2 \cos\left(\frac{2\pi f_2}{T_2} + \varphi_2\right) e^{-t/\tau_2}$$

where A_1, f_1, T_1, φ_1 and τ_1 correspond to the amplitude, frequency, period, phase and constant time of the low energy mode respectively. Analogously, the second term of the equation correspond to the high energy mode.

Figure 4.13a shows the perfect match between the raw data (circles) and the fit (solid lines) at different fluence values at 77 K. Figure 4.13b shows the amplitude parameter from the fit. It shows a similar behaviour on both modes with fluence as observed in Figure 4.12a: the 4.4 THz mode start to increase with fluence until it saturates at high pump fluence while the amplitude of the 5.46 THz mode increases linearly with fluence.

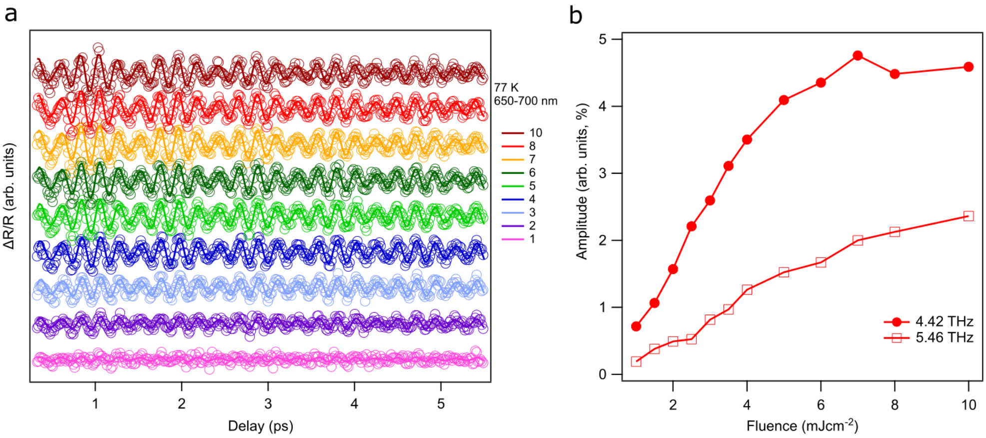

Figure 4.13: **Alternative method to study the fluence dependence on the phonon modes.** a) Fit of the differentiated transient data at 77 K and different fluence at 650-700 nm. b) Amplitude parameter of 4.38 THz and 5.46 THz mode as a function of fluence obtained through the fitting procedure.

These results emphasise that the transient reflectivity in the visible range is sensitive to the two main A_{1g}. Consequently, our broadband reflectivity provides a tool to monitor changes in the structure of the material. Notably, we find that the amplitude and the coupling of these two modes to these spectral region changes depends strongly on the sample temperature. Moreover, at 77 K where the sample is magnetically ordered, both modes exhibit a strong dependence on the photo-excitation fluence. Such behaviour could originate from changes in the magnetic order induced by the perturbation pulse and the coupling between the electronic, spin and the lattice degree of freedom.

4.4 Conclusions

In this chapter we have looked at how the dielectric function changes as a function of the photo-excitation. Our five main observations can be summarized as:

- The static spectrum in the visible range of $Sr_3Ir_2O_7$ is highly sensitive to temperature, with significant differences above and below the Néel temperature, T_N.
- The wavelength dependence of the reflectivity is also sensitive to the photo-excitation fluence as well as the time-delay .
- Our model to reproduce the reflectivity works well for all times and fluences at high temperature. The deviations as a function of fluence or time at 77 K could originate from changes in the magnetic state of the sample induced by the perturbation laser pulse.
- The transient reflectivity signal is modulated by coherent oscillations corresponding to the A_{1g} phonon modes.
- The amplitude of the modes as well as the wavelengths to which the couple in the visible range are sensitive to both temperature and fluence.

Previous results are shown that these two modes are sensitive to the magnetic state of the sample. In particular, a strong pseudospin-lattice coupling [45] and a pronounced Fano asymmetry shape that vanishes for $T < T_N$ [46] has been identified in $Sr_3Ir_2O_7$. The high selectivity of our pump-probe data to these two modes as well as the high sensitivity of the transient signal to temperature and excitation fluence suggest the visible range could be highly sensitivity to the magnetic order and thus provide a platform to understand the physics of photo-excited of $Sr_3Ir_2O_7$. In the next chapter we address this issue and identify a clear marker of the spin order in the system which allows us to track the antiferromagnetic to paramagnetic phase transition.

Chapter 5

Tracking spin and charge ordering in $Sr_3Ir_2O_7$

This chapter introduces the transient optical response of $Sr_3Ir_2O_7$ *in four dimensions with the aim of studying the response of the spin system in the demagnetization process. Section 5.1 shows the importance of tracking the magnetic order in* $Sr_3Ir_2O_7$. *Section 5.2 describes the experimental details used in our measurement. The experimental results are presented in Section 5.3 while their the interpretation are discussed in Section 5.4. Finally, the chapter ends with conclusions in Section 5.5.*

5.1 Introduction

As discussed in Chapters 3 and 4, $Sr_3Ir_2O_7$ is a spin-orbit Mott insulator that exhibits a phase transition from paramagnetic to antiferromagnetic at $T_N \approx 280$ K. There is large scientific interest in learning to control antiferromagnetic states, this is because antiferromagnetic order often breaks down into technologically-relevant phases such as high-temperature superconductivity by chemical doping [41] or by optical excitation (photo-doping) which has been proposed to act similarly to chemical doping [26, 63]. In $Sr_3Ir_2O_7$ it has been shown that light can quenched the antiferromagnetic order [60] therefore opening a route to control the magnetic properties of this material on demand.

In the previous chapter, we discussed how photo-excitation causes shifts in the electronic and structural degrees of freedom and how this manifests in the optical conductivity. In particular, we observed differences in the spectral response and the phonon modes when photo-exciting above and below Néel temperature. However, we did not extract any quantitative magnetic information from our data which allows us to evaluate whether the spin order changes upon photo-excitation or if the lattice plays a significant role. To date, magnetic dynamics have been primarily accessed through X-ray scattering experiments. Nevertheless, a complete understanding of the demagnetization process is still missing, for example, it is unknown if the optical quenching of the spin order requires a concomitant heating of the lattice or if in contrast, the suppression is non-thermal, potentially enabling access to a new transient states unreachable in thermodynamic equilibrium. Tracking the demagnetization is challenging for the iridates as, while many optical probes of ferromagnetism exist, probing antiferromagnetic states is more difficult due to the lack of net magnetic moment. In this chapter, we directly address this issue by identifying and tracking a marker for the magnetic order in $Sr_3Ir_2O_7$.

5.2 Specific technical details

In order to understand the spin dynamics we record the transient optical response of $Sr_3Ir_2O_7$ in four dimensions namely, as a function of time, wavelength, excitation fluence and temperature. This multidimensional approach allows us to separate out magnetic dynamics from structural and electronic processes enabling us to map out quantitative magnetic changes in unprecedented detail, while also assessing the lattice temperature from the viewpoint of the phonon frequencies. To achieve this:

- The temperature was modulated randomly from 77 K to 360 K, obtaining a broad temperature spectrum where the edges of the range are far from T_N. Thus, we are sure to measure the antiferromagnetic or paramagnetic orders. The fact that the temperature was adjusted randomly assures us that the changes in the sample as a function of temperature are real, avoiding possible effects produced by heating or cooling the sample in a linear way.

- Data collection was restricted to time delays between -0.4 and 1 ps in steps of 0.1 ps. If all temperature datasets had been collected with high time-resolution (≈0.01 ps), the entire measurement would have taken days to complete, favouring possible external factors to affect the consistency of the results. For example, (i) ice formation can be generated, (ii) after adding liquid Nitrogen to the cryostat to maintain the low temperature, possible vibrations in the cryostat can affect the position of the sample as well as the direction of the light reflected, varying the coupling into the fiber and/or (iii) possible pump fluctuations can affect the reference fluence values. The selected time steps allow a balance between sufficient data point acquisition and measurement reproducibility over a wide range of temperature and fluence.

The transient reflectivity measurements presented in this chapter are performed by using the system described in Section 4.2.1 with the slightly difference that the changes in the reflectivity of the sample were detected using the *Detector 2* (Section 2.2.4), which is a commercial Andor *Zyla sCMOS* camera.

5.3 Experimental results

As shown in Figure 4.5, the reflectivity changes between 77 and 295 K. To assess if these changes are related to the magnetic state, we systematically measured the static reflectivity as a function of temperature between 77 K and 360 K. Figure 5.1 shows the reflectivity relative to 77 K, when the sample is in the antiferromagnetic state. While at low temperature this normalized signal oscillates around 1, at high temperatures the signal increases significantly, suggesting that changes in the sample occurred around the Néel temperature at $\approx$ 280 K. We note that the reflectivity is also sensitive to other degrees of freedom and as these evolve with temperature isolating the magnetic signal from this data is not trivial.

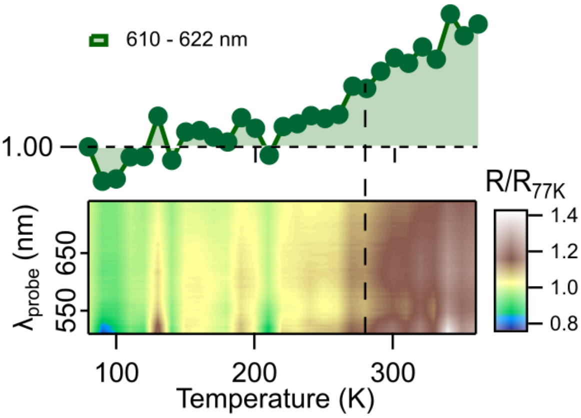

Figure 5.1: **Temperature dependence of the static reflectivity in $\mathbf{Sr_3Ir_2O_7}$.** The signal is shown relative to the value at 77 K (AFM). Top: Lineout at ~610 nm showing a change in reflectivity between low and high temperatures. The dashed line indicates the $T_N \approx 280$K value.

To isolate the magnetic contribution we resort to ultrafast broadband spectroscopy. By analysing the temperature and fluence dependence of the transient spectral shifts, we can identify regions of the spectra that are dominated by the magnetic signal. Figure 5.2 shows typical broadband reflectivity spectra taken above and below T_N at 0.15 ps, following photo-excitation with 800 nm (1.5 eV) laser light at a fluence value of F= 5 mJcm^{-2}. As discussed in Chapter 4, the spectral changes at both temperatures show a suppressed reflectivity at short wavelengths and a signal enhancement above ~600 nm consistent with a shift in the O2p-Ir5d charge transfer resonance [34].

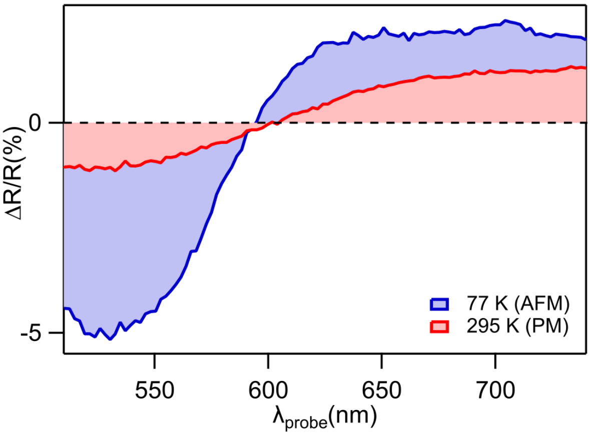

Figure 5.2: **Reflectivity change in $Sr_3Ir_2O_7$ upon 800 nm excitation at 77 K and 295 K.** Both spectra are taken at F= 5 mJcm^{-2} and at a time delay of 0.15 ps.

To establish which region has the most sensitivity to magnetic order and least sensitivity to the other degrees of freedom, we measure a 4D dataset, recording the response of the system at different delay times (t), temperatures (T), probe wavelengths (λ) and fluences (F). We assume that the change in reflectivity can be written as the sum of two components, one related to the electronic degrees of freedom, and the other to the magnetic as $\Delta R = \Delta R(T, \lambda, t, F) = \Delta R_e(T, \lambda, t, F) + \Delta R_M(T, \lambda, t, F)$ where ΔR_M and ΔR_e are the magnetic and non-magnetic (e.g. electronic) contributions respectively. Then, if we know ΔR_e, we can obtain ΔR_M from the measurements. As above T_N ΔR_M=0, therefore we can determine ΔR_e. In the ideal case ΔR_e would be independent of temperature, in which case the high temperature signal could simple be subtracted from the low temperature data to reveal the magnetic dynamics. However, Figure 5.3 shows that certain wavelength regions show significant temperature dependence above T_N. This indicates that the electronic signal is affected by the temperature and without knowing this temperature dependence below T_N it cannot be subtracted. To bypass this issue, we look for a wavelength range at which the above condition is met and assume that remains below T_N. Figure 5.3 shows a detailed temperature scan at different

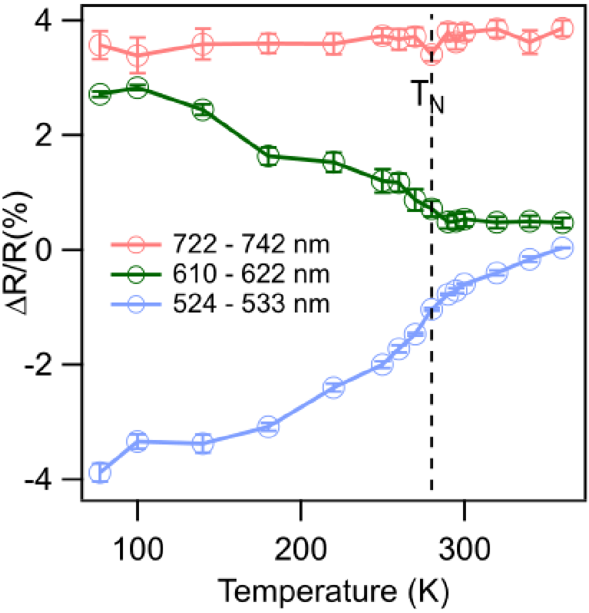

Figure 5.3: **Temperature dependence of the transient reflectivity at different probe wavelengths.** For clarity the traces are offset. The 610 nm region is both sensitive to magnetic order while showing a temperature independent response above T_N. The error bars show the standard deviation of the average of the change on the reflectivity data at each temperature for each region.

probe wavelengths for a fixed fluence and delay, which exemplifies the merits of our approach. From the data in Figure 5.2 alone, one might assume that the 500-550 nm region would exhibit the largest magnetic sensitivity as it shows the largest change when crossing T_N at each fluence value. However, the full temperature scan (Figure 5.3) reveals that this region is strongly temperature dependent above T_N, which precludes extraction of the magnetic signal without a detailed understanding of the non-magnetic temperature evolution of the system. Likewise, at long wavelengths ($>$ 700 nm) the signal shows a temperature independent response above T_N, but lacks magnetic sensitivity. Between these two extremes, we find that wavelengths around 610 nm are unique because the electronic response is temperature independent above T_N, whilst retaining sen-

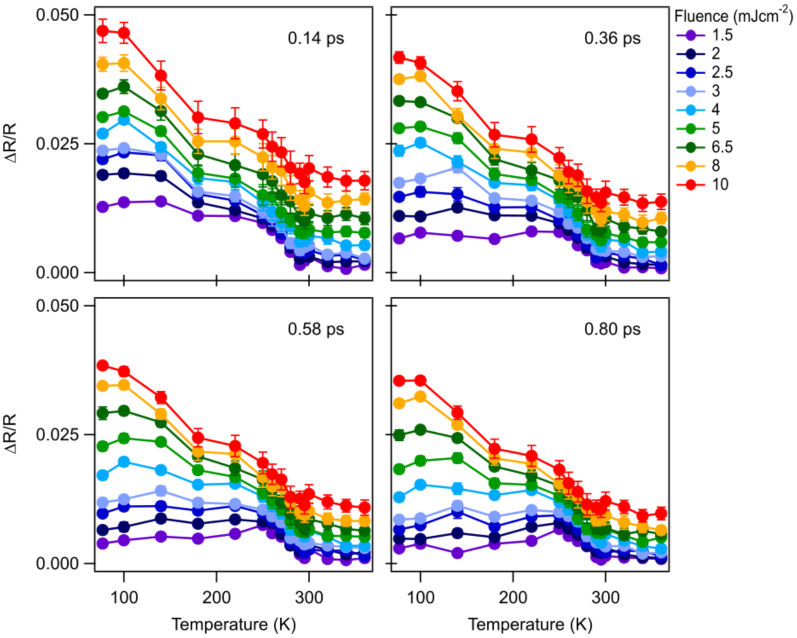

Figure 5.4: **Temperature dependence of the transient reflectivity in the 600-622 nm range** at different excitation fluences measured at a time delay of 0.14 ps, 0.36 ps, 0.58 ps and 0.80 ps. This wavelength in both sensitive to magnetic order while showing a temperature independent response above T_N. This behaviour is observed at all measured fluence and time delays.

sitivity to magnetic order. This remains true for all probed fluences and time delays as shown in Figure 5.4 and as discussed below.

Figure 5.5 shows the magnitude of the reflectivity change after subtracting the electronic contribution from the total reflectivity ($\Delta R_M(T) = \Delta R(T) - \Delta R_e(T > T_N)$) at 610 nm and t= 140 fs, 360 fs, 580 fs and 800 fs time delay. Above T_N the signal is zero at all fluences, as expected from our methodology. At T_N there is a discontinuity and the magnetic response rises sharply for all fluences. The magnetic signal continues to grow for high pump intensities as the sample is cooled, whereas at lower fluences the signal remains flat. Notably, at lower temperatures, larger changes can be induced before saturation, which also requires higher fluences to be reached (see Figure 5.6). Such behaviour suggests that as the temperature is lowered and the system becomes more ordered, more

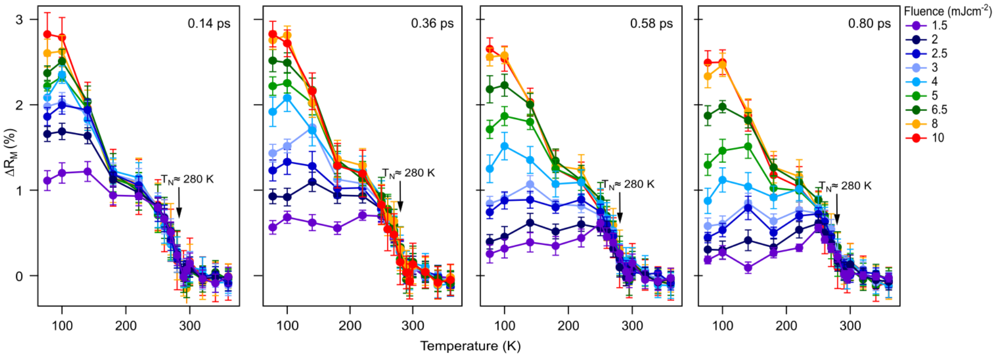

Figure 5.5: **Normalized temperature dependence of the magnetic degree of freedom** (ΔR_M) at different excitation fluences measured at t= 140 fs, 360 fs, 580 fs and 800 fs time delay obtained as $\Delta R(T) - \Delta R(T > T_N)$ in the 610 nm region. The signal saturates at high fluences and at temperatures close the Néel temperature as expected for light-induced demagnetization. The error bars are calculated following the subtraction expression of propagation of error between the error of the average of the wavelength data and the error of the high-temperature data.

energy is needed to perturb it and to demagnetize it. Based on this, we assign the saturation fluence as the fluence required to completely suppress magnetic order. For all temperatures we observe that fluences above ~ 4–5 mJcm^{-2} result in saturation. Thus, we normalize ΔR_M to the value obtained at the highest excitation fluence ($F = 10$ mJcm^{-2}), which provides a scale for a quantitative analysis of the demagnetization.

Next, we analyse the demagnetization dynamics. Figure 5.7 shows the change in the normalized magnetic signal at 77 K when the sample is in the antiferromagnetic state. We observe a sharp change in the magnetic signal immediately after photo-excitation. Notably, we find a very large ($> 50\%$) demagnetization even at low fluences, which is a strong indicator that the magnetic order can be efficiently perturbed by the laser pulse in this material. For comparison, we overlay the time evolution of a magnetic Bragg peak measured at several (high) fluences using XFEL radiation. The differences between the two experimental conditions prevent exactly matching the fluences: The X-ray data was taken from the one reported in Ref. [60] and performed under grazing incidence and with a 2 μm pump wavelength, while the optical data is performed at 800 nm

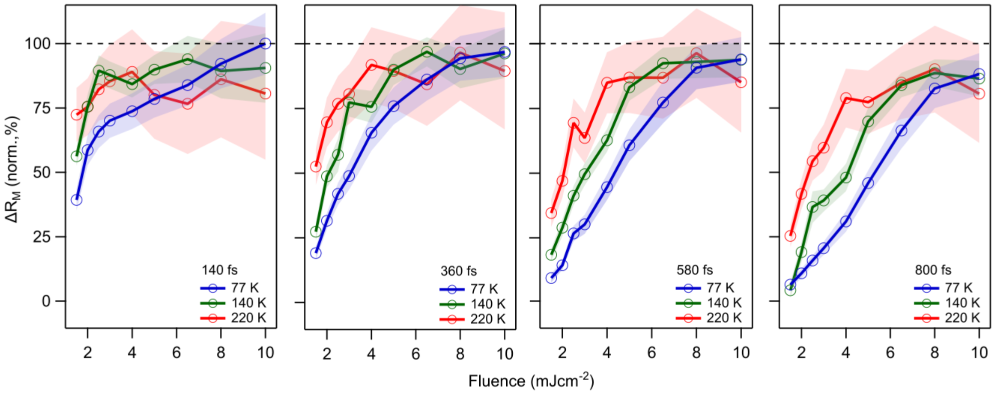

Figure 5.6: **Fluence dependence of the magnetic signal at different temperatures** measured at t= 140 fs, 360 fs, 580 fs and 800 fs time delay showing that full demagnetization is more rapidly attained at higher temperatures. We normalize the maximum ΔR_M value at 10 mJcm^{-2} to 100% demagnetization. Shaded areas indicates the error of the function which are calculated by using the division expression of the propagation of error between the subtracted data error and the error of the normalization value.

and 45 degree angle of incidence. Differences in absorption and reflection coefficients as well as penetration depth miss-matches prevents directly comparing the amplitude of the change and fluence values, but the agreement between the optical and X-ray data is remarkable providing further confirmation that our optical signal is a robust assay of changes in the magnetic order.

Following this initial demagnetization step, we distinguish two regimes in our data: (1) below a threshold fluence $F^{th} \sim 4-5 \text{mJcm}^{-2}$ the signal decays and recovers rapidly; the timescale of such re-magnetization is strongly fluence dependent. (2) Above F^{th} the signal saturates and exhibits a minimal decay within 1 ps, indicating near-complete and permanent demagnetization. The observation of the two regimes, and separating threshold fluence, suggests that laser radiation can access different mechanisms of de- and re-magnetization in the material. Figure 5.8 shows the fluence threshold required to switch between demagnetization regimes as a function of temperature. Red regions correspond to parameters which result in at least a 50% recovery of the magnetic order within 1 ps, whereas blue regions show long-lived demagnetization. The crossover fluence threshold at 77 K is approximately 4 mJcm^{-2} and decreases with

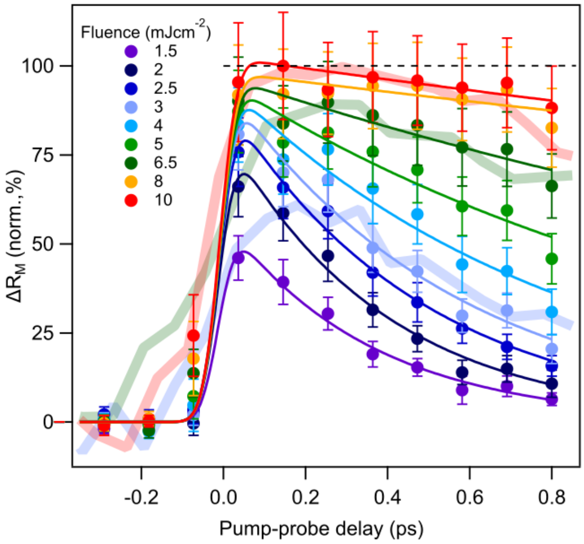

Figure 5.7: **Time-evolution of the magnetic signal measured at 77 K** at different fluences showing fast and large ($> 40\%$) demagnetization as well a change from rapid recovery to permanent demagnetization at F $>$ 4 mJcm^{-2}. For comparison, the time evolution of the magnetic Bragg peak obtained from [60] is also shown (solid translucent lines, scaled). The error bars are calculated by using the division expression of the propagation of error between the subtracted data error and the error of the normalization value. The magnetic Bragg peak data saturates at a value of $\sim$ 70% due to the pump probe miss-match between laser and X-rays. This difference should be much smaller at visible wavelengths. Therefore, to correct for this, we scale the magnitude of the X-ray data by a constant factor.

increasing temperature so that above $\sim$ 200 K only the long-lived de-magnetized state remains.

These results may be explained by a multi-temperature model in which the spin system is quickly heated via the laser excitation and followed by a subsequent cooling through a transfer of heat to the lattice [64]. In this scenario, the long-lived demagnetized state arises simply because all degrees of freedom, including the lattice temperature, have risen above T_N. To test this hypothesis, and taking advantage that we can check the lattice temperature by looking at the phonon mode frequency, we probed the lattice temperature by looking

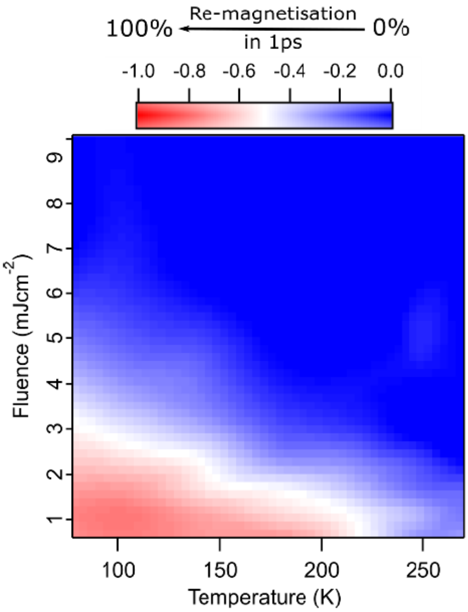

Figure 5.8: **Fluence and temperature dependence of the re-magnetization dynamics.** The plot shows the extent to which the magnetic signal (ΔR_M) recovers (i.e.: decay in Figure 5.7) between the initial excitation t = 0 ps and a delay of 1 ps. The crossover between fast recovery (red) and persistent signal (blue) decreases as the temperature approaches T_N.

to the strongly temperature dependent A_{1g} phonon modes [45]. Using time-resolved coherent phonon spectroscopy, we compared the photo-induced A_{1g} phonon modes with those measured a room temperature. Figure 5.9a shows the high time-resolution scans performed at room temperature and at 77 K. As discussed in chapter , both ~147 cm^{-1} (4.42 THz) and ~181 cm^{-1} (5.46 THz) A_{1g} modes can be clearly resolved in the broadband data and red shift at higher temperature (Figure 5.9b,c). The values obtained are in good agreement with those measured with equilibrium Raman spectroscopy, indicating that low fluence excitation does not significantly heat the system [46]. We know that similar values were obtained using different analysis methods discussed in Section 4.3.

In order to assess the lattice temperature as a function of excitation fluence,

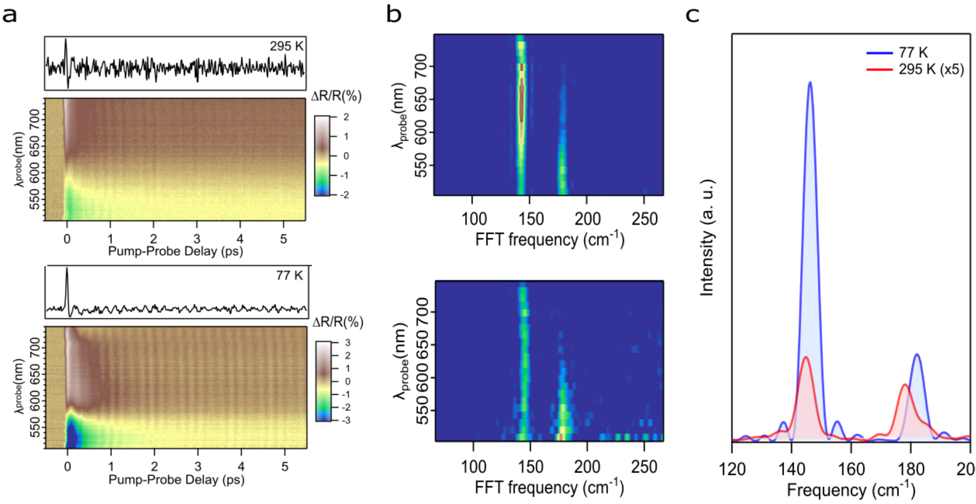

Figure 5.9: **Fourier Transform of the oscillations in the transient reflectivity at 77 K (AFM) and 295 K (PM) at F=2.5** mJcm^{-2}**.** The characteristic high and low energy A_{1g} modes can be captured. The amplitude decreases and the central frequency red shifts with increasing temperature.

we measure the phonon frequencies at 77 K. Although both A_{1g} modes show a gradual red shift with fluence, as expected for heating, we find that the red shift is significantly smaller than that when the system had crossed T_N (Figure 5.10). In particular, at the magnetic crossover threshold (F^{th}) the phonon values are only moderately perturbed, suggesting that a lattice temperature increase is not required to either suppress long-range spin order, nor prevent its recovery.

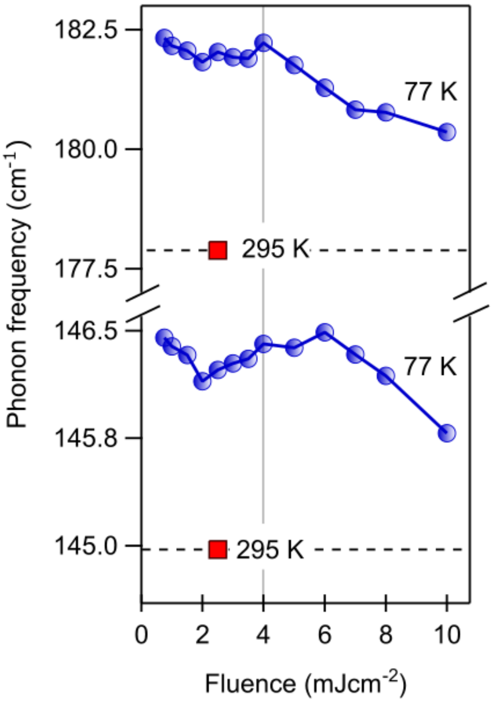

Figure 5.10: **Change in the mode frequency as a function of excitation fluence at 77 K (AFM).** For comparison the frequency measured at 295 K (PM) at low fluences is also displayed (red square). Despite large demagnetization achieved at all fluences, the modes remain mostly unchanged and exhibit only a small inflection at the crossover fluence threshold (F^{th}) but never reach the thermal value.

5.4 Discussion

Our observations can be explained by considering how photo-excitation modifies magnetic order in insulating quantum materials with strong spin-orbit coupling (SOC). Optical excitation creates electron-hole pairs causing changes in orbital occupancies. Due to the small charge gap in $Sr_3Ir_2O_7$, it is energetically favourable to create zero-spin doubly occupied sites following photo-excitation effectively generating ‘spin defects’ in the system (Figure 5.11a) [57]. This configuration is unstable and at low excitation density the excited electron can recombine with its corresponding hole via the emission of phonons. Although it is in principle possible for any electron to recombine with any available hole (leading for example to hole motion), the strong exchange coupling, which is only slightly smaller than the charge gap, disfavours an electron from recombining with a hole that does not result in antiparallel spin alignment. This is depicted in Figure 5.11a and b. If the electron-hole pair recombine before the surrounding spin system has time to react, the magnetic order can be restored without disordering the spin system beyond the initial creation of the spin defects. This suggests a direct link between electrons rapidly relaxing back to the valence band and the fast recovery of magnetic order, as measured at low excitation fluences. We indeed observe that the magnetic recovery in such a regime and the electronic relaxation times measured above T_N are comparable, suggesting electron-hole recombination in the low-density limit can restore the initial spin configuration. Notably, this process is markedly non-thermal as shown by the coherent phonon analysis and represents magnetic perturbations beyond linear spin-wave theory. At higher excitation fluences, a large density of spin defects is created, as depicted in Figure 5.11c. When these defects are close, the energy barrier preventing electron-hole recombination events that result in non-antiparallel spin alignments is significantly reduced. This result in a mixture of parallel and antiparallel spin alignments that eventually disorders the underlying spin network, slowing down the regeneration of the long-range order.

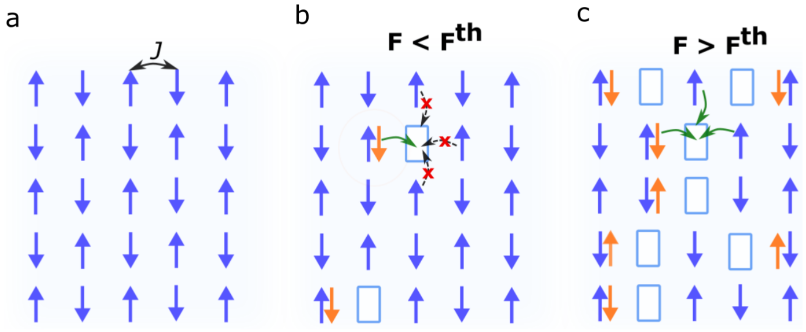

Figure 5.11: **Disorder mediated recovery of magnetic order.** a) Ground state characterized by a large exchange coupling (J) that leads to antiferromagnetic (AFM) order. b) Photo-excitation below the fluence threshold (F^{th}) results in the formation of a small density of spin vacancies and doubly occupied states with zero net moment. Effective destruction of the moment is enabled by the small charge gap. Rapid recombination events regenerate the antiferromagnetic order but recombination paths that produce parallel spin alignments are prevented by the dominant antiferromagnetic exchange coupling. c) Photo-excitation above the fluence threshold. The formation of a large density of spin vacancies relaxes the recombination constraint leading to a long-lived disordering of the spin system.

5.4.1 Plausibility of the results through Monte Carlo simulation

To test the feasibility of this scenario, we examine the recovery of a 3D spin-1/2 Ising model following a change in the magnetic order using a Monte Carlo simulation. We assume the creation of doubly occupied sites can be simplified as direct spin flips, with the flipping fraction depending on the laser fluence. We then count how many Monte-Carlo steps are required to return to the equilibrium conditions (Figure 5.12). When the spin network is only weakly perturbed, order recovers quickly. However, when the system approaches complete demagnetization, the recovery slows down dramatically and the system remains demagnetized. This fast recovery at small perturbations and the generation of a long-lived state at high defect concentrations in the absence of system heating is in good agreement with our experimental observations. We note that this basic model does not honour the complexity of $Sr_3Ir_2O_7$. For example, the model is blind to the mechanism of perturbation beyond imposing an instantaneous change, which is something that will depend on the dominant energy scale of the system. Indeed, while charge transfer in any Mott insulator is expected to produce rapid demagnetization [65], the exact nature of the spin-orbit coupling and the exchange interaction are likely key factors for explaining the magnitude and speed of the switching process [66]. Despite the limitations of the model, this approach allows us to explore the basic response of a system to a disruption of long-range order and highlights the role played by the degeneracy of the spin-disordered state in preventing a rapid recovery. This points towards a central role of disorder in determining the physics of irradiated solids [31]. While disorder has been largely regarded as undesirable, increasing evidence suggest it might be essential in enabling and controlling functionality in systems such as solar cells and photocatalysts and might provide new paths to control the excited state [67, 68].

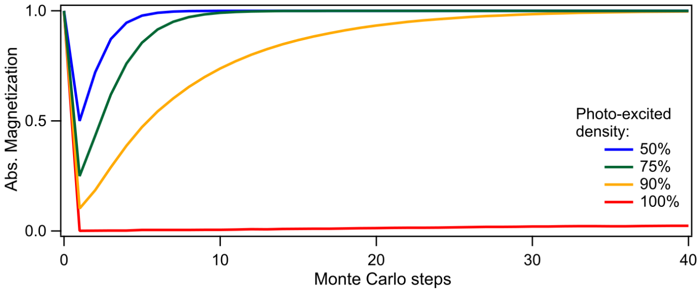

Figure 5.12: **Monte Carlo Magnetization dynamics in a 3D spin-1/2 Ising model** resulting from an instantaneous and random spin flips at different degrees of excitation. If a small fraction of spins is flipped the system recovers fast. In contrast when a large number of spins are flipped inducing large disorder, long-lived change in magnetization occurs.

5.5 Conclusions

In summary, we have shown how photo-excitation of $Sr_3Ir_2O_7$ can non-thermally suppress the magnetic long-range order. We have found a regime, at low fluences and low temperatures, in which we are able to manipulate the magnetic order by up to 50%, but where the system can recover within a picosecond. In contrast, at higher fluences we measure a crossover to a regime in which the magnetic order is completely suppressed for long times, but where the lattice temperature remains below T_N. Such crossover emanates from the generation of photo-induced spin defects that enable a pathway for spin disordering and long-lived breaking of magnetic order. The light-induced, non-thermal change of spin order opens new opportunities to investigate transient phases in solids. In particular, the iridates have long been thought of as the 5d analogues of cuprates, but the disruption of magnetic order through static doping did not allow to induce superconductivity. Optical excitation and manipulation of long-lived spin order might enable a new route to access and stabilize superconductivity.

Chapter 6

Ultrafast structural dynamics in metallic V_2O_3

This chapter shows the incongruity between two experimental results on the study of the lattice dynamics after photo-excitation in the paramagnetic metallic phase of V_2O_3*. Section 6.1 presents a description of the physical properties of* V_2O_3*, as well as, a summary of a combined theoretical and experimental approach performed by Lantz et al. to demonstrate a non-thermal phase developing after ultrafast photo-excitation on* V_2O_3*. Section 6.2 shows a different conclusion of the results measured by time-resolved reflectivity technique upon the same experimental conditions. This work was published by D. Moreno-Mencía et al. in Nat. Commun.* ***10*** *(2019).*

6.1 The physics of V_2O_3

The vanadium oxides are transition-metal oxides that undergo an insulator-metal phase transition (IMT) [69]. This effect was first discovered by Morin in 1959 [70]. Although there are many compounds of vanadium, two of them in particular, VO_2 and V_2O_3, have attracted considerable attention. The insulator-metal phase transition in both materials is accompanied by a structural transition.

As it was discussed in Chapter 1, both materials have been discussed in terms of Mott vs Peierls competition to determine the relative contributions of electron-electron and electron-phonon interactions. In the Mott picture electron-electron interactions drive the metal-insulator transition and the subsequent localization of charge results in the crystallographic distortion, whereas in the Peierls transition, the lattice distortion alone is enough to result in an insulating phase. A major difference between VO_2 and V_2O_3 is that whereas V_2O_3 is antiferromagnetic in the insulating state, VO_2 is not. The antiferromagnetic state in V_2O_3 favours to this material to be a Mott insulator.

While there have been many time-resolved studies on VO_2 to determine the roles of electron correlations and structural distortions on the electronic properties, there has been less work on V_2O_3. Therefore, in this work we investigate the role of correlations and the lattice in the phase transition.

V_2O_3 undergoes a first-order metal-insulator transition from a paramagnetic metallic (PM-M) to a low-temperature antiferromagnetic insulating phase (AFI) around $T_N \approx 150$ K with a seven orders of magnitude resistivity jump. This first-order transition is accompanied by a crystal symmetry change from a corundum to a monoclinic structure [71, 72]. Doping the system with chromium induces a new paramagnetic insulating phase (PM-I) [73], having the same corundum structure but slightly different lattice parameters [74, 75, 76]. The PM-M to PM-I transition has no structural modification and/or magnetic ordering, but it is driven by electron-electron interaction. Replacing vanadium with titanium, the Néel temperature T_N monotonously decreases and above a 5% Ti content the AFI monoclinic phase is completely suppressed. The system becomes a metal with a corundum structure at all temperatures.

The corresponding crystallographic structures for temperatures below and above T_c are displayed in Figure 6.2. At high temperature, the metallic phase has a corundum structure that consists of hexagonal packing of the oxygen atoms, and the vanadium atoms occupying two-thirds of the octahedral cation

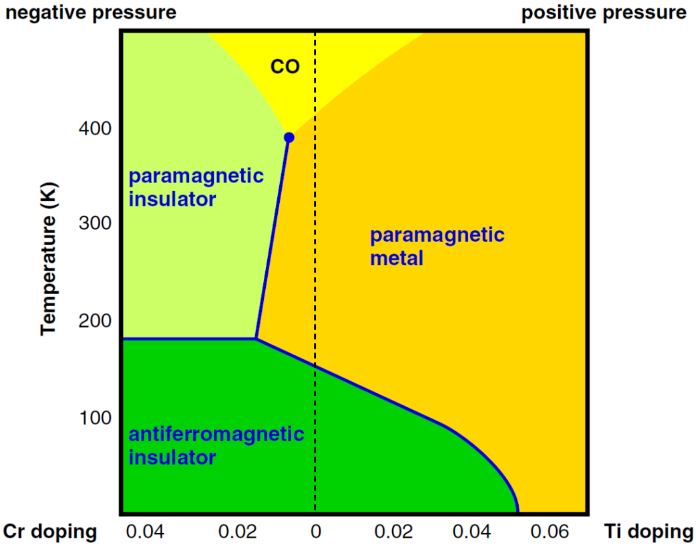

Figure 6.1: **V_2O_3 phase diagram.** Pure V_2O_3 is paramagnetic metal at room temperature. If the temperature is decreased up to $T_c \approx 280K$, the system undergoes to an antiferromagnetic insulator. In contrast, keeping the temperature fixed but changing the Chromium (Cr) concentration level, the system undergoes to a paramagnetic insulator. Reproduced from [71].

sites. The basic features of the corundum structure is shown on Figure 6.2a. The immediate surrounding of the V atoms provided by oxygen atoms has approximate octahedral symmetry [77, 78]. The crystal structure above T_c belongs to the $R\bar{3}c$ group [79, 80]. When the temperature is decreased below T_c, the onset of the magnetic order is also accompanied by a transition from corundum to monoclinic structure which belongs to the B2/b space group (Figure 6.2b) [78, 79, 81].

These changes in the crystal structure make that different phonon modes are observed in the different phases. Through Raman scattering in single crystals of V_2O_3 it has been shown at high temperature (above $T_c \approx 150$ K), V_2O_3 shows a unique A_{1g} symmetry Raman active mode at ~ 247 cm^{-1} (7.5 THz) and two E_g modes at ~ 203 and ~ 290 cm^{-1} (6 and 8.7 THz) while below the transition temperature three A_g Raman modes are found at ~ 230, ~ 280 and ~ 320cm^{-1} (6.9, 8.4, and 9.6 THz) and two B_g modes at ~ 190 and ~ 340 cm^{-1} (5.7 and 10.2 THz) [82, 83]. The low temperature modes will be discussed in more detail in Chapter 7.

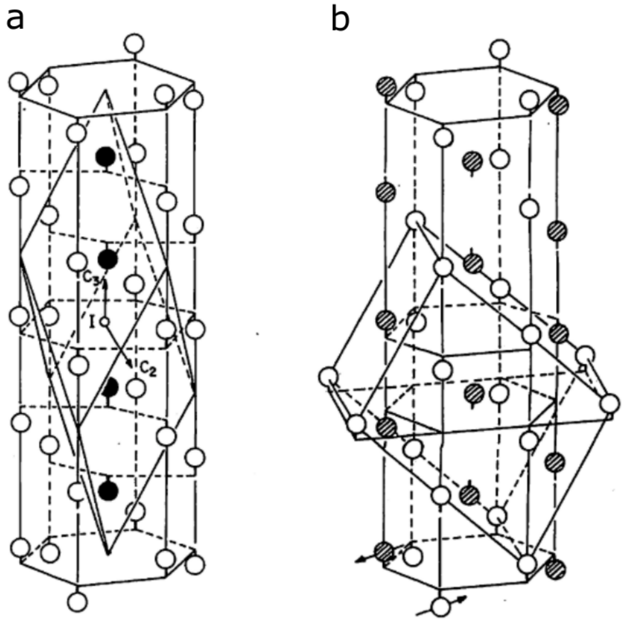

Figure 6.2: **Crystallographic structures of $\mathbf{V_2O_3}$.** a) Hexagonal unit cell with inscribed trigonal primitive cell of V_2O_3 in the metallic (corundum) phase at $T > T_c$. b) Hexagonal unit cell of the corundum phase and primitive cell of the insulator (monoclinic) phase at $T < T_c$. Hatched and open circles represent ions of opposite spins. Taken from [82].

The mechanism that underlies the IMT in the latter material has long been explained with a half-filled single-band Hubbard model, in which the Coulomb parameter, i.e., the electron-electron repulsion, competes with the kinetic energy. Castellani *et al.* [84, 85, 86] found a simple model to predict its density of states, schematically illustrated in Figure 6.3. There, the orbitals are split into t_{2g} and e_g orbitals due to the oxygen crystal field. Afterwards, the two *3d* electrons of the V^{3+} ion are distributed into a lower twofold-degenerate e_g^{π} orbital and an upper non-degenerate a_{1g}^{σ}. The hybridization between the two nearest V atoms causes a large splitting between bonding a_{1g}^{σ} and antibonding $a_{1g}^{\sigma *}$ states [78, 87].

This combination of electronic transition, structural change, and magnetic

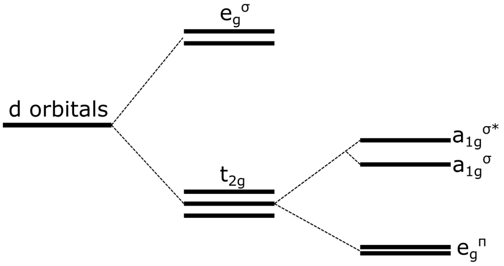

Figure 6.3: **Schematic energy level of V_2O_3.** The d orbitals are split into t_{2g} and e_g orbitals. Since the octahedron has a trigonal distortion, the t_{2g} are split into a lower two-fold degenerate e_g^π and an upper non-degenerate a_{1g}. The The hybridization between the two nearest vanadium atoms, causes a large splitting between the bonding a_{1g}^σ and antibonding a_{1g}^σ states.

transition appear to make V_2O_3 an ideal system to examine the role of electron-electron correlations and Mott physics in the ultrafast regime. Indeed several experiments have claimed to observed dynamics attributed to correlation effects. However, we show that V_2O_3 is a difficult material to work with and that, when the initial state is properly characterized the results are inconsistent with the existing correlation driven theories.

6.1.1 Does metallic V_2O_3 have a transient non-thermal phase?

The Mott insulating nature of V_2O_3 should make it very susceptible to changes in the electronic distribution. The optical excitation of many materials classified as Mott insulators has been used to trigger phase transitions through electronic redistribution. In each case the details vary depending on how strongly the lattice is coupled to the electronic degree of freedom.

To understand if the lattice or the electronic structure is the trigger for the insulator-metal transition has always been a challenge since at equilibrium both change together. In 2012, Lantz *et al.* [88] suggested a theoretical approach to understand the ultrafast evolution of V_2O_3. The central claim is that photoexcitation put charges into the a_{1g} orbital which results in tighter bonding giving rise a blue shift of the A_{1g} phonon mode (hardening). To support this idea, they adopted a combined theoretical and experimental approach. In the theoretical frame, they used the Hartree-Fock (HF) approximation in a three-band Hubbard model. Within this approximation, the total energy has two minima, a stable one at $n_{a_{1g}} \simeq 0.5$ that describes the insulator and, a metastable minimum at $n_{a_{1g}} \simeq 0.625$ that represents the metallic phase. Therefore, transferring ~ 0.13 electrons to the conduction band, would be possible to drive the system from the insulating to a metastable metallic phase, i.e, a non-thermal phase appears in this theoretical scenario since the metastable state pre-exists in equilibrium and can be nucleated directly from the insulator phase through the photo-excitation (Figure 6.4a). Calculations based on the local-density approximation including a parameter U associated to electronic interaction (LDA+U) are able to directly calculate the A_{1g} phonon frequency [89], which shows a blue shift as the a_{1g} occupation increases at expenses of the e_g one. Importantly, the change in lattice potential can still occur when the system is already metallic, i.e. it is not just related to the insulator-metal phase transition.

To verify this theoretical prediction, Lantz *et al.* studied the lattice evolution using time-resolved photoelectron spectroscopy, time-resolved reflectivity (TRR) and time-resolved X-ray diffraction (trXRD). Through this latter technique, they calculated the time-dependent intensity of the Bragg reflections (116) and (024) for the paramagnetic insulator phase. They observed that the evolution of the intensity with time is related directly to the structural dynamics before 4 ps since the centre of mass of the Bragg reflection does not move, this means that the unit volume cell does not change during the first 4 ps, while afterwards the thermal expansion becomes the dominant effect. Then, focusing on the first few picoseconds, they calculated the distance of the nearest vanadium atoms ($d(V_1 - V_4)$) given by the expression

$$d(V_1 - V_4) = (2Z_V - 0.5)c$$

Where, V_1 and V_4 correspond to the nearest vanadium atoms depicted in [78], Z_V is the change of the vanadium position, and c is the lattice constant. Since the (116) and (024) structure factors vary in opposite directions with Z_V, they found that the distance of the nearest vanadium atoms is reduced, consequently increasing the covalent bonding between the a_{1g} orbitals. This tighter bonding would give rise to a blue shift of the A_{1g} phonon mode (Figure 6.4b). To check this shift, they performed a time-resolved reflectivity measurement. Their time traces show coherent oscillations that can be analysed by Fourier transform, thus giving the central frequency of the A_{1g} phonon mode at 8 THz. This mode, as Figures 6.4c and d show, presents a blue shift of up to 14% compared with the equilibrium frequency measured by Raman spectroscopy by Tatsuyama *et al.*

[83] for both paramagnetic insulating and paramagnetic metallic phases. Thus, suggesting that there is a non-thermal phonon hardening. In addition, a time-resolved photoelectron spectroscopy measurement was performed to directly probe the electronic structure. They showed how the electrons are not relaxed in the paramagnetic insulating state after 2ps of photo-excitation. However, in the paramagnetic metal state is almost thermalized at 400 fs. The observed spectral changes obtained by keeping the sample at a fixed temperature T and photo-exciting with a pump pulse cannot be ascribed to heating, but rather to a non-thermal transient state. In particular, the measured spectra suggest that there is more weight both below and above the Fermi energy in the photo-excited state at T than in the equilibrium state at $\mathrm{T} + \Delta\mathrm{T}$. Therefore, the reduction of density of states around $\mathrm{E_F}$ is not compatible with a thermally excited configuration.

Although there is a convincing evidence for an ultrafast change in the lattice potential in V_2O_3, there are also some unresolved issues. Specifically, the same effect was observed in both the paramagnetic insulating and paramagnetic metallic state. In the metallic state there is no meta-stable state as the system is already metallic. As there is no gap, it is hard to see why the electrons would not relax back to a hot Fermi-Dirac distribution rapidly as metals typically show, instead of keeping the non-thermal difference. Secondly, although the two Bragg peaks suggest a change in the vanadium bond length, it is based on the assumption that only the vanadium motion explains the data and more Bragg peaks would be needed to check for consistency. Furthermore, no fluence dependence was measured. At low fluences, the phonon frequency should match the Raman data. Indeed, previous measurements show a good agreement between the Raman and coherent phonon frequencies [90]. Therefore, one would expect a strong fluence dependence for the phonon. Finally, the Raman measurements were not performed on the same sample and in order to check for issues related the sample quality, the Raman and time-domain signals should be measured on the same sample.

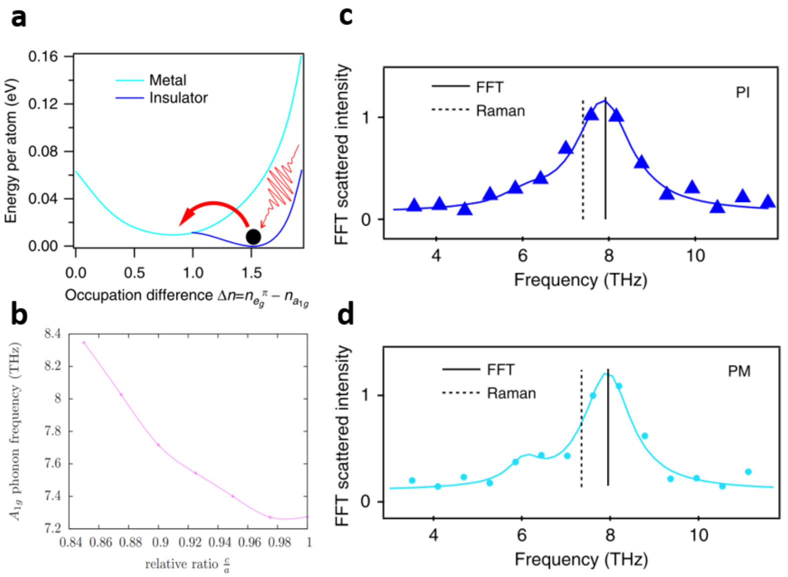

Figure 6.4: **Theoretical and experimental approach of the ultrafast evolution of** $\mathbf{V_2O_3}$**.** a) Hartree-Fock total energy as function of the occupancy differences between $\mathrm{e_g^\pi}$ and $\mathrm{a_{1g}}$ orbitals. b) Theoretical $\mathrm{A_{1g}}$ phonon frequencies as a function of the ratio c/a of the hexagonal structural parameters. c,d) Fast Fourier transform of the transient reflectivity traces compared with equilibrium Raman spectroscopy (dashed line) for the PM-M phase and PM-I phase, respectively. Taken from [88].

6.2 Investigating the non-thermal phase in V_2O_3.

To test if the transient state is stabilised by lattice distortion due to an overpopulation of the a_{1g} electronic orbital, we have repeated the time-resolved reflectivity measurements performed on the paramagnetic metallic phase and on several different pure V_2O_3 samples. The data shown in Figure 6.5 is measured on a single crystal of the paramagnetic metallic phase of V_2O_3. The samples were grinded and polished using grinding disk papers and polishing cloths with diamond suspension down to 3 μm to give a (001) surface normal. A sharp first-order insulator-metal phase transition at 165 K, often resulting in the crystal shattering, shows that our samples are of high quality and correspond to stoichiometric V_2O_3.

The first experiments were carried out in the pump-probe setup described in Section 2.2.2 pumping at 800 nm with pump fluence of 8 mJcm^{-2} at a frequency of 1 kHz. The pump-probe measurements were performed in a cross-polarised geometry at normal incidence and the sample was placed inside the liquid Nitrogen cryostat held at 200 K in order to reproduce the experimental conditions reported in [88] but with one significant difference in our measurement: we use a broadband optical probe and frequency-resolve detection, which provide greater sensitivity to the phonon oscillation. Figure 6.5 shows the wavelength dependence of the transient optical response after correcting for the chirp of the white light probe.

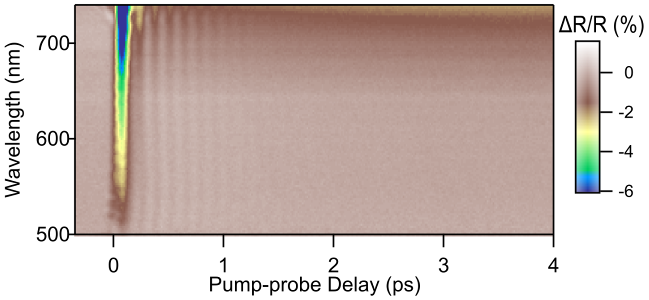

Figure 6.5: **Transient response of V_2O_3 to photo-excitation.** Time- and wavelength-resolved response of V_2O_3 after excitation with a 40 fs 1.5 eV pump pulse at 1 kHz repetition rate, a pump fluence of 8 mJcm^{-2} and a base temperature of 200 K.

The response is similar to that observed by Lantz *et al.* [88] with a spike-like feature near t=0 and coherent oscillations over a slowly varying background. After a broadband exploration, we saw the response is similar at all wavelengths, but the relative strength of the peak and oscillation amplitude changes for different wavelengths with an average of 100-nm section of the wavelength data centred at 550, 600 and 700 nm, as it is depicted in Figure 6.6. For the incoming results, we select the 600 nm average region to avoid a dephasing due to the chirp not being completely compensate.

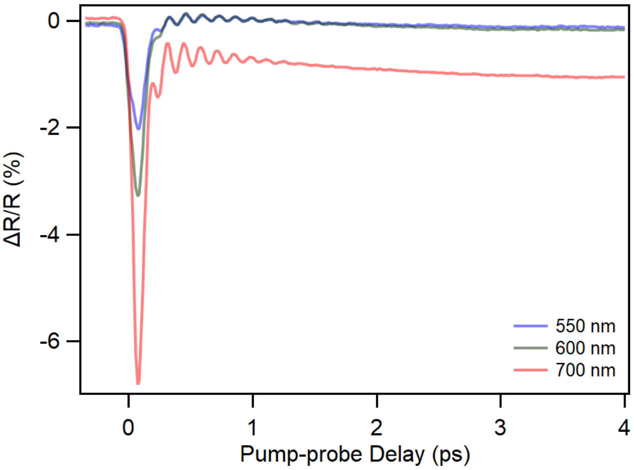

Figure 6.6: **Time traces of** V_2O_3 **at different wavelengths.** Each time trace is averaged over a 100-nm-wide region, centred at 550 nm (blue), 600 nm (green) and 700 nm (red).

In order to obtain a more precise value in our results obtained for the phonon frequency, we calculate it through two different methods:

Method 1: First, we fit the phonon oscillations directly from the transient data at 600 nm through the expression

$$f(t) = Ae^{-2\pi\gamma f_{A_{1g}}(t-t_0)}\cos\left(2\pi\left(\sqrt{1-\gamma^2}f_{A_{1g}}(t-t_0)-\varphi_1\right)\right)+$$
$$B\sin(2\pi(f_s(t-t_0)-\varphi_2))+Ce^{-(t-t_0)/\tau}+D$$

where A, B, C and D correspond to different amplitudes, γ is the damping term, t_0 is the initial time (t=0), φ_1 and φ_2 are the phases of the cos and sin respectively, f_s correspond to a slow dynamic, τ is the time constant and $f_{A_{1g}}$ is the phonon frequency parameter that we are interesting in obtaining. Figure 6.7a shows a zoom of the transient, together with a time dependent fit to the transient data, which resulted in a central frequency of 7.41 ± 0.01 THz (247 cm^{-1}).

Method 2: As a second analysis method, we remove the background of the transient response by differentiating it, as performed by [90], which acts as a complex low-pass filter for the slow dynamics. A fast Fourier transform (FFT) of the result was then calculated, after excluding the range close to the spike at t=0. The resulting FFT is shown in Figure 6.7b. The FFT was fitted by the Lorentzian function

$$f(x) = \frac{\gamma}{(x - x_0)^2 + \gamma^2} + y_0$$

where γ is the scale parameter which specifies the half-width at half-maximum, y_0 is an offset corrector parameter and x_0 is the central frequency of the phonon. The Lorentzian fit to the FFT gives a central frequency of 7.51 ± 0.01 THz (250 cm^{-1}).

The discrepancy in frequency obtained from the two methods of analysis of the same data is larger than the error reported by the fitting algorithm in either case. This shows that the main error in determining the mode frequency arises from how the background is processed. We determine the frequency of the mode to be 7.46 ± 0.05 THz by using the mean and standard deviation of the two fit results. This frequency is significantly slower than 8 THz, the response observed by Lantz *et al.* [88] despite being measured in the same configuration. Our results is more similar to the 7.5 THz value observed by Kuroda *et al.* using Raman spectroscopy.

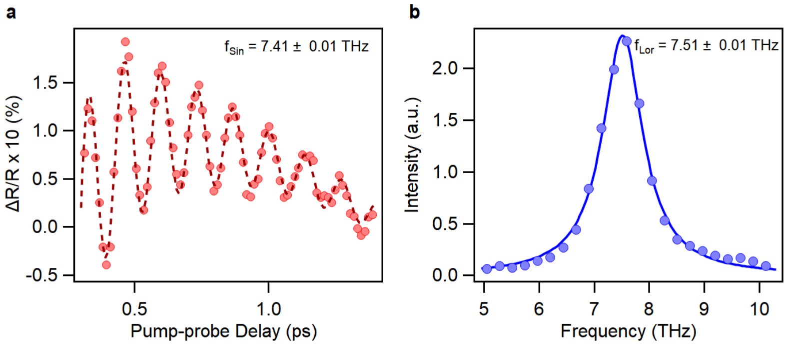

Figure 6.7: **Extraction of the phonon frequency. a)** Zoom of the transient data to show the measured coherent phonon oscillations (circle) together with the fit (dashed line) with a 7.4 THz mode. **b)** Fourier transform of the transient data (blue circles) after differentiation, in order to remove the slow dynamics. A Lorentzian fit (blue line) gives a central frequency of 7.5 THz.

In order to ensure that the Raman value of the initial state agrees with literature values, Raman measurements were also performed on the same sample at room temperature using the Raman microscope described in Section 2.3. Regarding to which laser source it is better to use, we found that apart from a change in the background level, there is not a high significant change on the Raman spectra. Figure 6.8a shows an example in which one of the Raman spectrum has a short exposure time ($\sim$ 60 seconds) and the other spectrum has the optimal exposure time ($\sim$ 300 seconds) where two phonon modes are clearly observed. The first peak ($\sim$ 6 THz) corresponds to the E_g mode, which is not measured in our time-resolved measurement, and the second corresponds to the observed A_{1g} mode. These mode frequencies are in good agreement with the literature [82]. Figure 6.8b shows a comparative plot of the Raman spectrum excited by 532 nm and 785 nm in a second V_2O_3 sample. We can see that at 785 nm, the E_g mode seems to be more sensitive, while the A_{1g} is more similar between them.

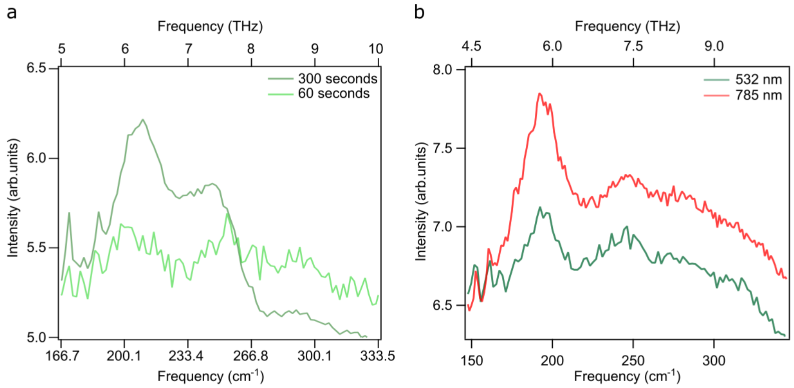

Figure 6.8: **Raman spectrum at different exposure times and pump sources.** **a**) At short exposure times (light green) the modes are barely visible, whereas at longer exposure times (dark green) we can distinguish two modes at ∼ 6 THz (E_g mode) and at ∼ 7.5 THz (A_{1g}). **b)** Raman spectrum at different pump sources. Both spectra barely change in the range of 4.5-10 THz (150 - 330 cm^{-1}) when V_2O_3 is excited with 532 nm (green line) or 785 nm (red line). These spectra belongs to a second V_2O_3 single crystal.

To extract with more precision the central frequency of the A_{1g} Raman mode, we used a multi-Lorentzian fit and a linear background as it is depicted in Figure 6.9a. Here, a small red shift can be expected due to the thermal induced softening of the mode, i.e., we expect it to be slightly lower in frequency than the data recorded at 200 K. A value of 7.4±0.03 THz was obtained. Again, this value can change if the background function is also modified, and the true error will be larger than the value reported by the fit. However, even with this lower bound, the Raman and time-domain frequencies (7.46 THz) obtained can be considered the same, to within the combined error bars. Therefore, we conclude that light does not induce a significant blue shift (Figure 6.9b), in disagreement with the Lantz *et al.* results [88].

In order to investigate the discrepancy with Lantz *et al.* further, we performed a range of fluence-dependent measurements on different samples of stoichiometric V_2O_3 and at different fluences. Samples 1 and 2 were grown and polished by a collaboration at John Hopkins University using the methods described at the beginning of this section, while sample 3 was provided by Lantz *et al.* research group in the Solid States Physics Laboratory of Paris-Saclay University. We show these data only for the purpose of reporting scientific val-

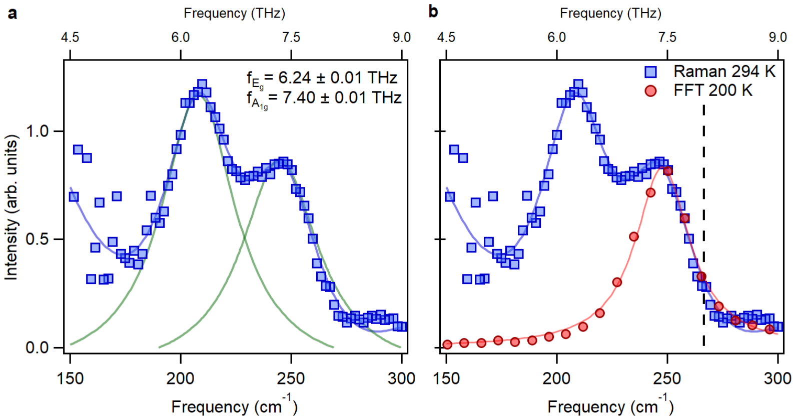

Figure 6.9: **Raman fit at 294 K.** a) Raman spectrum (blue squares) was fitted by a multi-Lorentzian fit (blue line). The Lorentzian peaks (green lines) represent the E_g mode with a frequency of 6.24 THz and the A_{1g} mode at 7.4 THz. b) A_{1g} mode from our Raman spectrum is in good agreement with the FFT data (red circles) previously calculated. The dashed line is the blue-shifted frequency reported in [88].

ues. Figure 6.10 plots the mode frequency as a function of power resulting from a Lorentzian fit to the Fourier transform of the background subtracted data at room temperature. In sample 1, we find that the frequency of the response can change by 3% by moving to different spots in the same sample, which otherwise showed no obvious difference in the optical appearance (sample 1a vs sample 1b in Figure 6.10), indicating that residual strain from polishing may change the frequency. Agreement can also be found between different samples (samples 1a and 2). The largest discrepancy we have observed is 0.6 THz (sample 1b and sample 3). This shows the measured mode frequency is very sample dependent and depends strongly on sample preparation, this is important because a saturated orbital will no longer produce a blue shift.

Finally, we point out that as the reported blue shift is driven by the population in the a_{1g} electronic level, one would expect the magnitude of the shift to increase or decrease with increasing or decreasing fluence as more or fewer electrons are excited into that orbital. However, we only observe a small red shift with increasing fluence, opposite of what is expected for a non-thermal lattice potential, but consistent with some thermal heating. In addition, despite

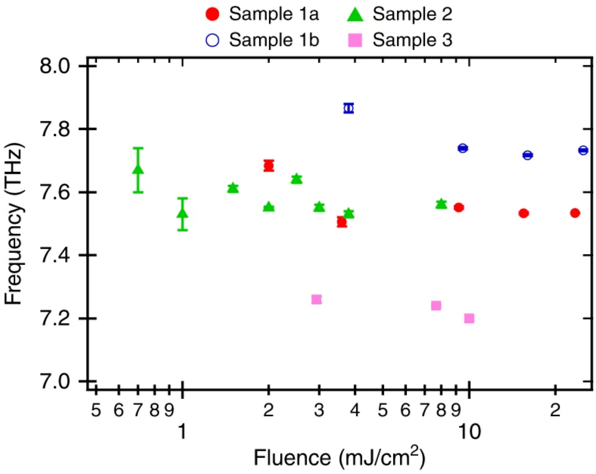

Figure 6.10: **Fluence dependence of the time-domain frequency for several samples of** V_2O_3. Samples 1a and b where measurements performed at two points on the same sample. A variation of 0.6 THz ($\sim$ 8%) is found over the samples measured. Error bars correspond to the error from the fit of the Lorentzian obtained from Fourier transforming the time-domain data and are an underestimate.

changing the fluence by almost two order of magnitude, the phonon amplitude and reflectivity change continue to increase, showing that the a_{1g} orbital population has not saturated, since a saturated orbital will no longer produce a blue shift.

In conclusion, we found no evidence for a transient non-thermal phase in V_2O_3 that is established by a lattice distortion and photo-induced hardening of the A_{1g} phonon mode as claimed in Ref. [88]. Good agreement between Raman and time-domain signals can be found when the measurements are performed on the same sample. There is no light-induced hardening and we do not find any evidence for control of the lattice structure by selective excitation of the a_{1g} orbital in this compound. Our results show that there can be a large variation in A_{1g} phonon mode frequency both within and between samples, which needs to be taken into account when comparing measurements with literature values. Thus, we believe that the 8 THz measured by Lantz *et al.* [88] was likely due to strain or other inhomogeneity in the system and it was the source of the difference with static Raman measurement. Our results highlight the difficulty in assessing the phase transition and the importance of performing the same experiment on the same sample in order to obtain quantitative results. This is particularly important in materials where the volume and structure changes can lead to sample cracking and sample heterogeneities, a point which is discussed in the next chapter.

Chapter 7

Tracking the ultrafast phase transition in V_2O_3

In contrast to the previous chapter, this chapter focuses on the low temperature phase and the light induced phase transition in the V_2O_3 *correlated material. Section 7.1 provides an introduction explaining how photo-excitation induces changes on the lattice potential and shows one of the first examples of tracking the phase transition by the evolution of the phonon spectrum in* VO_2*. A similar experiment in* V_2O_3 *is shown in Section 7.2, which presents the difficulties that working with crystals that have a large volume change at the phase transition and presents our results in a thin film of this material. The conclusions of the chapter are discussed in Section 7.3.*

7.1 Introduction

Photo-excitation on correlated materials can be used to control and manipulate their structural [91], electronic [92] and magnetic [93] degrees of freedom as well as exposed properties not accessible under equilibrium conditions. Such changes are most clearly identified in materials that undergo structure phase transitions. Tracking these processes is non trivial as they occur over multiple times and length scales. Moreover, identifying a single parameter to characterize the phase change is not always possible. In the case of structural phase transition, the lattice potential determines the atomic structure with the atoms occupying the minima of this lattice potential, but also the phonon spectra, which proceeds from the curvature of the potential. Thus, if photo-excitation drives a structural transition, it can be tracked through either mechanism.

X-ray or electron diffraction can be used to track the changes in structure as these techniques map ionic positions into specific Bragg peaks [27, 94, 95]. The changes on these peak suggest a change in ionic positions and extending these techniques into the time domain offers a route to monitor the phase transition on its fundamental time scale. Similarly, the phonon spectra of the solid can be measured by Raman scattering, which measures the Raman active modes [96]. However, the time resolution of these experiments is low to reveal changes on the transient symmetry. To overcome this limitation, coherent phonon generation can be used. As it was discussed in Chapter 1, in absorbing materials, the laser light redistributes charges within the solid. This redistribution generates a force into the lattice. The restoring forces experienced by the ions are dictated by the superposition of the phonon modes of the lattice potential [97]. If the force generated has a duration shorter than the period of the phonons, coherent motions of the lattice are induced. This motion can be tracked in the time domain by measuring the effects of the coherent phonons on the transient reflectivity of a material and has been used extensively as a probe to study the lattice in near-equilibrium conditions in the vicinity of phase transitions [98]. The critical number of modes typically changes when the symmetry of the potential changes.

Tracking of the progress of the ultrafast phase transition through coherent phonons was used in vanadium dioxide, VO_2, [99, 100]. The material changes from a low-temperature monoclinic M_1 phase to a high-temperature rutile R phase at approximately 340 K [70, 101]. In 2012, Wall *et al.* [99] demonstrated that photo-induced coherent oscillations can be used to measure the evolution of the phonon spectrum during the insulator-metal phase transition of VO_2. They found how, by exciting the material with sufficiently intense pump pulses, the amplitude of the four lowest modes of the 9 A_g Raman active phonon modes of the monoclinic M_1 increased with fluence up to the fluence threshold, F_{th}, was reached (Figure 7.1a). At this point, the mode amplitude decreased and disappear, leaving the decaying transient to dominate the dynamics. This is indicated in Figure 7.1b, which shows the Fourier transform of the signal when the system was excited well above the phase transition threshold. In this case, the signal consist of a single broad feature, and the normal modes of the monoclinic phase cannot be identified. By performing a broadband probing of the phase transition, it was demonstrated that this complete loss of the four M_1-phase phonons was not an optical probe-related artefact because, below the threshold fluence, coherent oscillations were observed at all wavelengths (Figure 7.1c). However, these oscillations disappeared across the whole probed spectrum above the phase transition (Figure 7.1d). These results suggest that when a sufficient number of electrons are excited, their perturbation to the lattice potential becomes large enough to modify the symmetry, driving the system into the R phase.

The advantage of this technique lies in that it can directly probe the structure of the sample using only optical probes and does not requiere X-rays. However, there is also a drawback to these measurements: the state of VO_2 immediately after photo-excitation could not be determined. This happens because the four Raman active phonon modes of the metallic phase are hard to observe with regular Raman scattering or coherent phonon generation [100]. Thus, optical methods alone could not determined if the structure of the material was in the metallic phase or some other intermediate structure. To provide a final answer it was necessary to resort to time-resolved X-ray diffuse scattering [31].

One phase-change material in which all the Raman active phonon modes can be observed optically is V_2O_3. As discussed in chapter 6, Kuroda *et al.* [82] studied the Raman scattering in single crystals of V_2O_3 in the range from 20 K to room temperature. They observed that the spectra showed a drastic change at $T_c \sim 150$K. At low temperature, in the monoclinic insulating phase, V_2O_3 shows multiple A_g Raman active phonons at ~ 230, ~ 280, and ~ 320 cm^{-1}, which correspond to ~ 6.9, ~ 8.4, and ~ 9.6 THz, respectively. However, more importantly, the high temperature metallic corundum phase retains a unique A_{1g} symmetry Raman active mode at ~ 235 cm^{-1} (~ 7 THz), which is not found in the low temperature state. Both Raman scattering spectra are shown

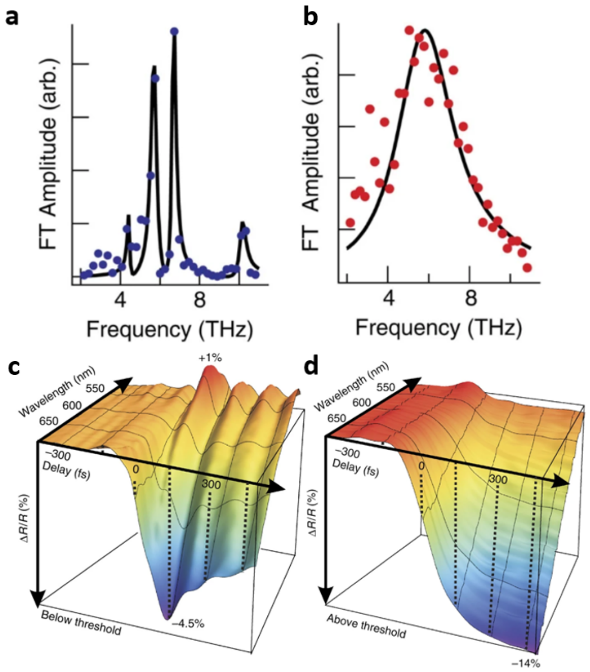

Figure 7.1: **Transient reflectivity and dynamics of $\mathbf{VO_2}$.** a)Fourier transform of the transient reflectivity for below the fluence threshold. b) FFT above the fluence threshold. c) Transient reflectivity as a function of probe wavelength and delay below the fluence threshold. d) Transient reflectivity as a function of probe wavelength and delay above the fluence threshold. Taken from [99].

in Figure 7.2 together with a frequency shift of these modes as a function of temperature. The properties of V_2O_3 are summarized in Table 7.1.

In this chapter, we take the advantage that the phonon modes of the metallic and insulating phases can be monitored optically, and use coherent phonon generation to track the state of the lattice throughout the phase transition. Using this all-optical method, we aim to stablish whether the lattice potential in V_2O_3 is switched directly to the metallic phase and if this can still induce vibration coherence in the phase transitions, i.e., can the excitation of the low temperature phase induce coherent vibrations in high temperature structure?

Temperature	**Phase**	**Crystal structure**	**Phonon modes (THz)**
T>T_c (>150 K)	Paramagnetic metal	Corundum	A_{1g}: 7 E_g: 6, 9
T<T_c (<150 K)	Antiferromagnetic insulator	Monoclinic	A_g: 6.9, 8.4, 9.6 B_g: 5.7, 10.2

Table 7.1: Phases, crystal structure and phonon modes above and below the transition temperature in V_2O_3 [82, 83].

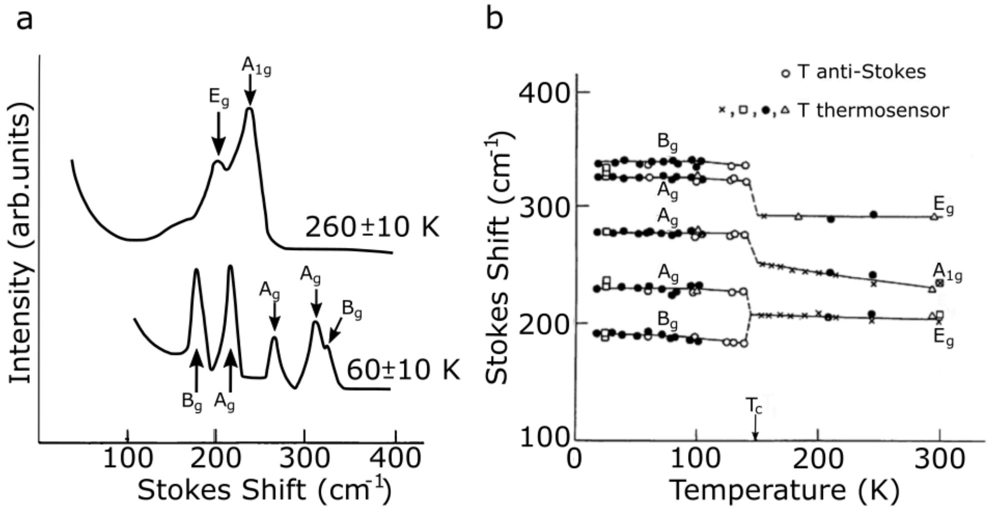

Figure 7.2: **Raman active phonon modes in** V_2O_3**.** a) Spectra of Raman scattering at above (260 K) and below (60 K) of T_c. At low temperature, V_2O_3 shows multiple A_g Raman active phonons at $\sim$ 230, $\sim$ 280, and $\sim$ 320 cm^{-1}, and B_g modes at $\sim$ 190, and $\sim$ 330 cm^{-1}. At high temperature, there is only one A_{1g} Raman mode at $\sim$ 250 cm^{-1} and one E_g phonon mode at $\sim$ 200 cm^{-1}. b) Frequency shift as a function of temperature for the scattering peaks found in **a**. The temperature represented by squares, triangles, crosses and filled dots were taken by a GaAs thermosensor at different times. A better estimate of the temperature at which the scattering effectively occurred was obtained from the intensity ratio of Stokes and anti-Stokes scatterings (empty dots). Adapted from [82].

7.2 Coherent phonon spectroscopy in V_2O_3

In this section, we first discuss the experimental challenges associated with measuring single crystals of V_2O_3 and show that cracking of the sample upon the structure transition prevents systematic data collection. We then show how to bypass this issue by measuring thin films.

7.2.1 Experimental challenges in pump-probe spectroscopy measurements of single crystal of V_2O_3

The physical characterization of phase transition is best performed using single crystals. Due to the slow and controlled growth condition of these samples they sustain lower defect concentration and higher homogeneity than polycrystalline samples. As a consequence, single crystals exhibit sharper phase transition, occurring within a smaller temperature range. Most importantly, the highly oriented nature of single crystals facilitates a full symmetry analysis of the phonons providing an excellent platform to characterize phase transitions.

We measured single crystals of V_2O_3 under different experimental conditions. However, we observed that upon cooling the sample below T_c the structure change from corundum to monoclinic caused the sample to crack, even to the point of being completely destroyed. Cracking occurred regardless of the rate at which the sample was cooled (~0.05 K/min). Figure 7.3 shows an image before and after the cooling procedure. We observed that cracking has two main consequences: (1) it changed the overall reflectivity of the sample and (2) it increased the sample heterogeneity. These hindered systematically data collection and impacted measurement reproducibility.

The complexity of measuring single crystals of V_2O_3 is exemplified in Figure 7.4, which shows data collected in two different experimental rounds. Upon photo-excitation a sharp decrease in reflectivity is observed. Subsequently, the signal recovers within less than 200 fs and is followed by a flat residual signal. We observed that under the same experimental conditions, the transient amplitude increased from one round to another (Figure 7.4a). In addition, the signal is also modulated by coherent oscillations. To extract the frequency of the oscillations, we first differentiated the data in order to remove the incoherent exponential decay component and subsequently performed a fast Fourier transform. In the first round of measurements we captured three monoclinic phonon modes at 6.9, 8.4, and 9.6 THz (black dashed lines in Figure 7.4b).

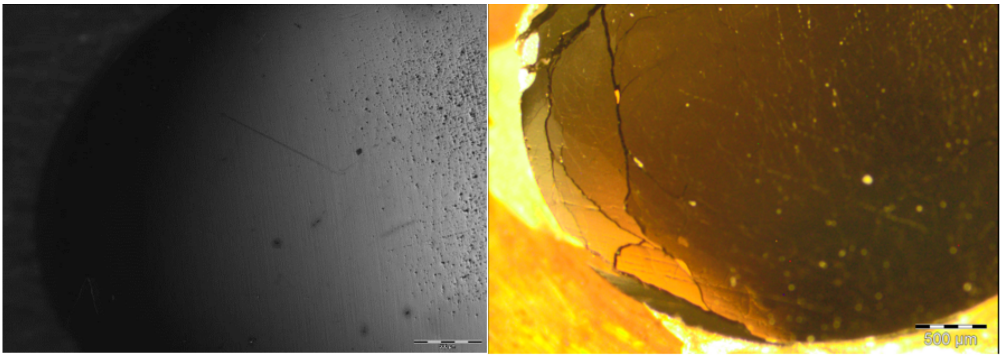

Figure 7.3: **Cracking on the V_2O_3 sample.** Sample breaks after going down the T_c. The left image shows the sample before crossing T_c, whereas the right image shows the sample after crossing T_c.

These values are in good agreement with those measured in equilibrium Raman spectroscopy [82, 83]. As the fluence increases above 4 $mJcm^{-2}$, we observe the metallic mode (∼7.4 THz) starts to appear (red dashed lines in Figure 7.4b) and that the amplitude of this mode increases with increasing fluence. However, despite the appearance of the metallic mode, we observe that the characteristic frequencies of the antiferromagnetic insulating phase are still presents. This could represent some form of pump induced heterogeneity, in which part of the sample is transformed into the metallic phase, and oscillates coherently, while another part remains insulating.

The poor homogeneity of the sample is corroborate by subsequent measurements under the same experimental conditions. The Fourier transform of round 2, shown in Figure 7.4c, shows the three antiferromagnetic phonon modes (black dashed lines) only appear at low fluences with frequencies at 6.8, 7.8, and 9.4 THz (inset Figure 7.4c). These frequencies are shifted to lower values relative to those of round 1. Moreover, in round 2 we observe that at 4 $mJcm^{-2}$ the 7.5 THz mode appears while all the monoclinic insulating modes disappear. In this case, it appears that the whole sample was transformed to the metallic phase. However, the lack of repeatability is worrying. In particular, why in one case can part of the sample remain monoclinic at 8 $mJcm^{-2}$ while in another case the sample is completely switched?

An alternative possibility is that the sample is heated by the laser above T_c statically. In this case, as the fluence increases so does the sample temperature, resulting in some or all of the probe volume being metallic at all times. While this is usually only a problem for free standing thin films [102], it may be an issue here as V_2O_3 has a very low thermal conductivity. In addition, cracking may reduce the thermal contact with the cold finger of the cryostat preventing heat dissipation. To circumvent this problem, we next use thin films of V_2O_3. This sample consist in highly oriented polycrystal with gaps between the grains and thus is less likely to crack upon structure changes.

7.2.2 Pump-probe spectroscopy measurement on V_2O_3 thin films

The measurements were performed on 56 nm thick thin-film of V_2O_3 deposited onto 60 nm Cr_2O_3 buffer layers on sapphire substrates. This sample has a transition temperature around 145 K. The measurement was carried out in a similar experimental setup to the one described in Section 2.2.2 where the light source is coming from a Ti:Sapphire laser operating at 1 kHz with a central wavelength of 800 nm, giving sub 100 fs pulses. In addition, two optical parametric amplifiers (OPA) are used to obtain a tunable laser source. One of the OPA generates pulses tunable over the visible range, from 500 to 1000 nm with a sub 15 fs pulse width. The other, produces pulses tunable over the near infrared wavelength range, from 1140 to 2700 nm with a sub 50 fs pulse width. For this measurement, we pump at 700 nm and probe at 1800 nm. The sample was placed in a closed Helium cycle cryostat that cools down up to 15 K. Thus, the sample can be kept at a temperature below T_c, avoiding possible cracks.

First, we characterized the thin film above the transition temperature at 154 K. When pumping the metallic state, we observe a sharp decrease in reflectivity at t=0 with an initial fast recovery of less than 0.5 ps (Figure 7.5a). The subsequent transient signals show a strong dependence with the excitation fluence. For example, while at 7 $mJcm^{-2}$ the signal grows with time, at 10 $mJcm^{-2}$ the signal decreases with time. Such behaviour is likely due to expansion effects of the thin film layer after pumping. Thin films create interference in the reflected light, as the thickness of the film changes due to thermal expansion, such interferences manifest also in the optical reflectivity. Regardless of this change at all fluence, the signal is strongly modulated by coherent oscillations below 2 ps. The Fourier transform of the oscillating component is shown in Figure 7.5b. We observe a single broad phonon at 7.3-7.4 THz, characteristic of the metallic state, which linearly red shifts by 0.2 THz as the fluence is increased (Figure 7.5c). These results are consistent with our previous broadband measurements of the high-temperature phase in single crystals and corroborate that photo-excitation of the metallic phase launches coherent oscillations at the same frequency observed in static Raman.

Having characterized the high temperature metallic state at this probe wavelength, we next monitor the photo-induced phase transition at 25 K. As shown in Figure 7.6a, the reflectivity signal increases after the photo-excitation and is followed by a slow varying change. The signal is also modulated by coherent oscillations. The Fourier transform at 2.5 $mJcm^{-2}$ shows two phonon modes with frequencies of 8.3 and 9.85 THz (Figure 7.6b), which are in a good agreement with those measured with Raman spectroscopy [82, 83] and they are characteristics of the low temperature phase. Figure 7.6c, shows the evolution of these modes as a function of fluence. We observe that the amplitude of this modes increases with increasing fluence but above 10 $mJcm^{-2}$ the modes disappear, suggesting a completion of the phase transition. This is exemplified in Figure 7.6d, showing the amplitude of the modes as a function of fluence. Strikingly, we do not observe the appearance of the 7.5 THz (corundum) mode at high fluence, despite of the disappearance of the monoclinic modes.

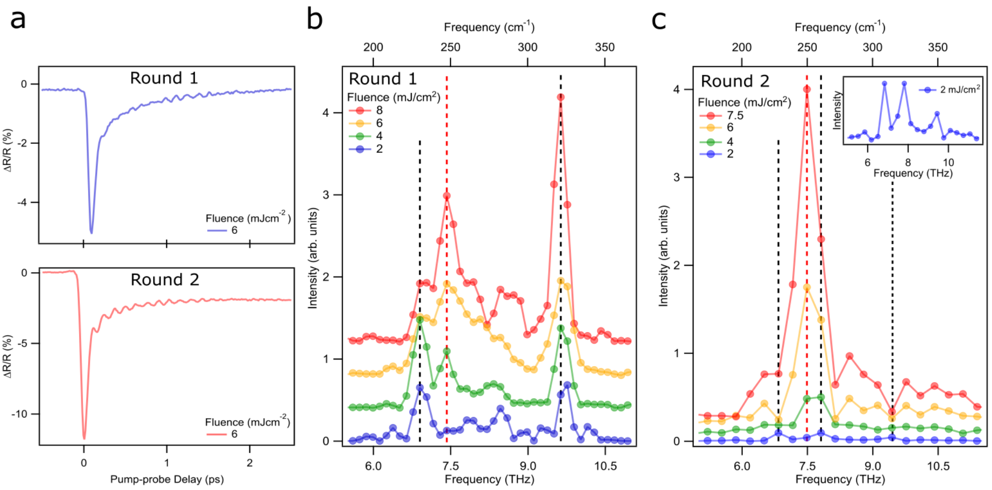

Figure 7.4: **Data comparison of two experimental rounds in a single crystal of** V_2O_3 a) Top: Round 1 of the transient reflectivity of V_2O_3 in the visible range measured at 77 K (below T_c~150 K) upon 800 nm excitation (F=6 mJcm^{-2}). A sharp reflectivity change occurs immediately after photoexcitation across t=0 ps. Most of the signal recovers within less than 200 fs; the remaining long-lived signal is modulated by coherent oscillations. Bottom: Round 2 of measurement under the same conditions. A difference in amplitude is observed. b) The Fourier transform of the oscillating component of Round 1 yields the three antiferromagnetic phonon modes at 6.9, 8.4, and 9.6 THz (black dashed lines) for low fluence value. Pumping at higher fluence, the metallic 7.5 THz phonon mode appears (red dashed lines). The traces are offset for clarity. c) FFT of the oscillations of Round 2. At low fluence appear three antiferromagnetic insulating modes with frequencies at 6.8, 7.8, and 9.4 THz (black dashed lines). At higher fluences, the metallic mode at 7.5 THz appears (red dashed lines), while the low temperature modes disappear. The inset shows a zoom of the 2 mJcm^{-2} data.

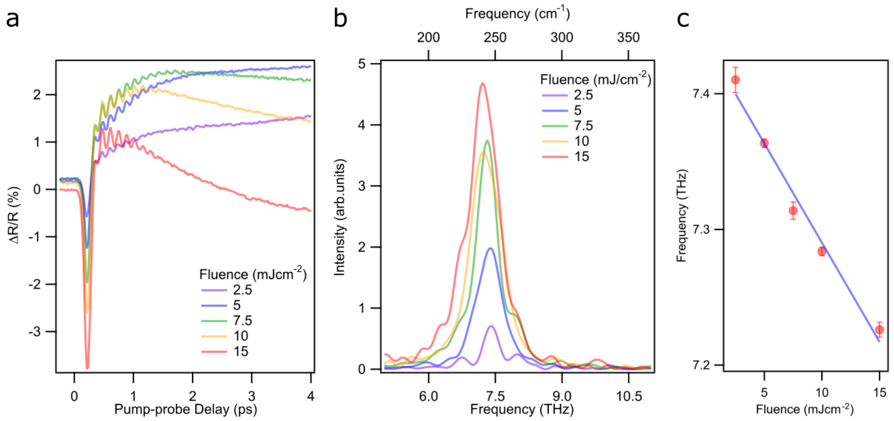

Figure 7.5: **Transient reflectivity data and FFT above** T$_c$ **in a thin film of** V$_2$O$_3$ a) Transient reflectivity data above T$_c$ upon 700 nm excitation at 154 K (PM-M) at different fluence values. b) Fourier transform of the oscillations in the transient reflectivity at 154 K. c) Linear red shift of the frequency metallic mode as the fluence is increased. The red dots indicate the frequency of the phonon. Blue line shows the linear fit of these frequency values.

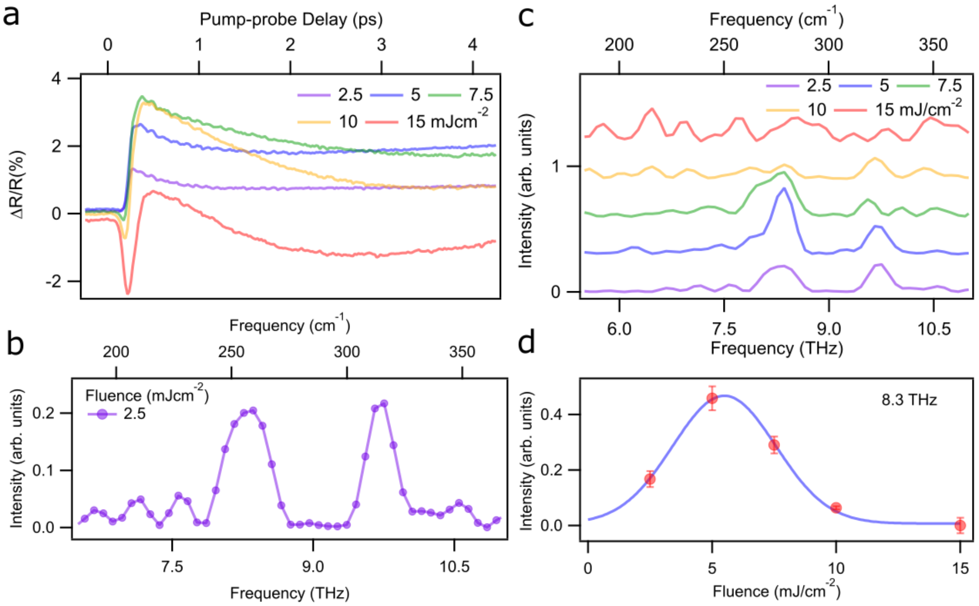

Figure 7.6: **Evolution with fluence of** A_g **phonon modes** a) Transient reflectivity data of V_2O_3 at 1800 nm measured at 25 K (AFI) upon 700 nm excitation at different fluence values. b) Fourier transform of the oscillations in the transient reflectivity at 2.5 $mJcm^{-2}$ after having differentiated the transient data to remove the background. Two coherent modes which correspond to the A_g mode are observed at 8.3 and at 9.85 THz. c) Comparison of the FFT traces at different fluence values. At low fluence values, two phonon modes are observed, whose amplitude increases with fluence until the A_g modes start to vanish after pumping at more energy. For clarity, the traces are offset. d) Intensity of the phonon modes as a function of fluence. The blue line is a guide to the eye that shows a fluence threshold between 5 and 7 $mJcm^{-2}$.

7.3 Discussion

Our measurements of thin films of V_2O_3 show that: (1) the metallic phase is characterized by a 7.5 THz mode, (2) the antiferromagnetic insulator state is characterized by 8.4 and 9.6 THz modes, (3) that such vibrations correspond to those measured using static Raman and that they can also be tracked by means of pump-probe spectroscopy at 1800 nm. In relation to the photo-induced phase transition our results show that (4) photo-excitation of the insulating phase above 10 mJcm^{-2} causes its characteristics vibration modes to disappear in the same way that occurs in VO_2 but, importantly, without the concomitant appearance of the monoclinic 7.5 THz mode. This result suggest that the metallic A_{1g} mode is not excited in the photo-induced phase transition. This can happen under several scenarios:

1. The lattice potential change is too slow. Although, this seems unlikely since the 9.6 THz mode (whose oscillation period is 105 fs) is sensitive to changes in lattice with increasing fluence. If the lattice potential change took longer than 105 fs we would expect to see an oscillation. However, we do not see any oscillation, so the potential change must be much faster than 105 fs and, presumably, faster than 52 fs (half a period). This timescale is fast enough to generate the metallic phase mode coherently.

2. The A_{1g} mode may be at zero amplitude in both phases, i.e., the atoms are already in the high symmetry positions before the phase transition. However, this cannot be the case due to excitation of the metallic phase leads to coherent generation of the A_{1g} mode, thus we would only expect this for one unique fluence. Higher fluences should still induce motion as higher fluences induce larger metallic phase motion.

3. An intermediate lattice potential is formed in which there is no Raman active mode. While this is a possibility, it seems unlikely because it would have a lower symmetry than both the insulating phase and the metallic phase, with no low frequency Raman active mode.

While we cannot completely exclude the third scenario, we instead examine if an instant change to the metallic phase potentially necessarily would generate coherence. Most theories to date have focused on how changing the potential changes the dynamics of the lattice, however, they have neglected what happens to the damping [103, 104, 105]. For strong damping, the dynamics of the phonons are less influenced by the potential and more influenced by the interactions with the other degree of freedom. Thus, the photo-excited potential could be the high temperature metallic phase, but the dephasing rate may be much higher than in equilibrium. Such strong coupling to other degrees of freedom is perhaps quite likely given the system is going through a phase transition. Firstly crystals show the largest deviation from harmonicity at phase transitions. Anharmonicity means the usual vibrational modes of the solid can be mixed together, enabling the transfer of energy to multiple lattice degrees of freedom. Furthermore, the transition from insulator to metal results in a large change in the charge distribution and the ability to screen fields. The rapid change during the transition could easily result in a strong damping on the excitation of any coherence.

Open questions then are *when the photo-excited phase resembles that of the equilibrium phase* and *when coherence can be excited*. To answer this question, double pulse excitation will be needed, where the first pulse can switch the potential and the second pulse can excite the new state. By varying the pump-pump delay the timescale for the non-equilibrium overdamped response could be mapped out, similar to what has been done for VO_2 [100].

In conclusion, we have seen that the vibrational coherence is not transferred across the phase transition in Mott-insulating V_2O_3. We found that while the vibrational coherence of the insulating phase is lost on a sub-phonon-period timescale, this coherence is not transferred to the metallic phase. This suggests that at the phase transition, multiple degrees of freedom are strongly coupled. As a result, there is a strong dephasing between modes of the system which prevents vibrational coherence being transferred despite the rapid restoration of the high symmetry state. While the restoration of the high symmetry phase can occur very rapidly, coherent phonons of the high symmetry phase cannot be excited until the initial non-equilibrium distributions has relaxed reducing the coupling between phonon modes and phonons with the excited electronic population.

Chapter 8

Summary and Outlook

Correlated materials have been an attracted area of research for the last decades due to their exotic properties given as a result of the electron-electron interactions. This stands in contrast to other commonly materials such as silicon or magnesium, whose properties are comparatively unaffected by the Coulomb repulsion. The remarkable properties and transitions between distinct, competing phases with dramatically different electronic and magnetic orders are fascinating from the science perspective as well as for emerging technological applications. Therefore, for exploiting quantum advantages in new photonic, electronic and energy technologies, it is vital a practical understanding of the correlated material properties. One way to lead new material properties is given by chemical doping, i.e, by introducing ions with a higher or lower valency where new phases can be stabilised. An alternative way to control these properties out of equilibrium is provided by photo-excitation, where light induces structural and electronic phase transitions in correlated materials. The advances on the development on the laser sources over the years have given rise to new techniques to characterize these materials. Nowadays, probing correlated materials by X-ray sources is one of the most used approached, nevertheless, the few facilities in the world gives as a result a limited number of experiments that can be performed. However, the use of ultrafast laser systems allows us to measure in a systematic manner by performing optical pump-probe spectroscopy providing us similar information to those obtained with X-ray lasers.

In this thesis, we have performed a broadband spectroscopy measurement at multiple experimental conditions such as time delays, excitation fluence and temperature on $Sr_3Ir_2O_7$ and V_2O_3 correlated materials which present electronic, structural and magnetic phase transitions. The main achievements and findings from the research of both compounds are summarized in the following.

$Sr_3Ir_2O_7$ has been measured in the paramagnetic and antiferromagnetic phases above and below $T_N \approx 280$ K, respectively. The spectrum is high sensitive to temperature and photo-excitation fluences, showing significant differences on each different phases. Such a strong dependence on the temperature and fluence makes it difficult for us to reliably separate the dataset into functions of specific variables, and no unique spectral function for the electronic degrees of freedom can be found. Looking to the transient reflectivity data in the visible range, we can observe that the signal is modulated by two A_{1g} phonon modes. These two modes are also sensitive to both, temperature and excitation fluence. These high sensitivities to the temperature and fluence suggest that the visible range could be highly sensitivity to the magnetic order and thus provide a platform to understand the physics of photo-excited of $Sr_3Ir_2O_7$. To that end, we have studied a detailed behaviour of the magnetic order with temperature, wavelength, time and fluence. It has been shown that moderate photo-excitation causes a large, $\sim 50\%$, and prompt suppression of magnetic order which can recover rapidly within a picosecond. In contrast, at higher excitation densities, the magnetic order can be completely suppressed, resulting in a dramatic increase of the recovery time. In addition, the lattice temperature remains below the equilibrium Néel temperature while the system is in the demagnetized state, showing that the long-lived state is non-thermal. These results suggest that the formation of photo-induced spin defects enable a pathway of the demagnetized state and the recovery of magnetic order.

V_2O_3 has been measured on its paramagnetic metallic phase at 200 K and on the antiferromagnetic insulator phase at 77 K. The measurements performed at high temperature by pump-probe spectroscopy shows a transient reflectivity signal modulated by coherent phonons. The agreement on the frequency value of the phonon mode measured by two different techniques, pump-probe and Raman spectroscopy, suggests that there is no evidence for a transient non-thermal phase in V_2O_3 that is established by a lattice distortion and photo-induced hardening of the A_{1g} phonon mode, as it has been previously claimed.

For the low temperature phase and the light induced phase transition in a thin film of V_2O_3, we detect two of the characteristic insulating A_g modes at low excitation fluence by performing a pump-probe spectroscopy measurement. The amplitude of these modes increases with increasing fluence but at high fluence the modes disappear, suggesting a completion of the phase transition. However, the appearance of the characteristic metallic mode is not observe. We suggest a scenario where most theories to date have not been focused on since most of them have neglected what happens to the damping. For strong damping, the dynamics of the coherent phonons are less influenced by the potential and more influenced by the interactions with other degree of freedom. Thus, the photo-excited potential could be in the high temperature metallic phase, but the dephasing rate may be much higher than in equilibrium.

The analysed compounds, $Sr_3Ir_2O_7$ and V_2O_3, have the similarity of being two antiferromagnetic materials at low temperature that undergo a phase transition as temperature increases, either an electronic and structural phase transition (V_2O_3) or only magnetic ($Sr_3Ir_2O_7$). In this thesis, it has been shown that these different phase transitions can be controlled by means of the broadband pump-probe spectroscopy technique. In addition, we have shown different techniques of careful analysis of these results in order to find a clear marker for a specific degree of freedom or a photo-excitation process. However, despite this detailed study of phase transitions in different correlated materials, there are still many further avenues for investigation:

- The pump probe signal was significantly stronger on single crystals over the thin films. It would be beneficial to have this quality in a repeatable way in order to attempt to extract spin dynamics from the optical data as performed on $Sr_3Ir_2O_7$. One way to do this would be to polish samples to a very thin thickness (in the order of microns) in order to try to prevent cracking.

- A double-pump probe experiment can be done in V_2O_3 to answer the questions of when the photo-excited phase resembles that of the equilibrium phase and when coherence can be excited.

- Tracking the spin and charge ordering in the monolayer iridate compound, Sr_2IrO_4, can be performed. This will help to identify more similarities or differences between the iridates compounds.

All these approaches could be implemented in a very near future. Furthermore, the techniques and concepts developed in this thesis can be used to study the transient optical response of other correlated materials in order control the properties on demand.

Abbreviations

AFI	**A**nti**f**erromagnetic **I**nsulator
AFM	**A**nti**f**erro**m**agnetic
ARPES	**A**ngle-**R**esolved **P**hoto**E**mission **S**pectroscopy
CMOS	**C**omplementary **M**etal-**O**xide-**S**emiconductor
DFT	**D**ensity **F**unctional **T**heory
$\mathbf{E_F}$	Fermi Level
$\mathbf{F^{th}}$	**F**lunce **Th**reshold
FFT	**F**ast **F**ourier **T**ransform
FWHM	**F**ull **W**idth at **H**alf **M**aximum
GDD	**G**roup **D**elay **D**ispersion
H	**H**orizontal
HF	**H**artree-**F**ock
IMT	**I**nsulator-**M**etal **T**ransition
IR	**I**nfra**r**ed
LDA	**L**ocal-**D**ensity **A**pproximation
LHB	**L**ower-**H**ubbard **B**and
$\mathbf{LN_2}$	**L**iquid **N**itrogen
$\mathbf{M_1}$	**M**onoclinic
ND	**N**eutral **D**ensity
OPA	**O**ptical **P**arametric **A**mplifier
PM	**P**ara**m**agnetic
PM-I	**P**ara**m**agnetic **I**nsulator
PM-M	**P**ara**m**agnetic **M**etal
R	**R**utile
REXS	**R**esonant **E**lastic **X**-ray **S**cattering
RIXS	**R**esonant **I**nelastic **X**-ray **S**cattering
RXS	**R**esonant **X**-ray **S**cattering
SOC	**S**pin-**O**rbit **C**oupling
$\mathbf{T_c}$	**C**ritical **T**emperature

T_N	**N**éel **T**emperature
TMO	**T**ransition **M**etal **O**xide
tr-REXS	**T**ime-**R**esolved **R**esonant **E**lastic **X**-ray **S**cattering
tr-RIXS	**T**ime-**R**esolved **R**esonant **I**nelastic **X**-ray **S**cattering
tr-XRD	**T**ime-**R**esolved **X**-**R**ay **D**iffraction
TRR	**T**ime **R**esolved **R**eflectivity
U	Coulomb potential energy
UHB	**U**pper-**H**ubbard **B**and
UV-VIS	**U**ltra**v**iolet-**Vis**ible
V	**V**ertical
XAS	**X**-ray **A**bsorption **S**pectroscopy
XFEL	**X**-ray **F**ree-**E**lectron **L**aser

Publications

The work presented in this thesis comprises the following publications:

1. David Moreno-Mencía, Alberto Ramos-Álvarez, Luciana Vidas, Seyed M. Koohpaye, Simon Wall. Ultrafast evolution and transient phases of a prototype out-of-equilibrium Mott-Hubbard material, *Nat. Commun.* **10**, 4034 (2019).
2. Ernest Pastor, David Moreno-Mencía, Maurizio Monti, Allan S. Johnson, Nina Fleischmann, Cuixiang Wang, Youguo Shi, Xuerong Liu, Daniel G. Mazzone, Mark P.M. Dean, Simon Wall. Non-thermal breaking of magnetic order via photo-generated spin defects, *arXiv:2104.04294* (2021).
3. Allan S. Johnson, David Moreno-Mencía, Ernest Pastor, Simon Wall. Phase transition dominated by dephasing in V_2O_3, *In preparation.*

Bibliography

[1] Tokura, T. Correlated-Electron Physics in Transition-Metal Oxides. *Physics Today* **56**, 50-55 (2003).

[2] Basov, D.N., Averitt, R.D. & Hsieh, D. Towards properties on demand in quantum materials. *Nature Mater* **16**, 1077-1088 (2017).

[3] Zhang, J. & Averitt, R.D. Dynamics and Control in Complex Transition Metal Oxides. *Annual Review of Materials Research* **44**, 19-43 (2014).

[4] Morosan, E., Natelson, D., Nevidomskyy, A.H. & Si, Q. Strongly Correlated Materials. *Adv. Mater.* **24**, 4896-4923 (2012).

[5] Bednorz, J.G. & Müller, K.A. Possible High Tc Superconductivity in the Ba-La-Cu-0 System. *Z. Phys. B* **64**, 5003–5008 (1986).

[6] Wu, M.K., Ashburn, J.R., Torng, C.J., Hor, P.H., Meng, R.L., Gao, L., Huang, Z.J., Wang, Y.Q. & Chu, C.W. Superconductivity at 93 K in a new mixed-phase Y-Ba-Cu-O compound system at ambient pressure. *Phys.Rev.Lett.* **58**, 908–910 (1987).

[7] Millis, A. Lattice effects in magnetoresistive manganese perovskites. *Nature* **392**, 147-150 (1998).

[8] Tokura, Y. *Colossal Magnetoresistive Oxides* (Ed.Gordon and Breach Science, 2000).

[9] Dagotto, E., Hotta, T. & Moreo, A. Colossal magnetoresistant materials: the key role of phase separation. *Physics Reports* **344**, 1–153 (2001).

[10] Campi, G., Bianconi, A., Poccia, N., Bianconi, G., Barba, L., Arrighetti, G., Innocenti, D., Karpinski, J., Zhigadlo, N.D., Kazakov, S.M., Burghammer, M., Zimmerman, M.v., Sprung, M., & Ricci, A. Inhomogeneity of charge-density-wave order and quenched disorder in a high-Tc superconductor. *Nature* **525**, 359–362 (2015).

[11] Le Tacon, M., Bosak, A., Souliou, S.M., Dellea, G., Loew, T., Heid, R., Bohnen, K-P., Ghiringhelli, G., Krisch, M. & Keimer, B. Inelastic x-ray scattering in $YBa_2Cu_3O_{6.6}$ reveals giant phonon anomalies and elastic central peak due to charge-density-wave formation. *Nature Phys.* **10**, 52–58 (2014).

[12] Basov, D.N., Averitt, R.D., van der Marel, D., Dressel, M. & Haule, K. Electrodynamics of correlated electron materials. *Rev. Mod. Phys.* **83**, 471-541 (2011).

[13] Taillefer, L. Scattering and Pairing in Cuprate Superconductors. *Annual Review of Condensed Matter Physics* **1**, 51-70 (2010).

[14] Yamani, Z., Tun, Z. & Ryan, D.H. Neutron scattering study of the classical antiferromagnet MnF2: a perfect hands-on neutron scattering teaching course. *Canadian Journal of Physics* **88**, 771-797 (2010).

[15] Maekawa, S., Tohyama, T., Barnes, S.E., Ishihara, S., Koshibae, W. & Khaliullin, G. *Physics of Transition Metal Oxides* (Ed.Springer, 2004).

[16] Mohn, P. *Magnetism in the Solid State: An Introduction.* (Ed.Springer, 2003).

[17] Mott, N.F. Metal-insulator transition. *Rev. Mod. Phys.* **40**, 677-683 (1968).

[18] Peierls, R. *More surprises in Theoretical Physics* (Princeton University Press, 1991).

[19] Vidas, L. The insulator-metal phase transition in VO_2 measured at nanometer length scales and femtosecond time scales. Ph.D. thesis, ICFO (2019).

[20] Imada, M., Fujimori, A. & Tokura, Y. Metal-insulator transitions. *Rev. Mod. Phys.* **70**, 1039-1263 (1998).

[21] Cheong, S.-W., Sharma, P., Hur, N., Horibe, Y. & Chen, C. Electronic phase separation in complex materials. *Physica B: Condensed Matter* **318**, 39–51 (2002).

[22] Ricci, A., Poccia, N., Campi, G., Joseph, B., Arrighetti, G., Barba, L., Reynolds, M., Burghammer, M., Takeya, H., Mizuguchi, Y., Takano, Y.,

Colapietro M., Saini, N.L. & Bianconi, A. Nanoscale phase separation in the iron chalcogenide superconductor $K_{0.8}Fe_{1.6}Se_2$ as seen via scanning nanofocused X-ray diffraction. *Phys. Rev. B* **84**, 060511 (2011).

[23] Park, J.T., Inosov, D.S., Niedermayer, Ch., Sun, G.L., Haug, D., Christensen, N.B., Dinnebier, R., Boris, A.V., Drew, A.J., Schulz, L., Shapoval, T., Wolff, U., Neu, V., Yang, X., Lin, C.T., Keimer, B. & Hinkov, V. Electronic phase separation in the slightly underdoped iron pnictide superconductor $Ba_{1-x}\mathbf{K}_xFe_2As_2$. *Phys. Rev. Lett.* **102**, 117006 (2009).

[24] Shank, C., Yen, R., Fork, R.L., Orenstein, J. & Baker, G.L. Picosecond Dynamics of Photoexcited Gap States in Polyacetylene. *Phys. Rev. Lett.* **49**, 1660-1663 (1982).

[25] Shank, C., Yen, R. & Hirlimann, C. Time-Resolved Reflectivity Measurements of Femtosecond-Optical-Pulse-Induced Phase Transitions in Silicon. *Phys. Rev. Lett.* **50**, 454-457 (1983).

[26] Yu, G., Lee ,C.H., Heeger, A.J., Herron, N. & McCarron, E.M. Transient photoinduced conductivity in single crystals of $YBa_2Cu_3O_{6.3}$: “Photodoping” to the metallic state. *Phys. Rev. Lett.* **67**, 2581–2584 (1991).

[27] Cavalleri, A., Tóth, Cs., Siders, C. W., Squier, J. A., Ráksi, F., Forget, P. & Kieffer, J. C. Femtosecond structural dynamics in VO_2 during an ultrafast solid-solid phase transition. *Phys. Rev. Lett.* **87**, 237401 (2001).

[28] Chapman, H.N., Barty, A., Bogan, M.J., Boutet, S., Frank, M., Hau-Riege, S.P., Marchesini, S., Woods, B.W., Bajt, S., Benner, W.H., London, R., Plönjes, E., Kuhlmann, M., Treusch, R., Düsterer, S., Tschentscher, T., Schneider, J.R., Spiller, E., Möller, T., Bostedt, C., Hoener, M., Shapiro, D.A., Hodgson, K.O., van der Spoel, D., Burmeister, F., Bergh, M., Caleman, C., Huldt, G., Seibert, M.M., Maia, F.R.N.C., Lee, R.W., Szöke, A., Timneanu, N. & Hajdu, J., Femtosecond diffractive imaging with a soft-X-ray free-electron laser. *Nature Phys.* **2**, 839-843 (2006).

[29] Marchesini, S., Boutet, S., Sakdinawat, A.E., Bogan, M.J., Bajt, S., Barty, A., Chapman, H.N., Frank, M., Hau-Riege, S.P., Szöke, A., Cui, C., Shapiro, D.A., Howells, M.R., Spence, J.C., Shaevitz, J.W., Lee, J.Y., Hajdu, J. & Seibert, M.M. Massively parallel X-ray holography. *Nat. Photonics* **2**, 560-563 (2008).

[30] Barty, A., Boutet, S., Bogan, M.J., Hau-Riege, S.P., Marchesini, S., Sokolowski-Tinten, K., Stojanovic, N., Tobey, R., Ehrke, H., Cavalleri, A., Düsterer, S., Frank, M., Bajt, S., Woods, B.W., Seibert, M.M., Hajdu, J., Treusch, R. & Chapman, H.N. Ultrafast single-shot diffraction imaging of nanoscale dynamics. *Nat. Photonics* **2**, 415-419 (2008).

[31] Wall, S., Yang, S., Vidas, L., Chollet, M., Glownia, J.M., Kozina, M., Katayama, T., Henighan, T., Jiang, M., Miller, T.A., Reis, D.A., Boatner, L.A., Delaire, O. & Mariano, T. Ultrafast disordering of vanadium dimers in photoexcited VO_2. *Science* **362**, 572–576 (2018).

[32] Vargis, E., Tang, Y.W., Khabele, D. & Mahadevan-Jansen, A. Near-infrared Raman Microspectroscopy Detects High-risk Human Papillomaviruses. *Transl. Oncol.* **5**, 172-9 (2012).

[33] Kim, J., Casa, D., Upton, M.H., Gog, T., Kim, Y-J., Mitchell, J.F., Van Veenendaal, M., Daghofer, M., Van Den Brink, J., Khaliullin, G. & Kim, B.J. Magnetic Excitation Spectra of Sr_2IrO_4 Probed by Resonant Inelastic X-Ray Scattering : Establishing Links to Cuprate Superconductors. *Phys.Rev.Lett.* **108**, 177003 (2012).

[34] Ramos-Alvarez, A., Fleischmann, N., Vidas, L., Fernandez-Rodriguez, A. & Wall, S. Probing the lattice anharmonicity of superconducting $YBa_2Cu_3O_{7-\delta}$ via phonon harmonics. *Phys. Rev. B* **100**, 184302 (2019).

[35] Hogan, T.C. Probing the spin-orbit Mott state in $Sr_3Ir_2O_7$ by electron doping. Ph.D. thesis, Boston College (2016).

[36] Beznosikov, B.V. & Aleksandrov, K.S. Perovskite-like crystals of the Ruddlesden-Popper series. *Crystallogr. Rep.* **45**, 792-798 (2000).

[37] Lee, D. & Lee, H.N. Controlling Oxygen Mobility in Ruddlesden–Popper Oxides. *Materials* **10**, 368 (2017).

[38] Ge, M., Qi, T.F., Korneta, O.B., De Long, D.E., Schlottmann, P., Crummett, W.P. & Cao, G. Lattice-driven magnetoresistivity and metal-insulator transition in single-layered iridates. *Phys. Rev. B* **84**, 100402 (2011).

[39] Zhao, J.G., Yang, L.X., Yu, Y., Li, F.Y., Yu, R.C., Fang, Z., Chen, L.C. & Jin, C.Q. High-pressure synthesis of orthorhombic perovskite and its positive magnetoresistance. *Journal of Applied Physics* **103**, 103706 (2008).

[40] Liu, P., Kim, B., Chen, X-Q., Sarma, D.D., Kresse, G. & Franchini, C. Relativistic GW+BSE study of the optical properties of Ruddlesden-Popper iridates. *Phys. Rev. Materials* **2**, 075003 (2018).

[41] Chu, H., Zhao, L., Torre, A., Hogan, T., Wilson, S.D. & Hsieh, D. A charge density wave-like instability in a doped spin–orbit-assisted weak Mott insulator. *Nature Mater.* **16**, 200–203 (2017).

[42] Huang, Q., Soubeyroux, J.L., Chmaissem, O., Natali Sora, I., Santoro, A., Cava, R.J., Krajewski, J.J. & Peck, W.F. Neutron powder diffraction study of the crystal structures of Sr_2RuO_4 and Sr_2IrO_4 at room temperature and at 10 K. *Journal of Solid State Chemistry* **112**, 355–361 (1994).

[43] Subramanian, M., Crawford, M. & Harlow, R. Single crystal structure determination of double layered strontium iridium oxide $Sr_3Ir_2O_7$. *Materials Research Bulletin* **29**, 645–650 (1994).

[44] Villars, P., Cenzual, K., Daams, J., Gladyshevskii, R., Shcherban, O., Dubenskyy, V., Kuprysyuk, V., Savysyuk, I. & Zaremba, R. Structure Types. Part 10: Space Groups (140) I4/mcm-(136)P4_2/mnm-$Sr_3Ir_2O_7$. Springer Materials (2011).

[45] Hu, L.L., Yang, M., Wu, Y.L., Wu, Q., Zhao, H., Sun, F., Wang, W., He, R., He, S.L., Zhang, H., Huang, R.J., Li, L.F., Shi, Y.G. & Zhao, J. Strong pseudospin-lattice coupling in $Sr_3Ir_2O_7$: Coherent phonon anomaly and negative thermal expansion. *Phys. Rev. B* **99**, 094307 (2019).

[46] Grettarsson, H., Sung, N.H., Hoppner, M., Kim, B.J., Keimer, B. & Le Tacon, M. Two-Magnon Raman Scattering and Pseudospin-Lattice Interactions in Sr_2IrO_4 and $Sr_3Ir_2O_7$. *Phys. Rev. Lett.* **116**, 136401 (2016).

[47] Kim, B.J., Hosub, H., Moon, S.J., Kim, J., Park, B., Leem, C.S., Yu, J., Noh, T.W., Kim, C., Oh, S., Park, J., Durairaj, V., Vao, G. & Rotenberg, E. Novel Jeff=1/2 Mott State Induced by Relativistic Spin-Orbit Coupling in $Sr_3Ir_2O_7$. *Phys. Rev. Lett.* **101**, 076402 (2008).

[48] Wang, Q., Cao, Y., Waugh, J.A., Park, S. R., Qi, T. F., Korneta, O. B., Cao, G. & Dessau, D. S. Dimensionality-controlled Mott transition and correlation effects in single-layer and bilayer perovskite iridates. *Phys. Rev. B* **87**, 245109 (2013).

[49] Schnells, V.I. Theory of the magnetic properties of the bilayer iridate $Sr_3Ir_2O_7$. MSc thesis, Philipss-Universität Marburg (2013).

[50] Okada, Y., Walkup, D., Lin, H., Dhital, C., Chang, T.-R., Khadka, S., Zhou, W., Jeng, H.-T., Paranjape, M., Bansil, A., Wang, Z., Wilson, S.D. & Madhavan, V. Imaging the evolution of metallic states in a correlated iridate. *Nature Mater.* **12**, 707-713 (2013).

[51] Kim, B.J., Ohsumi, H., Komesu, T., Sakai, S., Morita, T., Takagi, H. & Arima, T. Phase-sensitive observation of a spin-orbital Mott state in Sr_2IrO_4. *Science* **323**, 1329–1332 (2009).

[52] Moon, S.J., Jin, H., Kim, K.W., Choi, W.S., Lee, Y.S., Yu, J., Cao, G., Sumi, A., Funakubo, H., Bernhard, C. & Noh, T.W. Dimensionality-Controlled Insulator-Metal Transition and Correlated Metallic State in 5d Transition Metal Oxides $Sr_{n+1}IrO_{3n+1}$ (n =1, 2, and inf). *Phys. Rev. Lett.* **101**, 226402 (2008).

[53] Shitade, A., Katsura, H., Kuneš, J., Qi, X.-L., Zhang, S.-C. & Nagaosa, N. Quantum Spin Hall Effect in a Transition Metal Oxide Na_2IrO_3. *Phys. Rev. Lett.* **102**, 256403 (2009).

[54] Jackeli, G. & Khaliullin, G. Mott Insulators in the Strong Spin-Orbit Coupling Limit: From Heisenberg to a Quantum Compass and Kitaev Models. *Phys.Rev.Lett.* **102**, 017205 (2009).

[55] Fink, J., Schierle, E., Weschke, E. & Geck, J. Resonant elastic soft X-ray scattering. *Rep. Prog. Phys.*, **76**, 056502 (2013).

[56] Ament, L.J.P., Veenendaal, M.V., Devereaux, T.P. & Hill, J.P. Resonant inelastic X-ray scattering studies of elementary excitations. *Rev. Mod. Phys.* **83**, 705–767 (2011).

[57] Kim, J., Said, A.H., Casa, D., Upton. M.H., Gog, T., Daghofer, M., Jackeli, G., Van Den Brink, J., Khaliullin, G. & Kim, B.J. Large Spin-Wave

Energy Gap in the Bilayer Iridate $Sr_3Ir_2O_7$: Evidence for Enhanced Dipolar Interactions Near the Mott Metal-Insulator Transition. *Phys. Rev. Lett.* **109**, 157402 (2012).

[58] Dhital, C., Hogan, T., Zhou, W., Chen, X., Ren, Z., Pokharel, M., Okada, Y., Heine, M., Tian, W., Yamani, Z., Opeil, C., Helton, J.S., Lynn, J.W., Wang, Z., Madhavan, V. & Wilson, S.D. Carrier localization and electronic phase separation in a doped spin-orbit-driven Mott phase in $Sr_3(Ir_{1-x}Ru_x)_2O_7$. *Nat. Commun.* **5**, 3377 (2014).

[59] Dean, M.P.M., Cao, Y., Liu, X., Wall, S., Zhu, D., Mankowsky, R., Thampy, V., Chen, X.M, Vale, J.G., Casa, D., Kim, J., Said, A.H., Juhas, P., Glownia, J.M., Robert, A., Robinson, J., Sikorski, M., Song, M., Kozina, M., Lemke, H., Patthey, L., Owada, S., Katayama, T., Yabashi, M., Tanaka, Y., Togashi, T., Liu, J., Serrao, C.R, Kim, B.J. & Huber, L. Ultrafast energy- and momentum-resolved dynamics of magnetic correlations in the photo-doped Mott insulator Sr_2IrO_4. *Nature Mater.* **15**, 601–605 (2016).

[60] Mazzone, D.G., Meyers, D., Cao, Y., Vale, J.G., Dashwood, C.D., Shi, Y., James, A.J.A., Robinson, N.J., Lin, J., Thampy, V., Tanaka, Y., Johnson, A.S., Miao, H., Wang, R., Assefa, T.A., Kim, J., Casa, D., Mankowsky, R., Zhu, D., Alonso-Mori, R., Song, S., Yavas, H., Katayama, T., Yabashi, M., Kubota, Y., Owada, S., Liu, J., Yang, J., Konik, R.M., Robinson, I.K., Hill, J.P., McMorrow, D.F., Först, M., Wall, S., Liu, X. & Dean, M.P.M. Laser-induced transient magnons in Sr3Ir2O7 throughout the Brillouin zone. *Proceedings of the National Academy of Sciences* **118** (2016).

[61] Park, H.J., Sohn, C.H., Jeong, D.W., Cao, G., Kim, K.W., Moon, S.J., Jin, H., Cho, D.-Y. & Noh, T.W. Phonon-assisted optical excitation in the narrow bandgap Mott insulator $Sr_3Ir_2O_7$. *Phys. Rev. B* **89**, 155115 (2014).

[62] Li, L., Kong, P.P., Qi, T.F., Jin, C.Q., Yuan, S.J., DeLong, L.E., Schlottmann, P. & Cao, G. Tuning the $J_{\mathrm{eff}} = \frac{1}{2}$ insulating state via electron doping and pressure in the double-layered iridate $Sr_3Ir_2O_7$. *Phys. Rev. B* **87**, 235127 (2013).

[63] Koshihara, S., Tokura, Y., Mitani, T., Saito, G. & Koda, T. Photoinduced valence instability in the organic molecular compound tetrathiafulvalene-p-chloranil (TTF-CA). *Phys. Rev. B* **42**, 6853–6856 (1990).

[64] Koopmans, B., Malinowski, G., Dalla Longa, F., Steiauf, D., Fähnle, M., Roth, T., Cinchetti, M. & Aeschlimann, M. Explaining the paradoxical diversity of ultrafast laser-induced demagnetization. *Nature Mater.* **9**, 259–265 (2010).

[65] Bittner, N., Golež, D., Strand, H.U.R., Eckstein, M. & Werner, P. Coupled charge and spin dynamics in a photoexcited doped Mott insulator. *Phys. Rev. B* **97**, 235125 (2018).

[66] Li, J., Dasari, N. & Eckstein, M. Ultrafast dynamics in relativistic Mott insulators. `arXiv:2010.09253` (2020).

[67] Pastor, E., Walsh, A., Park, J.-S., Steier, L., Bakulin, A.A., Kim, S., Grätzel, M. & Durrant, J.R. In situ observation of picosecond polaron self-localisation in $\alpha - Fe_2O_3$ photoelectrochemical cells. *Nat. Commun.* **10**, 3962 (2019).

[68] Guzelturk, B., Winkler, T., Van De Goor, T.W.J., Smith, M.D., Bourelle, S.A., Feldmann, S., Trigo, M., Teitelbaum, S.W., Steinrück, H.-G., De Pena, G., Alonso-Mori, R., Zhu, D., Sato, T., Karunadasa, H., Toney, M.F., Deschler, F. & Lindenberg, A.M. Visualization of dynamic polaronic strain fields in hybrid lead halide perovskites. *Nature Materials* **20**, 618–623 (2021).

[69] Lo Vecchio, I., Baldassarre, L., D'Apuzzo, F., Limaj, O., Nicoletti, D., Perucchi, A., Fan, L., Metcalf, P., Marsi, M. & Lupi, S. Optical properties of V_2O_3 in its whole phase diagram. *Phys. Rev. B* **91**, 155133 (2015).

[70] Morin, F.J. Oxides which show a metal-to-insulator transition at the Neel temperature. *Phys.Rev.Lett.* **3**, 34–36 (1959).

[71] Lechermann, F., Bernstein, N., Mazin, I. I. & Valentí, R. Uncovering the Mechanism of the Impurity-Selective Mott Transition in Paramagnetic V_2O_3. *Phys. Rev. Lett.* **121**, 106401 (2018).

[72] Autier-Laurent, S., Mercey, B., Chippaux, D., Limelette, P. & Simon, C. Strain-induced pressure effect in pulsed laser deposited thin films of the strongly correlated oxide V_2O_3. *Phys. Rev. B* **74**, 195109 (2006).

[73] Hansmann,P., Toschi, A., Sangiovanni, G., Saha-Dasgupta, T., Lupi, S., Marsi, M. & Held, K. Mott-Hubbard transition in V_2O_3. *Phys. Status Solidi B* **250**, 1251–1264 (2013).

[74] McWhan, D.B., Rice, T.M. & Remeika, J.P. Mott Transition in Cr-Doped V_2O_3. *Phys.Rev.Lett.* **23**, 1384–1387 (1969).

[75] McWhan, D.B., Menth, A., Remeika, J.P., Brinkman, W.F. & Rice, T.M. Metal-Insulator Transitions in Pure and Doped V_2O_3. *Phys. Rev. B* **7**, 1920–1931 (1973).

[76] Marezio, M., McWhan, D.B., Remeika, J.P. & Dernier, P.D. Structural aspects of the metal-insulator transitions in Cr-doped VO_2. *Phys. Rev. B* **5**, 2541–2551 (1972).

[77] Dernier, P.D. The crystal structure of V_2O_3 and $(V_{0.962}Cr_{0.038})_2O_3$. *J. Phys. Chem. Solids* **31**, 2569–2575 (1970).

[78] Saha-Dasgupta, T., Andersen, O.K, Nuss, J., Poteryaevv A.I., Georges A., Lichtenstein A.I. Electronic structure of V2O3: Wannier orbitals from LDA-NMTO calculations. *arXiv/0907.2841* (2009).

[79] McWhan, D.B. & Remeika, J.P. Metal-Insulator Transition in $(V_{1-x}Cr_x)_2O_3$. *Phys. Rev. B* **2**, 3734–3750 (1970).

[80] Ding, Y. Chen, C-C.,Zeng, Q., Kim, H-S.,Han, M.J., Balasubramanian, M., Gordon, R., Li, F., Bai, L., Popov, D., Heald, S.M,, Gog, T., Mao, H-K. & van Veenendaal, M. Novel High-Pressure Monoclinic Metallic Phase of V_2O_3. *Phys. Rev. Lett.* **112**, 056401 (2014).

[81] Dernier, P.D. & Marezio, M. Crystal Structure of the Low-Temperature Antiferromagnetic Phase of V_2O_3. *Phys. Rev. B* **2**, 3771–3776 (1970).

[82] Kuroda, N. & Fan, H.Y. Raman scattering and phase transitions of V_2O_3. *Phys. Rev. B* **16**, 5003–5008 (1977).

[83] Tatsuyama, C. & Fan, H. Y. Raman scattering and phase transitions in V_2O_3 and $(V_{1-x}Cr_x)_2O_3$. *Phys. Rev. B* **21**, 2977–2983 (1980).

[84] Castellani, C., Natoli, C.R. & Ranninger, J. Insulating phase of V_2O_3: An attempt at a realistic calculation. *Phys. Rev. B* **18**, 4967–5000 (1978).

[85] Castellani, C., Natoli, C.R. & Ranninger, J. Magnetic structure of V_2O_3 in the insulating phase. *Phys. Rev. B* **18**, 4945–4966 (1978).

[86] Castellani, C., Natoli, C.R. & Ranninger, J. Metal-insulator transition in pure and Cr-Doped V_2O_3. *Phys. Rev. B* **18**, 5001–5013 (1978).

[87] Poteryaev, A.I., Tomczak, J.M., Biermann, S., Georges, A., Lichtenstein, A.I., Rubtsov, A.N., Saha-Dasgupta, T. & Andersen, O.K. Enhanced crystal-field splitting and orbital-selective coherence induced by strong correlations in V_2O_3. *Phys. Rev. B* **76**, 085127 (2007).

[88] Lantz, G., Mansart, B., Grieger, D., Boschetto, D., Nilforoushan, N., Papalazarou, E., Moisan, N., Perfetti, L., Jacques, V.L.R., Le Bolloc'h, D., Laulhé, C., Ravy, S., Rueff, J.-P., Glover, T.E., Hertlein, M.P., Hussain, Z., Song, S., Chollet, M., Fabrizio, M. & Marsi, M. Ultrafast evolution and transient phases of a prototype out-of-equilibrium Mott–Hubbard material. *Nature Communications* **8**, 13917 (2017).

[89] Baroni, S., de Gironcoli, S., Dal Corso, A. & Giannozzi, P. Phonons and related crystal properties from density-functional perturbation theory. *Rev. Mod. Phys.* **73**, 515–562 (2001).

[90] Misochko, O.V., Tani, M., Sakai, K.,Kisoda, K., Nakashima, S., Andreev, V.N. & Chudnovsky, F. A., Optical study of the Mott transition in V_2O_3 : Comparison of time- and frequency-domain results. *Phys.Rev.B* **58**, 12789–12794 (1998).

[91] Ichikawa, H., Nozawa, S, Sato, T., Tomita, A., Ichiyanagi, K., Chollet, M., Guerin, L., Dean, N., Cavalleri, A., Adachi, S., Arima, T.-H., Sawa, H., Ogimoto, Y., Nakamura, M., Tamaki, R., Miyano, K. & Koshihara, S.-Y. Transient photoinduced 'hidden' phase in a manganite. *Nat. Matter.* **10**, 101-105 (2011).

[92] Fausti, D., Tobey, R. I., Dean, N., Kaiser, S., Dienst, A., Hoffmann, M. C., Pyon, S., Takayama, T., Takagi, H. & Cavalleri, A. Light-Induced Superconductivity in a Stripe-Ordered Cuprate. *Science* **331**, 189-191 (2011).

[93] Radu, I, Vahaplar, K., Stamm, C., Kachel, T., Pontius, N., Dürr, H. A., Ostler, T. A., Barker, J., Evans, R. F. L., Chantrell, R. W., Tsukamoto, A., Itoh, A, Kirilyuk, A., Rasing, Th. & Kimel, A. V. Transient ferromagnetic-like state mediating ultrafast reversal of antiferromagnetically coupled spins. *Nature* **472**, 205-208 (2011).

[94] Siders, C. W., Cavalleri, A., Sokolowski-Tinten, K., Tóth, Cs., Guo, T., Kammler, M., von Hoegen, M. H., Wilson, K. R., von der Linde, D. & Barty, C. P. J. Detection of Nonthermal Melting by Ultrafast X-ray Diffraction. *Science* **286**, 1340-1342 (1999).

[95] Baum, P., Yang, D.-S. & Zewail, A.H. 4D Visualization of Transitional Structures in Phase Transformations by Electron Diffraction. *Science* **318**, 788-792 (2007).

[96] Fausti D., Misochko, O.V. & van Loosdrecht, P.H.M. Ultrafast photoinduced structure phase transition in antimony single crystals. *Phys. Rev. B* **80**, 161207 (2009).

[97] Stevens T.E., Kuhl, J. & Merlin, R. Coherent phonon generation and the two stimulated Raman tensors. *Phys. Rev. B* **65**, 144304 (2002).

[98] Zeiger, H.J., Cheng, T.K., Ippen, E.P., Vidal, J., Dresselhaus, G. & Dresselhaus, M.S. Femtosecond studies of the phase transition in Ti_2O_3. *Phys. Rev. B* **54**, 105–123 (1996).

[99] Wall, S., Wegkamp, D., Foglia L., Appavoo, K., Nag, J., Haglund Jr. R.F., Stähler & Wolf, M. Ultrafast changes in lattice symmetry probed by coherent phonons. *Nat Commun.* **3** (2012).

[100] Wall, S., Foglia, L., Wegkamp, D., Appavoo, K., Nag, J., Haglund Jr. R.F., Stähler & Wolf, M. Tracking the evolution of electronic and structural properties of VO_2 during the ultrafast photoinduced insulator-metal transition. *Phys. Rev. B* **87**, 115126 (2013).

[101] Eyert, V. The metal-insulator transitions of VO_2: A band theoretical approach. *Annalen der Physik* **11**, 650–704 (2002).

[102] Vidas, L., Schick, D., Martínez, E., Perez-Salinas, D., Ramos-Álvarez, A., Cichy, S., Batlle-Porro, S., Johnson, A., Hallman, K.A., Haglund, R.F. & Wall, S. Does VO_2 Host a Transient Monoclinic Metallic Phase? *Phys. Rev. X* **10**, 031047 (2020).

[103] Beaud, P., Caviezel, A., Mariager, S.O., Rettig, L., Ingold, G., Dornes, C., Huang, S.-W., Johnson, J.A., Radovic, M., Huber, T., Kubacka, T., Ferrer, A., Lemke H.T., Chollet, M., Zhu, D., Glownia, J.M., Sikorski, M., Robert, A., Wadati, H., Nakamura, M., Kawasaki, M., Tokura, Y., Johnson, S.L. & Staub, U. A time-dependent order parameter for ultrafast photoinduced phase transitions. *Nature Materials* **13**, 923–927 (2014).

[104] Zong, A., Dolgirev, P.E., Kogar, A., Ergeçen, E., Yilmaz, M.B.,Bie, Y.-Q, Rohwer, T., Tung, I.-C., Straquadine, J., Wang, X., Yang, Y., Shen, X., Li, R., Yang J., Park, S., Hoffmann, M.C., Ofori-Okai, B.K., Kozina, M.E., Wen, H.,Wang, X.,Fisher, I.R.,Jarillo-Herrero, P. & Gedik, N. Dynamical slowing-down in an ultrafast photoinduced phase transition. *Phys. Rev. Lett.* **123**, 097601 (2019).

[105] Trigo, M., Giraldo-Gallo, P., Kozina, M.E., Henighan, T., Jiang, M.P., Liu, H.,Clark, J.N.,Chollet, M., Glownia, J.M., Zhu, D., Katayama, T., Leuenberger, D., Kirchmann, P.S., Fisher, I.R., Shen, Z.X. & Reis, D.A. Coherent order parameter dynamics in $SmTe_3$. *Phys. Rev. B* **99**, 104111 (2019).

Acknowledgements

A *castell* is a human tower built traditionally at festivals in Catalonia. These castells are built thanks to the collaboration and effort of many people. In the same way, the work and the achievements acquired in this thesis would not have been possible without the support and help of people who are very special to me.

This thesis is only the raised hand of the *enxaneta* (person at the top of the tower) that indicates that the construction of the castell is complete. However, to be at the top of the castell I have needed the help of an *aixecador*, which provides a stable platform for the *enxaneta*. This role is played by Simon whom I would like to thank the trust placed in me by giving me the opportunity of joining his group first, as a Master-student and later, as a PhD-student. I really appreciate his infinite patience with me because of repeating the same explanations or procedures thousands of times. Thanks to this, I have learnt a lot and I feel very happy and lucky to have had him as a group leader.

Two important people in the structure of the top part of the castell is given by *els dosos*. This position would be held by the *castellers* Ernest and Dani. The thesis would not have been written without the invaluable help of Ernest. I would like to thank him all the time spent with me trying to organize and to improve the text and plots of the thesis and papers. I will miss the fruit from his orchard and his jokes in any context. Thanks to Dani, my integration to the group was much easier and my experience in ICFO and Barcelona would not have been the same without him.

The *tronc* (trunk) of the tower would be all the others UDQS members. Special thanks to Allan (the V_2O_3 data would not have been possible without him as well as he has always been there to help me both in the lab and to answer my questions) and to Nina and Emmanuel (to share the office with friends is always a real pleasure). I would also thank to those who have already left the group like Elías, Luci, Alberto, Tim, Sergi... Thanks to all of them the environment in the lab and the office has been very nice and pleasant.

Por último, la *pinya* del castell está formada por mis amigos y mi familia.

Todos ellos forman parte de un colchón en el que sabía que si me caía, iban a estar ahí para amortiguar y hacer mucho más llevadero el golpe. De todos los amigos quiero destacar al grupo del Máster, a los de Córdoba y a mis amigos de siempre de Puertollano. Todos ellos me han estado apoyando y dando su cariño en cada momento. Me gustaría agradecer también a todos aquellos amigos que están en ICFO que han hecho que este lugar no lo haya visto únicamente como un lugar de trabajo. Y, para terminar, mis agradecimientos más grandes y verdaderos van dirigidos para mi familia y para Elena. A pesar de que mi familia esté físicamente lejos, los he sentido más cerca que nunca, especialmente en los momentos más duros. Había momentos en los que realmente necesitaba esa llamada de las 20:30 y ahí estaban apoyándome y sufriendo como nadie, a veces dudaba de si era yo quién tenía que entregar la tesis o eran ellos. Por otra parte, la importancia que tiene Elena, no solo en el doctorado, sino en los últimos 10 años es incalculable. La estabilidad anímica y mental que me ofrece a diario hacen que sea ella una de las personas más indispensables en la realización de toda esta tesis.